Phase Controlled Synthesis of Iron Sulfide Nanocrystals

By

Jordan Marcus Rhodes

Dissertation

Submitted to the Faculty of the

Graduate School of Vanderbilt University

in partial fulfillment of the requirements

for the degree of

DOCTOR OF PHILOSOPHY

in

Chemistry

May 8th, 2020

Nashville, Tennessee

Approved:

Janet E. Macdonald, Ph. D

Timothy P. Hanusa, Ph. D

Sandra J. Rosenthal, Ph. D

Piran R. Kidambi, Ph. D

Dedication

To my lovely wife and family, thank you for everything

Acknowledgements

This work was supported financially by the Department of Chemistry at Vanderbilt University, National Science Foundation grant numbers CHE-1253105 and EPS-1004083, Department of Education Graduate Assistance in Areas of National Need (GAANN) Fellowship 9200A140248. Portions of this work were performed at the Vanderbilt Institute of Nanoscale Science and Engineering, using facilities renovated under TN-SCORE (DMR 0907619) and NSF EPS-1004083.

I would like to thank Dr. Janet Macdonald for welcoming me into her group. As a student that has always struggled with confidence during my time in grad school, I can't thank you enough for always being supportive, encouraging, and understanding. Your curiosity and enthusiasm for chemistry has been inspirational to me, and I am proud to have been a member of the Macdonald Lab. I would also like to thank Dr. Timothy Hanusa, Dr. Sandra Rosenthal, Dr. Piran Kidambi, and Dr. Rizia Bardhan for supporting me and serving on my dissertation committee.

I am grateful for my time in the Macdonald Lab and all the members past and present. Emil, you were the best post-doc any one could ask for, you really brought everyone together. Suresh, thank you for always being willing to help out. Mike, I don't think I've met anyone as excited and up to date on the latest literature as you, definitely helpful advice. Shane, thank you for your support and for teaching me the basics of using our electrochemistry set up. Andrew, you were easily the go-to guy for anything synthesis related, thank you for all you help. Alice the Macdonald Lab prodigy, you were always a big inspiration for just how easy you made grad school look. Evan, we've been in all the same rotations and lab from day one, and it has been an honor man. On the rare occasions when I didn't have my headphones on you always had the best advice,

encouragement and perspective on life. Wishing you and your family the best! Stephanie, I'm glad to see you find you way with Phuture Doctors, keep on going! Maddy, Chris, and Nathan, the Macdonald Lab is definitely in good hands with such bright scientists as you three. I know all three of you will continue on to have great success here at Vanderbilt and beyond. I would also like to thank the TEM guru James McBride for all your help with the TEM imaging and training, and especially for the STEM-EDS tomography. Thanks also VINSE personnel Dmitri Koktysh and Anthony Hmelo. Big thank you to Don Brunson for introducing me to the Vanderbilt graduate program. And lastly, I want to thank everyone at Rider University that helped expose me to the possibility of pursuing a doctorate as well as the necessary steps to get there. I am grateful for the Ronald E. McNair program and Angelica Benitez, as well as mentors and professors Dr. Feng Chen, and Dr. Danielle Jacobs.

To my parents, Sonya and Joseph, words cannot thank you enough. Mom, your love and hard work and sacrifice for all five of us was truly inspirational. Dad, thank you for all of your encouragement, support, and sharing of your wisdom. Thank you to my grandma, Johanna for helping to raise us five kids when we were younger. Thank you, Rico for all the support. Joey, you are the best big brother I could ask for. Maya, I am proud of you and know that you will discover your path. Owen, probably the coolest out of all of us, I'm proud of you and seeing the man you have become. Sierrah, I am glad you found your passion, keep going Bird! To my wife, Wilenny, thank you for being there every step of the way. You have been my biggest supporter even when I doubted myself. You are my best friend and the love of my life. I love you with all my heart. Finally, and most importantly, I thank God for blessing me so abundantly, as I can accomplish nothing without His grace and mercy.

Table of Contents

List of Figures

Figure **Page**

Chapter 1

Introduction

1.1 Broader impacts/Research Motivation

One of the most pressing issues that our society faces today is the impact that our energy generation and consumption has on our environment. As of 2018, the US alone still heavily depends on nonrenewable carbon generating energy sources such as fossil fuels. Despite the significant efforts in developing alternative energy sources, non-renewable sources still dominate. In a report by the U.S. Energy Information Administration released its annual energy review which reported that over 80% of our national energy consumption was sourced from nonrenewable sources such as petroleum, coal, and natural gas, while less than 10% of energy consumed last year was from renewable sources (**Figure 1.1**). With a global energy demand of 18 TW per year,[1] solar

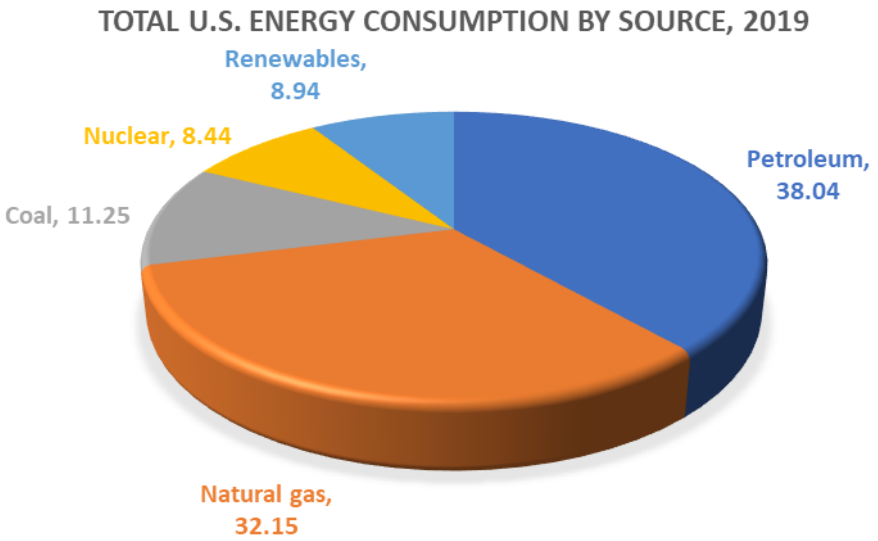

Figure 1.1: U.S. Energy Information Administration's annual energy review for total U.S. energy consumption by source, February 2020.

energy is distinguished amongst the renewable energy sources as a near infinite source of energy, with 120,000 TW striking the surface of earth annually, relative to the energy that can potentially be provided by hydroelectric (2.5 TW), geothermal (12 TW), and wind (2-4 TW).[2] Despite being a near infinite source, solar energy only accounted for less than one percent of energy consumed in the U.S. last year. Current solar technology must greatly improve before it can compete with and eventually replace non-renewable sources.

While the issue of finding viable alternatives to the current societal dependence on nonrenewable energy sources is a monumental task, scientists have turned their focus to nanoscale solutions. Nanocrystalline materials have several advantages over their bulk counterparts. At the nanoscale materials have a much higher surface-to-volume ratio, a property that is especially useful for catalytic applications and energy storage, as well as unique optoelectronic properties such as quantum confinement.[3] In order to take full advantage of the potential of nanotechnology, a deep understanding of the factors that contribute to the formation of high-quality nanocrystals is imperative. The following introductory sections will establish the fundamentals of synthesizing nanocrystals, specifically focusing on wet-chemical colloidal methods.

1.2 Colloidal Nanocrystal Synthesis

The main focus of this dissertation is the synthetic aspect of preparing nanocrystals, so a basic understanding of key concepts of nanocrystal synthesis is necessary. In wet-chemical colloidal synthesis of nanocrystals three fundamental ingredients are used, typically molecular precursors are used in conjunction with a reaction medium, typically an organic solvent, and organic molecules that function as ligands. When energy is added to the system in the form of heat, radiation, or mechanical energy the precursors dissociate into "monomers" which are the actual building units for nucleation and subsequent growth.

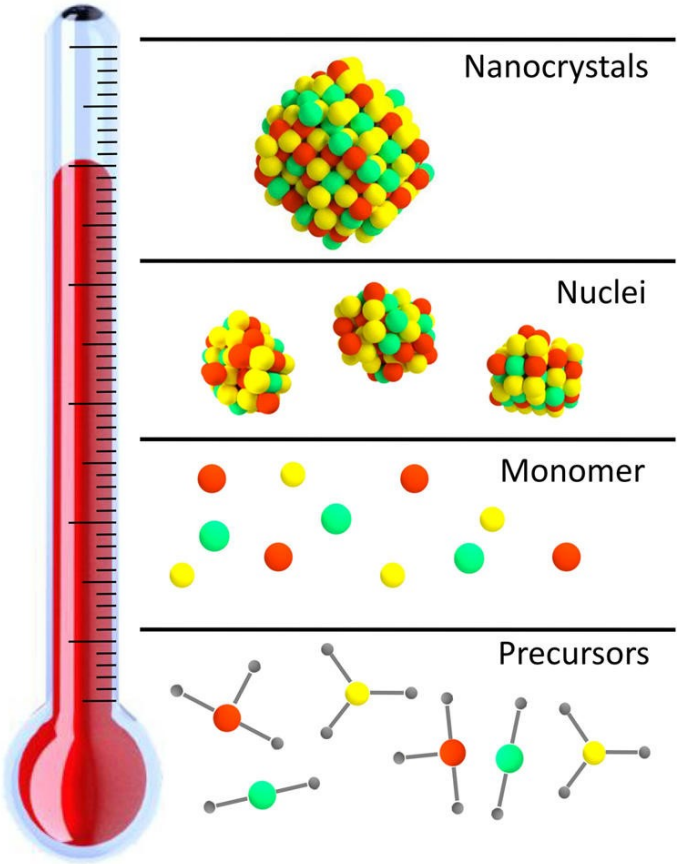

Figure 1.2: Heat up synthesis of nanocrystals. Adapted from ref [73] with permission. Copyright 2015 American Chemical Society

1.2.1 Nucleation theory

Nucleation theory in the classical sense takes a thermodynamic approach focusing mainly on the free energy associated with the formation of nanocrystals. Since nanocrystals consist of either bulk atoms or surface atoms, the total free energy (ΔG_T) of a nanocrystal is essentially the sum of the bulk free energy (ΔG_B) and the surface free energy (ΔG_S) as defined by the following equation.

$$\Delta G_T = \Delta G_B + \Delta G_S \tag{1.0}$$

For a spherical particle with radius r, the bulk free energy is defined as $\Delta G_B = (4/3\pi r^3)\Delta G_V$ where ΔG_V is the Gibbs free energy per unit volume. Given that ΔG_V can be further expressed as $\Delta G_V = -(k_B T/V_M) \ln S$, and the surface free energy is defined as $\Delta G_S = 4\pi r^2 \gamma$, the total Gibbs free energy for a spherical particle can be established by the following relationship:

$$\Delta G_T = -\frac{4\pi r^3 k_B T \ln S}{3V_M} + 4\pi r^2 \gamma \tag{1.1}$$

where k_B is Boltzmann's constant, T is temperature, S is the level of supersaturation, V_M is the molar volume of the monomer, and γ is the surface energy between the particle and solution. An examination of Equation 1.2 above reveals that the energy associated with forming volume is

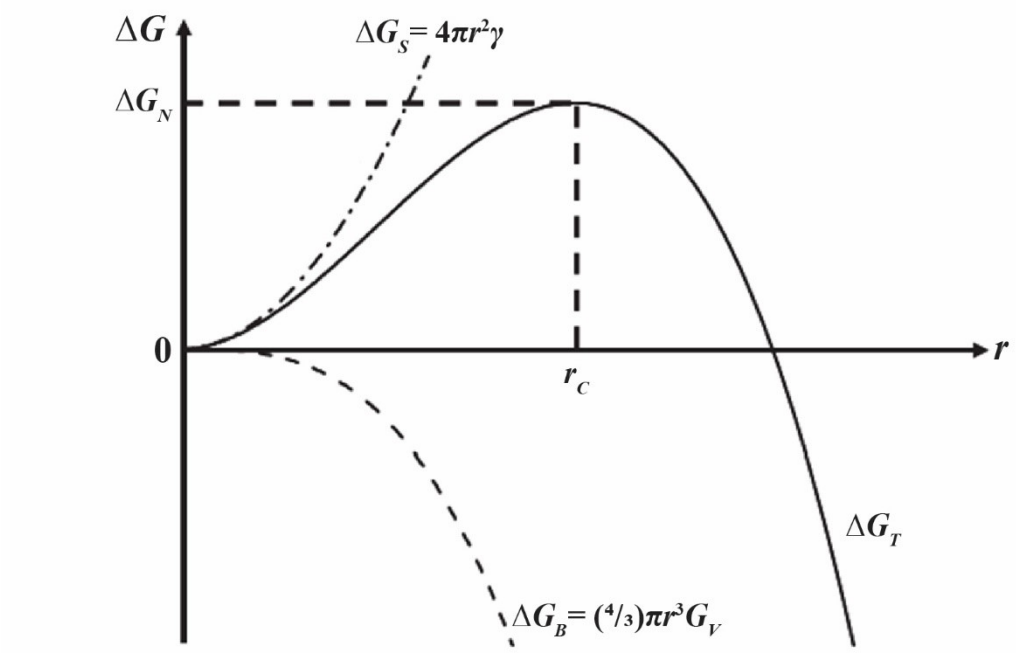

Figure 1.3: Surface (ΔG_S), bulk (ΔG_B), and total (ΔG_T) free energy contributions as a function of radius for an arbitrary spherical particle system. Adapted from ref [4] (Copyright Wiley-VCH Verlag GmbH & Co, 2011)

always negative, hence energetically favorable for the total free energy of the system, while the energy associated with the formation of surface area is a positive contribution to the overall free energy, hence energetically unfavorable. In **Figure 1.3** the total free energy ΔG_T (solid line), bulk contribution ΔG_B (dashed line), and surface contribution ΔG_S (dotted line) are included in the plot.

A few key observations can be made from **Figure 1.3**. At the smallest sizes the total free energy is dominated mainly by the surface contribution, due to the high surface to volume ratio of the particle. As the particle grows in size the bulk free energy contribution increases, and there exists an energetic maximum in ΔG_T that is defined as the critical point, which is the smallest possible particle radius that can form and remain stable in solution. This energy barrier is known

as the free energy of nucleation (ΔG_N), and can be calculated by setting the derivative of $d\Delta G_T/dr$ to zero:

$$\Delta G_N = -\frac{16\pi\gamma r^3 V_M}{3{k_B}^2 T^2 (\ln S)^2} \tag{1.3}$$

The corresponding particle size at the total free energy maximum is the critical radius (r_c) which is determined by the following equation:

$$r_C = -\frac{2\gamma V_M}{k_B T \ln S} \tag{1.4}$$

Below the critical radius is the meta stable regime in which nuclei will tend to dissolve in order to lower their total free energy. Above the critical radius particle additional particle growth will stabilize the system.

Nucleation theory also takes into account the kinetics of nucleation. Using an Arrhenius type equation, the rate of nucleation can be described by the following equation

$$\frac{dN}{dt} = A \exp\left(-\frac{\Delta G_{crit}}{k_B T}\right) = A \exp\left(\frac{16\pi\gamma^3 {V_M}^2}{3{k_B}^3 T^3 (\ln S)^2}\right) \tag{1.5}$$

Where A is a pre-exponential factor. The key parameters that can be manipulated during experimentation are the level of supersaturation S, temperature T, and the surface free energy γ. In general, the level of supersaturation has the greatest impact on the rate of nucleate relative to the other two experimentally controllable factors. Kwon and Hyeon[4] demonstrated computationally using that by changing the level of supersaturation from S=2 to 4, the nucleation rate increased by a factor of 10^{70}. The impact of temperature is understated according to this model, as in practice nanocrystal reactions can be very temperature sensitive.

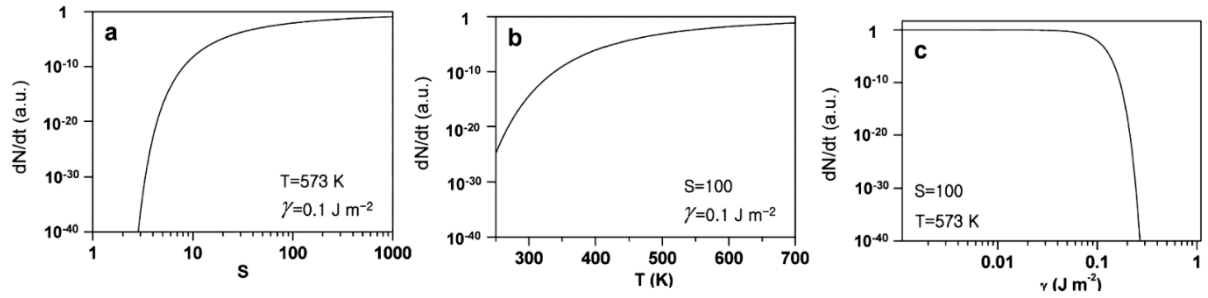

Figure 1.4: Nucleation rate as a function of a) supersaturation, b) temperatute, c) the surface energy calsulated using equation 1.5, with V_m as 3.39×10^{-5} m^3 mol^{-1}, the value for CdSe. Nulceation rate is normalized with pre-exponential factor A. Reproduced with permission from ref [4] (Copyright Wiley-VCH Verlag GmbH & Co, 2011)

1.2.2 LaMer Burst Nucleation

The concept of burst nucleation was first described by LaMer and Dinegar for the precipitation of monodispersed sulfur hydrosols from the slow decomposition of sodium thiosulfate in hydrochloric acid.[5] The most often cited and adapted component of their original study was the qualitative explanation of the particle growth process, which is included in **Figure 1.5**. In their model the nanocrystal formation process is divided into three stages in time: monomer accumulation, nucleation, and growth. In the monomer accumulation stage, Region I, the precursor converts to monomer over time beyond the point of saturation (C_S) until the minimum monomer

concentration required for nucleation is reached (C_{min}). In Region II nucleation occurs while the monomer concentration is increasing, until C_{max} is reached. At this point 'burst' nucleation takes place in which the rate of nucleation is higher than monomer production rate, so the net monomer concentration rapidly depletes until it falls below C_{min}. After the monomer concentration depletes below C_{min} in Region III new nuclei are unable to form, and only diffusion limited growth occurs until C_s is reached.

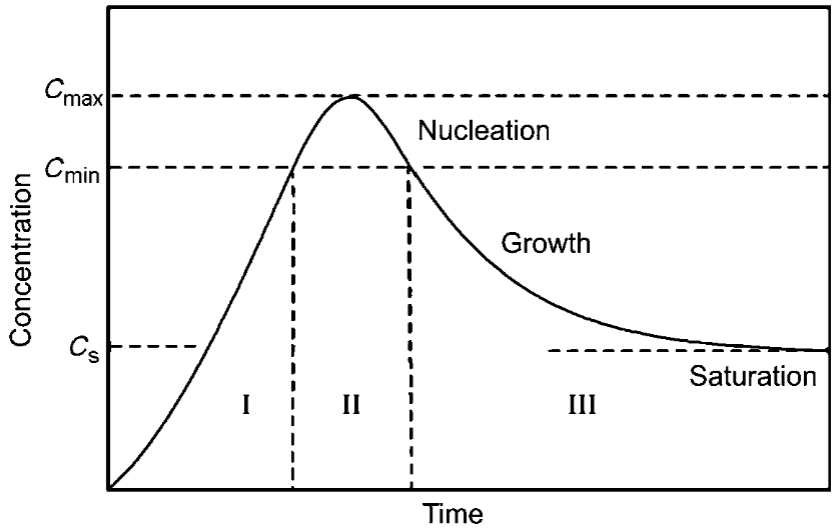

Figure 1.5. LaMer and Dinegar's qualitative model to describe nucleation and growth. Reproduced with permission from Ref 5

In a recent critique of the highly cited proposal by LaMer, Whitehead and coworkers[6] point out several shortcomings of how the model is cited in the literature as well as the model itself. It is important to note that while this model is widespread and commonly cited as an explanation for the precipitation of monodispersed crystals, the key assumptions of the model are rarely discussed and the actual differential equation from the original paper has only once been successfully fitted to experimental kinetic data despite the ubiquity in the literature. In short, the LaMer model is best

used as a conceptual tool to qualitatively generalize the nucleation and growth conditions that produce monodispersed nanocrystals, but certainly should not be cited as evidence for a given phenomenon in its "words only" form.

1.2.3 Ostwald Ripening and Size focusing/coarsening

In the event that monomer deposition on the surface of growing nanocrystals is a reversable process, a phenomenon called Ostwald ripening may occur. In a thermodynamically driven process to minimize high interface energy between particles and solution, smaller particles will dissolve and redeposit on to larger particles, but only occurs if the reaction is reversible. A characteristic sign of Ostwald ripening is an increase in average particle size as well as an increase in standard deviation.

1.3 Scope of dissertation

The focus of this dissertation will explore the importance of understanding the underlying chemistry of molecular precursors to target specific phases in nanocrystal synthesis. Chapter 2 highlights the iron pyrite system as a potential low cost, high natural abundant and non-toxic photo absorber material that has long been plagued with poor performance despite promising material properties. This chapter will provide a historical review and perspective of the main categories of issues related to the poor performance of pyrite in solar applications. Chapter 3 will highlight our attempt to address one of the longstanding issues regarding the synthesis of iron pyrite on the nanoscale, which is the poor understanding of all the factors that contribute to specific phase selection during the synthesis stage. Phase control as a function of sulfur precursor reactivity and

decomposition mechanism is one of the keys to selecting controlling the FeS phases obtained. Chapter 4 will highlight our attempts to address another issue with pyrite, which is poor control of surface states and doping. Nanocrystalline pyrite often has poor quality surfaces that tend to be p-type despite the tendency of high-quality pyrite single crystals to be n-type. The presence of a surface inversion layer due to sulfur vacancies and other types of defects are often implicated as the cause of poor performance, and our strategy to address this issue involves hybridizing with the isostructural cattierite. Chapter 5 will address further attempts and ideas to revisit the concept of intentional phase control by isolating the kinetics of precursor decomposition rates. This time instead of disulfides, thioethers, and sulfides, thioureas and thiophenols are explored. Thioureas and thiophenols may potentially isolate only the kinetic contributions to phase control as the extent of thiourea substitution affects the thiourea decomposition rate, while maintaining the same decomposition mechanism.

Chapter 2

The Allure of Iron Pyrite: Revolutionary Material or Fool's Gold?

Iron pyrite has been used by mankind for centuries whether it was for decorative jewelry, or as an alternative to flint for striking to create fire. The brassy yellow appearance of the mineral resembles gold to the untrained eye, hence the appropriate nickname of "fool's gold." While iron pyrite is virtually worthless in terms of monetary value, the potentially useful semiconducting properties of the mineral have been under investigation as early as 1874.[7] Many research applications include pyrite such as battery technologies, sensing applications, and photocatalysis,[8] but one area of interest that has intrigued researchers over the last few decades is the potential application of iron pyrite as a next generation photovoltaic material. In the modern-day clean energy rush, will pyrite emerge as a golden solution to the challenge of lowering the cost of solar devices? Or will it live up to its nickname as a promising lure at first glance but upon further appraisal end up worthless?

2.1 Photovoltaic application of iron pyrite

Pyrite has excellent optical properties for energy conversion from sunlight with an appropriate bandgap of 0.95eV (indirect, with direct transition at 1.03 eV) which is close to the Shockley-Quiesser limit for an ideal semiconductor,[9] as well as high electron mobility (μ = 360 $cm^2\ V^{-1}\ s^{-1}$) for single crystals and long minority carrier diffusion length (100-1000 nm). In addition, a high absorption coefficient of $\alpha > 10^5$ for $h\nu > 1.3$ eV means that an iron pyrite thin film would only have to be 20 nm thick in order to absorb 90% of sunlight vs crystalline silicon, which needs 300 μm to absorb the same amount [10] Not only would low rate of material

consumption be required, but pyrite itself is already an earth abundant, inexpensive, and nontoxic material. It is readily discarded as an unwanted byproduct of coal mining, and assuming a 10% cell efficiency and 5 μm thick active layer, the US primary power demand could be met with just a tenth of the pyrite that is disposed annually as mining waste in six states alone.[11] Furthermore, in a materials cost extraction vs. annual electricity potential analysis of 23 promising semiconductors for photovoltaics relative to crystalline silicon, iron pyrite stood out in a class of its own (**Figure 2.1**). According to this study back in 2009, a pyrite cell operating at only 4% solar conversion efficiency would be equally as cost effective as a 20% efficient crystalline silicon cell at the time in terms of lifetime energy output.[12] Even though the cost of silicon based cells has dropped considerably in the decade since (as low as $0.20/W in 2018 according to NREL),[13] pyrite photovoltaics would still have a high impact with only minimal progress in efficiency required.

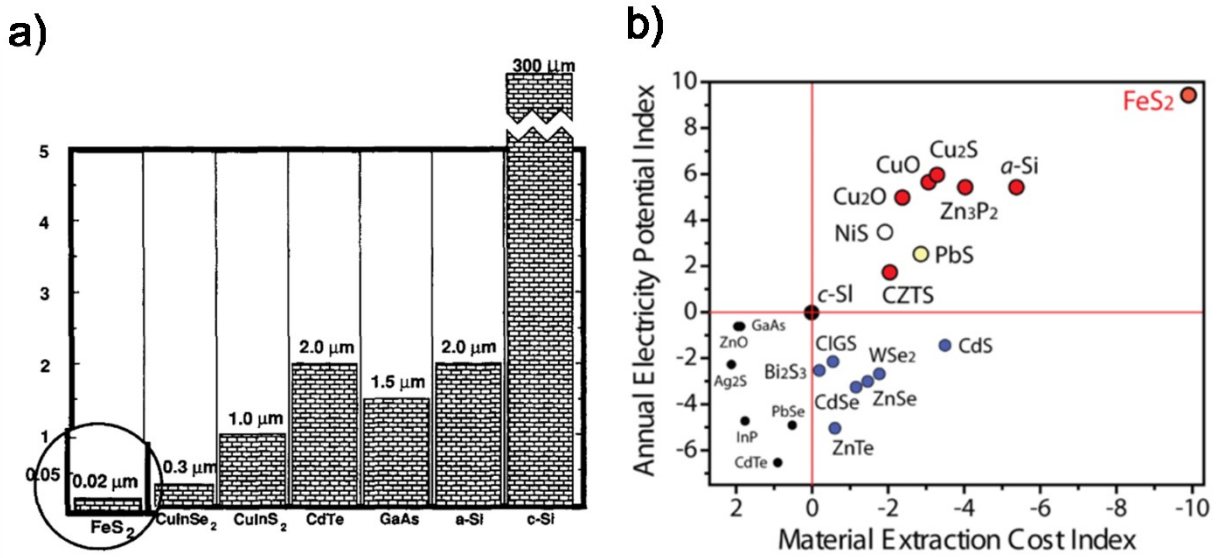

Figure 2.1: a) Comparison of film thickness of several semiconductors required to absorb 90% of sunlight based on absorption coefficient $L = 1/\alpha$. (Adapted from ref [10]) b) Cost benefit analysis in terms of material extraction cost (cents/watts) and annual electricity potential (TWh) of 23 semiconductors relative to crystalline silicon. (Original data of Wadia 2009, reformatting by Caban-Acevedo 2014).

Needless to say, all of these factors have made pyrite one of the most intriguing materials as a potential revolutionary material in the quest for inexpensive and solar cells in the past decade.

The efforts of Tributsch and coworkers established the groundwork for pyrite photovoltaic device research in the 80s and 90s. [10,14,23–26,15–22] They constructed the first pyrite photoelectrochemical and Schottky solar cells,[15] and also performed a number of studies to characterize the fundamental photoelectrochemical, photoconductive, and electronic properties of the material.[10] Despite pyrite devices demonstrating high quantum efficiencies (over 90%) and photocurrents (upwards of 40 mA cm^{-2}), they often demonstrated low photovoltages, typically less than 200mV equating to a solar conversion efficiencies under 3%.[26] Despite such promising properties and the fact that these pioneering studies for pyrite PVs have been conducted over three decades ago, not much improvement has been made in terms of increasing solar conversion efficiency. The same story of low open circuit voltage has plagued subsequent attempts of developing iron pyrite based solar cells. [27–30]

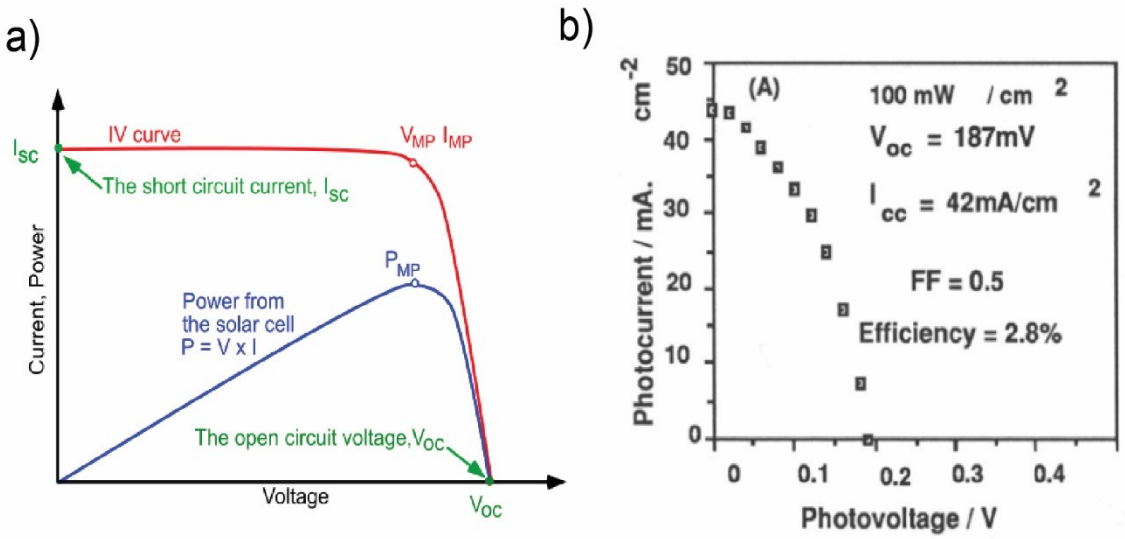

Figure 2.2: (a) generic IV curve for an arbitrary photovoltaic cell (PVEducation.org, accessed February 2020). (b) Record performing pyrite solar cell to date achieving an efficiency of only 2.8% (Adapted from ref[25] Copyright 1993, Elsevier).

2.1.1 Mystery of low open circuit voltage

The often-cited record performing pyrite photovoltaic device was reported by Ennaoui *et al.* in 1990,[26] which was a photoelectrochemical cell consisting of an n-type FeS_2 single crystal electrode and aqueous iodine/tri-iodide electrolyte (**Figure 2.2**b). The low efficiency of 2.8% was limited by the low open circuit voltage despite having a high short circuit current and moderate fill factor (V_{oc} = 187mV; I_{sc} = 42 mA/cm^2; FF = 0.50).[26] For comparison, a current state of the art n-type crystalline silicon cell was able to achieve an efficiency of 26.7% with nearly quadruple the open circuit voltage and an equivalent short circuit current (V_{oc} = 738mV; I_{sc} = 42.7 mA/cm^2; FF = 0.85).[31,32]

In order to understand the information that a low open circuit voltage can reveal about the quality of the photoactive material, a brief discussion about solar cell operational parameters is warranted. When evaluating the efficiency of a solar cell the following equation is used:

$$\eta = \frac{V_{OC} I_{SC} FF}{P_{in}}$$

where V_{oc} is the open circuit voltage, I_{sc} is the short circuit current, FF is fill factor, P_{in} is input power, and η is efficiency. The standard P_{in} for efficiency calculations is typically 100 mW/cm^2 to simulate sunlight, and the other parameters can be extracted from an IV curve (**Figure 2.2**a) where the I_{sc} is the maximum current at zero voltage, V_{oc} is the maximum voltage at zero current, and fill factor is the relative "squareness" of the IV curve. Focusing on V_{oc} specifically, open circuit voltage can be calculated by setting the net current equal to zero in the solar cell equation:

$$V_{OC} = \frac{nkT}{q} \ln\left(\frac{I_L}{I_0} + 1\right)$$

Where n is the ideality factor, k is Boltzmann's constant, T temperature, q charge of electron, I_L light generated current and I_0 dark saturation current. The key variables that affect V_{oc} are the light I_L and dark saturation I_0 currents. Dark saturation current depends on charge carrier recombination and can vary by orders of magnitude, so the V_{oc} is essentially a measurement that reflects the amount of charge recombination in a solar cell. When studies arrive at the conclusion that pyrite-based photovoltaics are limited by low open circuit voltages, the implication is that the extent of charge recombination in pyrite solar cells is high. While there is a consensus that low V_{oc} is the main limiting factor in pyrite PVs, the exact cause of a high rate of charge carrier recombination is up for debate. In the efforts to identify the fundamental issues regarding the source of the underwhelming performance and low V_{oc} of pyrite in photovoltaic devices, three main categories have been defined: surface and bulk defects, nature of unintentional doping, and concerns about phase purity. [33–35]

2.1.2 Concerns about pyrite nonstoichiometry and bulk defects

Understanding the true extent of pyrite nonstoichiometry has been a point of contention amongst researchers. It is often observed that both natural and synthetic pyrite samples can deviate from ideal stoichiometry of FeS_{2-x} with x as high as 0.25.[36] The sulfur deficiency has historically been interpreted as sulfur vacancies (V_S) such as simple Schottky defects, in which the pyrite unit cell remains intact with missing sulfur atoms. The implications of sulfur defects in the pyrite crystal structure were investigated by Birkholz *et al*.[37] In their early model the sulfur vacancy is presumed to be a simple Schottky defect, which would have implications on the local coordination environment where the oxidation states can change in order to preserve net charge neutrality. For every sulfur vacancy four bonds are broken: three S-Fe bonds and one S-S bond. The formal charge

of -1 for the sulfur in the original S_2^{2-} unit becomes S^{2-} for the remaining sulfur as a result of the vacancy. Upon examination of the coordination environment of an Fe atom in the pyrite structure, the FeS_6 coordination becomes FeS_5 as a result of a sulfur vacancy, and a local symmetry reduction from O_h to C_{4v} occurs as the octahedral coordination becomes tetragonal pyramidal. This symmetry reduction results in a change in the splitting of Fe 3d orbitals in accordance to ligand field theory (Figure 2.3). The effect of sulfur vacancies on the electronic properties of pyrite was considered in early models of the pyrite band structure. Early studies suggested that the formation of states within the band gap could be the result that could function as trap states, although the exact position and width of this defect band is still up for debate.[35,37]

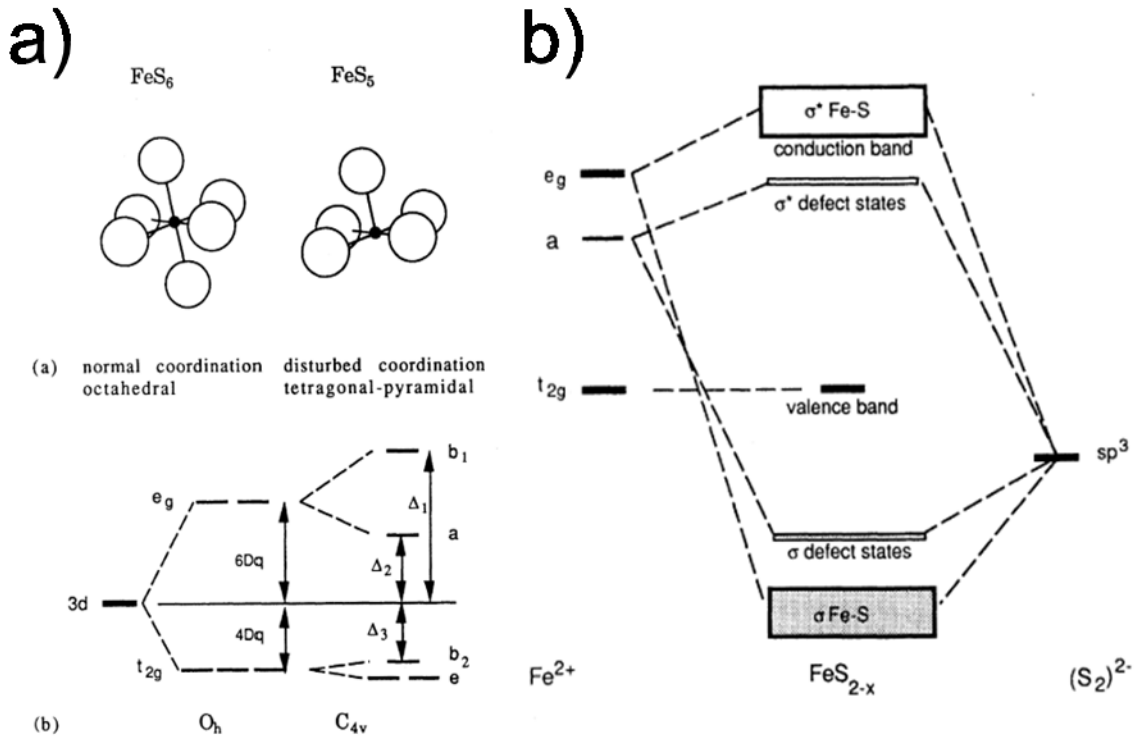

Figure 2.3: a) Reduction in symmetry of O_h to C_{4v} as a result of sulfur vacancy in $FeS_6 \rightarrow FeS_5$ and the resulting ligand field splitting. b) Proposed effect the defect states would have on the pyrite band diagram. Adapted with permission from ref 10.

Computational studies have called into question the idea of bulk sulfur vacancies as the cause of the apparent sulfur deficiency in pyrite samples. In a 2011 study by Yu *et al*., the argument is presented that based on computational evidence that the barrier for bulk sulfur vacancy formation is almost prohibitively high at 2.4 eV, so vacancy formation at bulk would be unlikely.[38] Other calculations of V_S formation energy are also in good agreement with values in the range of 2-3.5 eV.[39–41] Hu *et al*.,[39] however, cautions that DFT studies can tend to overestimate defect formation energies, citing the well-known case of prevalent oxygen vacancies in metal oxides despite high calculated defect formation energies of ~3.0 eV.[42] The computational consensus that bulk V_s defect formation energy is high seems to be supported by recent experimental studies that

establish that pyrite is essentially a stoichiometric compound.[43] Using in-situ high resolution XRD and relevant standardization techniques, McAuliffe and Shoemaker determined that pyrite has inflexible stoichiometry with no significant changes in lattice parameter, and that sulfur deficient samples result from the formation of pyrrhotite phases.[43] While secondary phases are often undetected via XRD analysis, their presence can be inferred by sensitive magnetic measurements, where perfectly stochiometric pyrite would be diamagnetic, but substoichiometric or impurity samples exhibit magnetism.[44,45]

Currently there is no direct correlation between pyrite S:Fe stoichiometry and its electrical properties.[46] Furthermore, early studies of photovoltage as a function of stoichiometry established no clear pattern and surprising results were observed such as $FeS_{1.88}$ achieving higher measured photovoltages than $FeS_{1.93}$.[47] At the moment the verdict on pyrite bulk nonstoichiometry is not yet final, but the growing consensus is that it is not the main culprit of low open circuit voltage in pyrite devices.

2.1.3 Surface related issues

The first clues that pointed to the poor surface quality of pyrite samples early on was the effect that surface treatment had on photoconductive response measurements. Natural pyrite samples tend to show little or no photoconductive response,[48] but in the early attempts at constructing pyrite based photovoltaic devices, Büker and coworkers[20] noted the importance of surface treatment in their n-type pyrite single crystal samples, both natural and synthetically grown via chemical vapor transport (CVT) methods. A photoconductive response was only evident after polishing and surface treatment via electrochemical etching with a $HF/CH_3COOH/HNO_3$ solution, while samples that were tested as prepared or only polished always produced ohmic characteristics

Table 0-1. Overview of previously published literature results on the synthesis of FeS_2 highlighting defect model, synthesis method, characterization techniques used, and purpose of paper presented in the work., (Reproduced from Ref [43] with permission of the International Union of Crystallography)

Proposed defect	Synthesis	Characterization	Purpose of study	Citation
Non-stoichiometry due to sulfur vacancies				
Sulfur vacancies	CVT-Br	ICP-AES, XRD	Stoichiometry of FeS_2	Birkholz *et al.* (1991)
Sulfur vacancies	CVT-Br	XRD, density, TEM	Stoichiometry of FeS_2	Fiechter *et al.* (1992)
Sulfur vacancies	Iron sulfidation	XRD	Thin-film microstructure	de las Heras *et al.* (1996)
Common defects in CVT growth				
Sulfur vacancies, Br incorporation	CVT-Br	ICP-MS, ICP-AES	Purity of synthetic FeS_2 crystals	Luck *et al.* (1989)
Br incorporation	CVT-Br	ESR	Effect of transport agent	Siebert *et al.* (1989)
Common defects in thin-film growth				
Sulfur interstitials, iron vacancies	Steel sulfidation	XRD, Raman	Nanowire growth	Cabán-Acevedo *et al.* (2012)
C,H,O incorporation, marcasite impurity	APCVD	XRD, Raman, Auger, SIMS, RBS, XPS	Thin-film growth	Berry *et al.*(2012)
Marcasite impurity	Thermal sulfidation	Raman	Thin-film growth	Kim *et al.* (2016)
$Fe_{1-x}S$ impurity	Thermal sulfidation	WAXRD, Raman, EDS	Thin-film stoichiometry	Zhang *et al.* (2015)

Abbreviations: **CVT-Br** Chemical vapor deposition with bromine; **ESR** electron spin resonance spectroscopy, **TEM** transmission electron microscopy, **APCVD** atmospheric pressure chemical vapor deposition, **RBS** Rutherford backscattering spectroscopy, **WAXRD** wide-angle X-ray diffraction

and failed to demonstrate any photoactivity.[20] Liu *et al.* also demonstrated that photoelectrochemical oxidation of KCl on a pyrite single crystal electrode surface significantly improved photocurrent response, as well as decreased dark current, a sign of reduced carrier recombination.[49] More recently in the case of pyrite nanocrystalline thin films, surface treatment by way of surfactants was also demonstrated to impact photoactivity. Bi *et al.*[28] demonstrated that pyrite nanocrystals with trioctylphosphine (TOPO) ligands were able to show a photoconductive response to standard terrestrial air mass (AM 1.5) illumination as a result of surface passivation, with the added benefit of improved stability to oxidation in air for up to a year.

Prompted by the apparent connection between surface treatment and improved photoactivity, researchers have sought to further understand the nature of pyrite surfaces, which are not particularly known for their stability. In mining, oxidative decomposition of pyrite surfaces results in loss of sulfur as sulfuric acid in the phenomenon of acid mine drainage.[50] The S-terminated (100) surface is the most common surface termination as well as cleavage plane. One of the leading theories that has been proposed relates to the instability of sulfur on the surface,

namely the formation of sulfur vacancies. The (100) pyrite surface can be cleaved in such a way that either the Fe-S bond breaks or the S-S bond. When the Fe-S bond is cleaved a charge neutral situation results with Fe^{2+} and $(S_2)^{2-}$ but when the persulfide unit breaks it results in Fe^{2+} and S^{1-}. In the latter case the S^{1-} monomers may convert to the more stable S^{2-} in one of the following ways: $Fe^{2+} + S^{-1} \rightarrow Fe^{3+} + S^{2-}$ or $2S^{1-} \rightarrow S^0 + S^{2-}$. Computations have shown that sulfur vacancy formation on the (100) surface has a low defect formation energy (~0.4 eV).[38,51] This surface vacancy formation has been linked to a number of interconnecting issues including surface conductive states, surface inversion layers, surface nonstoichiometry, surface defects, deep trap states, and reduced surface band gap. [10,20,55–58,28,34,38,46,51–54] In one of the most comprehensive studies by Walter *et al.* a detailed investigation of over 120 samples of CVT grown n-type FeS_2 single crystals demonstrate that a surface p-type inversion layer is present with a thickness limit of ~3nm, which can be suppressed by polishing.[55]

2.1.4 Phase impurities

The presence of secondary iron sulfide phases has also been a cause for concern in pyrite-based photovoltaics. Pyrite formation is often accompanied by these phases as many of them serve as intermediates for pyrite formation, as well as many are the products of pyrite decomposition. Marcasite, the orthorhombic polymorph of pyrite, was identified early on as a potential detrimental phase due to its small band gap of 0.34 eV.[59] But more updated studies have provided evidence to the contrary to the conventional wisdom where the band gap of marcasite was actually much closer and comparable to pyrite than previously thought.[46,60,61] Furthermore, the intentional inclusion of marcasite has been shown to improve photoresponse of pyrite films.[61,62] Other S-deficient iron

sulfides such as greigite, pyrrhotite, and troilite still remain as concerns due to their metallic nature,[34] so developing pure phase syntheses to pyrite remains a priority.

2.2 Pyrite formation mechanisms

2.2.1 The Fe-S crystalline system and pyrite precipitation in nature

The iron-sulfur based minerals are amongst the most earth abundant naturally occurring transition metal chalcogenides and they play vital roles in natural processes such as the environmental sulfur cycle.[63] There have even been theories that iron sulfides could have played a key role in the origin of life on earth, serving energy sources for sulfur metabolizing bacteria in anoxic hydrothermal ocean vents.[64]A diversity of chemical and physical properties are present in iron sulfides where, depending on the phase, they can exhibit metallic or semiconducting behavior, and demonstrate a range of magnetic behavior such as diamagnetism, antiferromagnetism or ferrimagnetism.[64]

In addition to pyrite, the iron-sulfur crystalline system includes another six naturally occurring phases, namely, mackinawite, troilite, pyrrhotite, smythite, greigite, and marcasite. Vaughan and Lennie in the early 90s extensively investigated the iron sulfur system and identified the relationship between phases.[64] Above 350°C the relationships are straightforward and well understood, but below that temperature a greater level of complexity is introduced due to the behavior of the many pyrrhotite phases based on ordered vacancy superstructures, as well as the presence of metastable phases such as greigite and marcasite that are rarely observed in nature but often observed in synthetic experiments.[64]

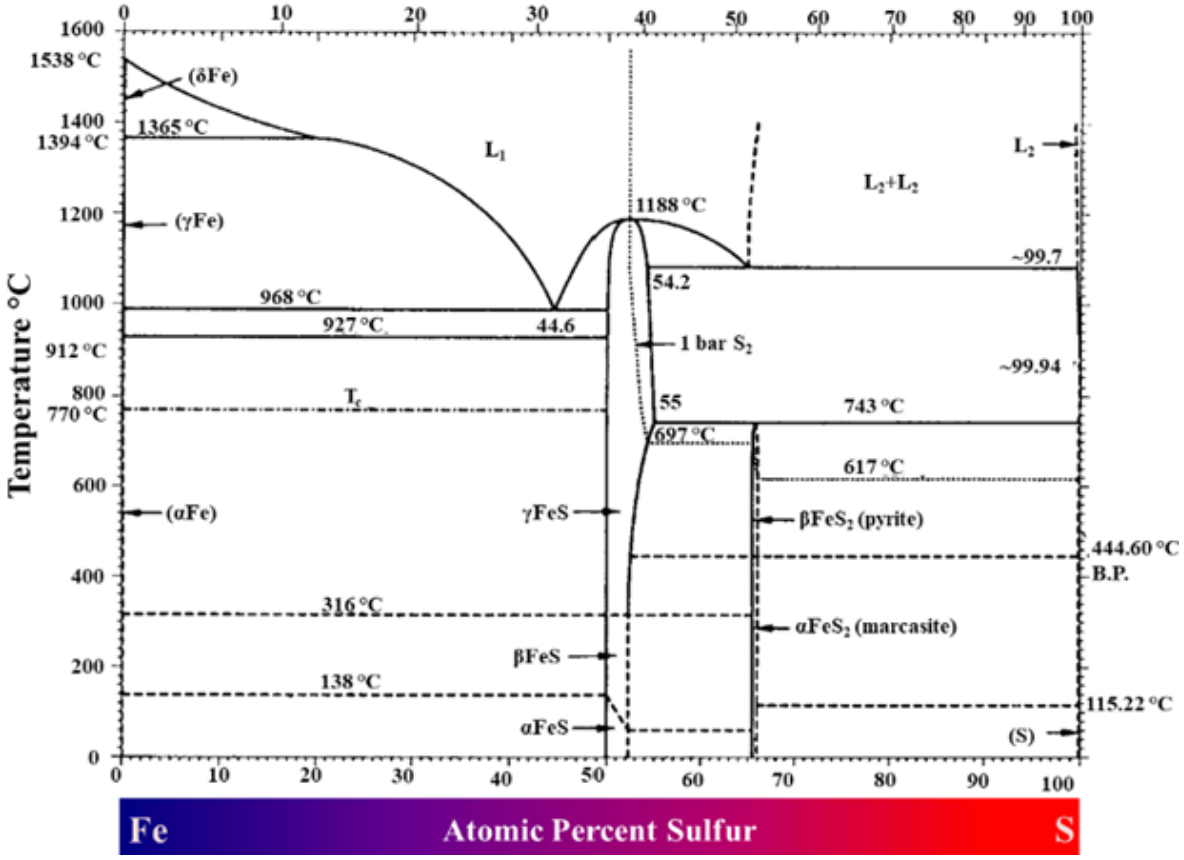

Figure 2.5. Phase relations in the Fe-S system. Reproduced with permission from ref [10] Copyright 1993 Elsevier Ltd.

Pure phase pyrite formation is made difficult by two factors, namely, the low temperature stability of the multiple iron sulfide phases with lower S/Fe ratios than pyrite mentioned previously, as well as presence of S_2^{2-} units inherent to the pyrite crystal structure. The dimeric S_2^{2-} structural units are problematic because there are not many common precursors found in natural pyrite forming environments that can decompose to directly supply the persulfide units. As a result, pyrite formation in nature is often the result of the sulfidation of the other sulfur poor Fe-S phases such as mackinawite, pyrrhotite, and greigite.[63,65–67]

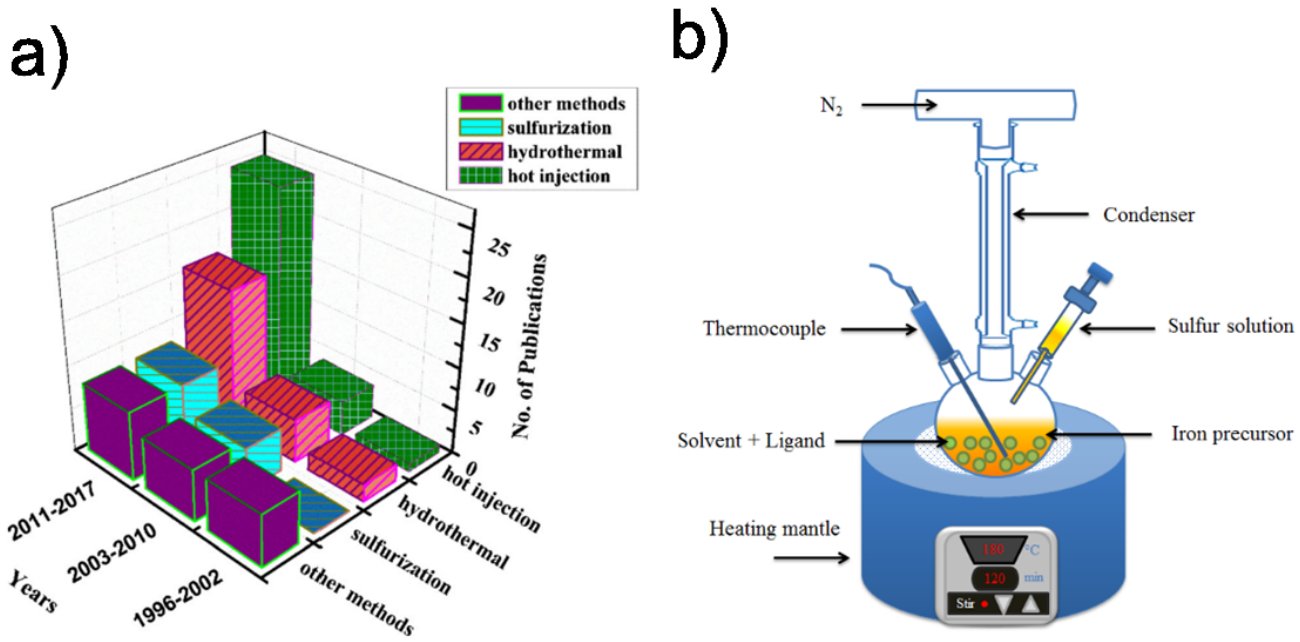

Figure 2.6: A) Research tends in the field of FeS_2 nanomaterials synthesized using different approaches. Adapted from ref [8] with permission. Copyright 2019 Springer. B) Typical hot injection synthesis of FeS_2 nanocrystals, adapted from ref [69] with permission Copyright 2018 Wiley.

2.3 Synthetic methods to pyrite formation

Much of the early work reported in the previous sections discussed results obtained with single crystal pyrite samples. Pyrite single crystals have been synthesized mostly by vapor phase methods such as CVT,[36] MOCVD,[68] and spray pyrolysis.[24] However, the field of pyrite research has undergone a pivot toward the synthesis of nanoscale structures and films during the past decade (**Figure 2.6**: A) Research tends in the field of FeS_2 nanomaterials synthesized using different approaches. Adapted from ref [8] with permission. Copyright 2019 Springer. B) Typical hot injection synthesis of FeS_2 nanocrystals, adapted from ref [69] with permission Copyright 2018 Wiley.). The

cost effective and highly tunable nature of colloidal reactions has revitalized the interest in pyrite research. The Law group reported the first synthesis that utilized hot injection for the precipitation of spherical pyrite nanocyrstals.[11] Utilizing mainly hot injection, hydrothermal, and solvothermal methods, numerous reports of size, morphology, and shape control have emerged, leading to finer control of the resultant pyrite nanocrystals.[69]

2.4 Where this thesis fits in the big picture

The fundamental studies on iron pyrite nanocrystals are imperative in order to further our understanding of the material and its complex behavior. While the synthesis of single crystals is ideal for lab research and fundamental studies, the utilization of single crystals in commercial applications is not quite as practical. In terms of cheap processability, colloidal nanocrystal pyrite thin film-based devices are a more commercially viable option. In the Macdonald lab, we specialized in the colloidal synthesis of semiconducting nanocrystals. As such we are well equipped to develop syntheses to produce and manipulate nanocrystal materials. The work presented in this thesis will address the factors that contribute to phase control in the iron sulfide system in colloidal nanoscale syntheses. Additionally, the surface of pyrite nanocubes is addressed by introducing epitaxially grown CoS_2 layers to promote pyrite functionality in catalytic applications.

Chapter 3

Phase-Controlled Colloidal Syntheses of Iron Sulfide Nanocrystals via Sulfur Precursor Reactivity and Direct Pyrite Precipitation[a]

3.1 Introduction

While many colloidal syntheses to first row transitions metal sulfides are known,[70–73] there is little rational control of the resultant phase. In particular, the iron sulfides provide one of the greatest challenges for phase-selective colloidal synthesis. Of the naturally occurring metal sulfides, the iron sulfides are the most earth abundant. However, relative to other metal chalcogenides, the iron−sulfur system is poorly understood due to its complexity as numerous phase variations arise from minimal changes in stoichiometry below 350 °C.[64]

There are seven major iron sulfide phases: iron pyrite (cubic FeS_2), marcasite (orthorhombic-FeS_2), greigite (Fe_3S_4), the pyrrhotite group ($Fe_{1-x}S$), troilite (FeS), mackinawite ($Fe_{1+x}S$), and cubic FeS.[63,64] The most stable and abundant phase is pyrite, which has a NaCl-type structure with Fe^{2+} and persulfide (S_2^{2-}) components. Pyrite is employed in battery technologies[74] and is of particular interest for photovoltaics as a semiconductor with a bandgap of 0.95 eV.[10] In contrast, metastable greigite has a widespread natural occurrence as the sulfur analogue of magnetite (Fe_3O_4). Greigite has an inverse spinel-type structure with fcc packed S^{2-} ions, Fe^{2+} in 1/8th of the tetrahedral sites, and mixed Fe^{2+} and Fe^{3+} in the octahedral sites. Greigite has garnered interest as a ferrimagnet,[75] as a supercapacitor,[76] and as a biomimetic catalyst since greigite-like clusters are common in biological enzymes.[77,78] The pyrrhotite group of iron sulfides, which have

[a] Portions of this chapter have been previously published in Rhodes, J. M. et al., *Chem. Mater.*, **2017**, 29, 8521-8530.

attracted attention for use in Li-ion batteries,[79] comprise of NiAs-type structures with varied ordered iron vacancies, leading to numerous polytypes. The monoclinic pyrrhotites are the most iron deficient, followed by hexagonal pyrrhotite and troilite FeS as the stoichiometric endmember.[63] Since the crystal phase is a major determinant of the properties of iron sulfides, understanding how the phase can be controlled in colloidal syntheses is of vital importance when designing iron sulfides for specific applications.

The ability to synthesize a select iron sulfide requires a thorough understanding of the factors that contribute to the formation of each crystalline phase. Two notable differences between iron sulfide phases are the stoichiometric iron/sulfur ratio and the variability of oxidation states for both iron (Fe^{2+} and Fe^{3+}) and sulfur (S^{2-} and S_2^{2-}). Many studies have evaluated the effect of temperature, reaction time, precursor concentration, iron precursor oxidation state, solvent, and ligands on the product phase.[11,80–85] Fewer studies have evaluated the effect of the sulfur precursor on the resultant crystalline phase as elemental sulfur is most widely used in colloidal hot injection syntheses.[86] Other sulfur sources such as dialkyldithiocarbamates,[87] L-cysteine,[88] and cubane type Fe−S complexes[89] have been used but are far less common. Despite these earlier studies, a comprehensive and predictive route to phase-pure products of the iron sulfides is needed.

The strategy of systematically replacing the chalcogenide and phosphide precursors used while maintaining all other reaction conditions has been recently used as a tool to manipulate the outcome of various nanocrystal syntheses.[90–92] By modulating the reactivity via changing the substitution of various chalcogenide and pnictide molecular precursors, fine control of size, dispersion, morphology, composition, and crystalline phase was achieved for CdS, CdSe,[93,94] PbS,[95] and nickel phosphide systems.[96] This type of study is an unexplored methodology for the

iron sulfides and could provide an efficient platform to gain insight into the relatively poorly understood iron sulfide system.

More than a screening of precursors is desired. Studies are beginning to show that unique reactions and decompositions in the organic reagents can be an invaluable source of information to understand how and why size, dispersion, morphology, composition, and phase are controlled. As an example, Qiao et al. recently demonstrated how the decomposition products of the benzyl ether solvent influenced the size and shape of magnetite nanocrystals.[97] A similar attention to detail is required when comparing organosulfur reagents.

In this study, the phase-selective and phase-controlled synthesis of Fe_xS_y nanoparticles is reported. The reactivity of various alkyl-substituted disulfides, thiols, and thioethers as sulfur sources is exploited to produce phase-pure FeS_2, Fe_3S_4, and Fe_7S_8 nanoparticles. Bond strengths of the organosulfur precursors (derived from computation) correlate with product trends observed but only partially explain the phase selectivity. Further chemical analysis of the precursor decompositions provides mechanistic details of the phase selection. The focus is particularly on determining the organic transformations that cause allyl disulfide to yield pyrite, as it is a reagent potentially capable of directly supplying S_2^{2-} units, a key feature in the pyrite structure. Evidence is provided which suggests that direct pyrite precipitation occurs when using allyl disulfide, an alternate route to the conventional mechanism which involves the nucleation of iron monosulfide intermediate species followed by further sulfidation to form pyrite, which is commonly cited.[63,80,98,99]

3.2 Experimental Methods

All glassware was oven-dried prior to use. Standard Schlenk line techniques were used in an inert N_2 atmosphere for all reactions. A J-KEM Scientific Model 210 temperature controller was used with a heating mantle for reaction temperature control. All reagents and solvents were used as received unless otherwise noted.

3.2.1 Materials

Anhydrous iron chloride ($FeCl_2$, 98%) was purchased from Strem Chemicals; sulfur flakes, allyl disulfide (Allyl-SS-Allyl, 80%), benzyl disulfide (Bz-SS-Bz, 98%), tert-butyl disulfide (t-Bu-SS-tBu, 97%), phenyl disulfide (Ph-SS-Ph, 99%), allyl mercaptan (AllylSH, 60%), tert-butyl mercaptan (t-Bu-SH, 99%), thiophenol (Ph-SH, 98%), diallyl sulfide (Allyl-S-Allyl, 97%), dibenzyl sulfide (Bz-S-Bz, 95%), di-tert-butyl sulfide (t-Bu-S-t-Bu, 98%), diphenyl sulfide (Ph-SPh, 98%), 1-octadecene (ODE, 90%), and oleylamine (OAm, 70%) were purchased from Sigma-Aldrich. Benzyl mercaptan (Bz-SH, 99%) was purchased from Fluka. n-Octylamine (OA, 99+%) was purchased from Acros Organics.

3.2.2 Characterization

TEM images and quantitative EDS measurements were acquired using a FEI Tecnai Osiris S/TEM operating at 200 kV with ChemiSTEM for EDS detection. Particle sizing measurements were taken in ImageJ. X-ray diffraction (XRD) patterns were acquired using a Scintag XGEN-4000 X-ray diffractometer with a CuKα ($\lambda = 0.154$ nm) radiation source. The resulting diffraction patterns were then visually compared to data from the JCPDS database to determine the structure.

Confocal Raman spectroscopy was performed on a Thermo DXR Raman microscope using 532 nm radiation at 0.2 mW power with a 100× objective, and a 50 μm pinhole aperture for an estimated spot size of 0.6 μm. UV−vis-NIR absorbance spectra were recorded on a Jasco V-670 spectrophotometer using quartz cuvettes. A baseline was first recorded without any reference cuvette, and then samples in $CHCl_3$ were recorded with a background of the neat $CHCl_3$ in the reference cuvette. NMR spectra were taken using a Bruker DRX-400 (400 MHz) spectrometer. Spectra were calibrated to residual solvent signals of 7.26 and 77.0 ppm for ^1H, respectively, in $CDCl_3$. GC-MS analysis was performed on a Varian Saturn 2100T GC/MS/MS. Separation of the components was accomplished using a SLB-5MS capillary GC column (Supelco, Bellefonte, PA, USA) 30 m × 0.25 mm i.d., 0.25 μm film thickness, and gradient oven program beginning at 40 °C, held for 3.5 min followed by heating to 250 °C with rate of 25 °C/min for a total run time of 19.90 min.

3.2.3 Synthesis of Fe_xS_y Particles

Several colloidal hot injection methods to synthesize pyrite nanocrystals[11,28,81,82,85] are derived from a general synthesis of metal sulfide nanoparticles,[72] in which a metal− alkylamine complex thermally decomposes in the presence of elemental sulfur. In this study, the general synthetic scheme is used differing only in the sulfur precursors used in order to evaluate the effect of sulfur precursor reactivity. [An atomic ratio of 1/6 Fe:S was maintained for each experiment, in which a 0.5/3.0 $FeCl_2$:sulfur precursor molar ratio was used (0.5/1.5 $FeCl_2$: R-S-S-R).] In a 25 mL 3-neck round-bottom flask, $FeCl_2$ (0.5 mmol) and 10 mL of OAm were placed under vacuum for 1 h at 60 °C. The temperature was increased to 170 °C and maintained for 1 h under an inert N_2 atmosphere. In a separate vial, an organosulfur precursor was dissolved in 5 mL of OAm and

placed under vacuum at room temperature for 45 min followed by backfilling with N_2 for 15 min. [The following sulfur precursors were used: Allyl-SS-Allyl (1.5 mmol, 0.217 mL); Bz-SS-Bz (1.5 mmol, 369.6 mg); t-Bu-SS-t-Bu (1.5 mmol, 0.287 mL); Ph-SS-Ph (1.5 mmol, 327.5 mg); Allyl-SH (3.0 mmol, 0.248 mL); Bz-SH (3.0 mmol, 0.352 mL); t-Bu-SH (3.0 mmol, 0.338 mL); Ph-SH (3.0 mmol, 0.308 mL); Allyl-S-Allyl (3.0 mmol, 0.386 mL); Bz-S-Bz (3.0 mmol, 643.0 mg); t-Bu-S-t-Bu (3.0 mmol, 0.542 mL); Ph-S-Ph (3.0 mmol, 0.502 mL); or elemental sulfur (3.0 mmol, 96.2 mg).] The S precursor/OAm solution was then injected into the reaction flask and heated to 220 °C for 2 h under N_2. The reaction solution was then cooled in air to room temperature, and ∼40 mL of chloroform was added, followed by centrifugation 5−10 min at 8000 rpm. Particles were further purified by two cycles of suspension with chloroform followed by ethanol (total ∼20 mL) and then centrifugation for 5 min at 4400 rpm. The particles were stored in chloroform.

3.2.4 Reactions of Disulfides with Octylamine

Disulfide/octylamine solutions were prepared by pipetting 12.0 mmol of octylamine and 12.0 mmol of an alkyl disulfide (allyl, benzyl, tert-butyl, or phenyl) in a 6-dram vial and sealed with a rubber septum and thermocouple. The solution was placed under vacuum for 30 min at room temperature followed by backfilling with N_2. Solutions were then heated to 130 °C for 2 h and then allowed to cool to room temperature, followed by analysis via GC-MS, ^{1}H NMR, and ^{13}C NMR.

3.2.5 Iron Sulfide Syntheses Using Allyl-SS-Allyl with Oleylamine/ Octadecene Cosolvent

In a 25 mL 3-neck round-bottom flask, $FeCl_2$ (0.5 mmol) and 10 mL of OAm/ODE were placed under vacuum for 1 h at 60 °C. [The OAm/ODE volume percentage was varied while keeping the overall solvent volume of 15 mL. OAm vol % used was 100, 93, 80, 66, 53, 40, and 20%.] The temperature was increased to 170 °C and maintained for 1 h under an inert N_2 atmosphere. In a separate vial, an Allyl-SS-Allyl was dissolved in 5 mL of OAm/ODE* and placed under vacuum at room temperature for 45 min followed by backfilling with N_2 for 15 min. The Allyl-SS-Allyl/ OAm solution was then injected into the reaction flask and heated to 220 °C for 2 h under N_2. The reaction solution was then cooled in air to room temperature, and ∼40 mL of chloroform was added, followed by centrifugation 5−10 min at 8000 rpm. Particles were further purified by two cycles of suspension with chloroform followed by ethanol (total ∼20 mL) and then centrifugation for 5 min at 4400 rpm. The particles were stored in chloroform.

3.2.6 Computational Methods

The computational methods used in this study were adapted from the work of Guo et al.[93] in which the bond dissociation energies (BDEs) of various dialkyl disulfides and diselenides were calculated. The BDEs in this study were calculated using Gaussian at the DFT level of theory and the Boese-Martin Kinetics (BMK) functional. Molecular geometries were optimized using the 6-31G(d) basis set followed by single-point energy calculations using the 6-311G(d,p) basis set.

3.3 Results and Discussion

The general procedure used here was adapted from Bi et al. in which FeS_2 nanoparticles were synthesized via a colloidal hot injection method.[28] In short, $FeCl_2$ is heated in the presence of oleylamine at 170 °C to form an iron(II)−oleylamine complex, to which a sulfur precursor (such as a solution of elemental sulfur[28]) is injected and allowed to react at 220 °C for 2 h (Scheme 3.1). The conditions were maintained between each experiment with the exception of the sulfur precursor used, which here were dialkyl disulfides (R-SS-R), thioethers (R-S-R), and thiols (R-SH), where R = Allyl, benzyl (Bz), tert-butyl (tBu), or phenyl (Ph) substituent groups.

Figure 3.1 summarizes the resulting Fe_xS_y nanoparticles obtained by varying the organosulfur precursor used, as characterized by TEM and powder XRD. FeS_2 cubic nanoparticles resulted from using Allyl-SS-Allyl as the sulfur precursor (Figure 3.1a, pyrrhotite impurity indicated by asterisks). Phase-pure FeS_2 (no detectable impurities via XRD) was obtained 30 min after Allyl-SS-Allyl injection, whereas a 2 h reaction time resulted in formation of trace pyrrhotite impurities (see the Appendix A for discussion). Phase pure Fe_3S_4 resulted from Bz-SS-Bz, Allyl-SH, and Bz-SH (Figure 3.1b, e, and f, respectively). The Fe_3S_4 products had irregular sheet-like morphologies typically on the order of >100 nm. Pyrrhotite nanoparticles with hexagonal morphologies and varied sizes were formed by the remainder of precursors used (Figure 2.1c, d,

Scheme 3-1

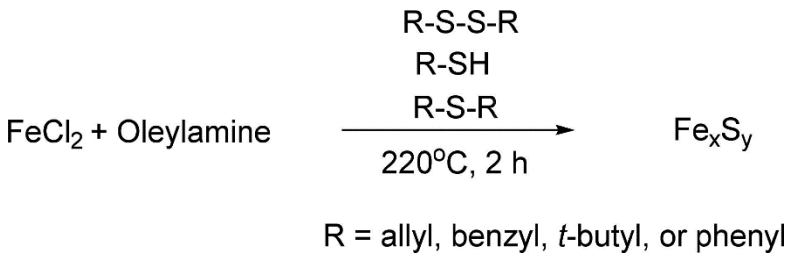

g, h, i, j, and k (with magnetite impurity peak indicated by asterisk)), with the exception of Ph-S-Ph which formed magnetite Fe_3O_4, indicative of no reaction with the sulfur precursor (Figure 3.1l).

Precursor reactivity is defined in this study as the ability of the organosulfur molecule to release an active S species capable of nucleating with the Fe^{2+} precursor to form iron sulfide nanoparticles. Qualitatively, the differences in reactivity are attributed to the pendant alkyl group attached to the S center, as well as the oxidation state of S, where the R-S-S-R feature more oxidized S_2^{2-} units relative to the S^{2-} containing R-SH and R-S-R precursors. It was observed that allyl and benzyl substituted disulfides and thiols favored the sulfur-rich pyrite and greigite phases, while tert-butyl and phenyl substituted molecules usually resulted in sulfur-poor pyrrhotite phases. In order to correlate the dependence of sulfur content in the resultant iron sulfide phase with the reactivity of the organosulfur precursor, computational evidence was explored.

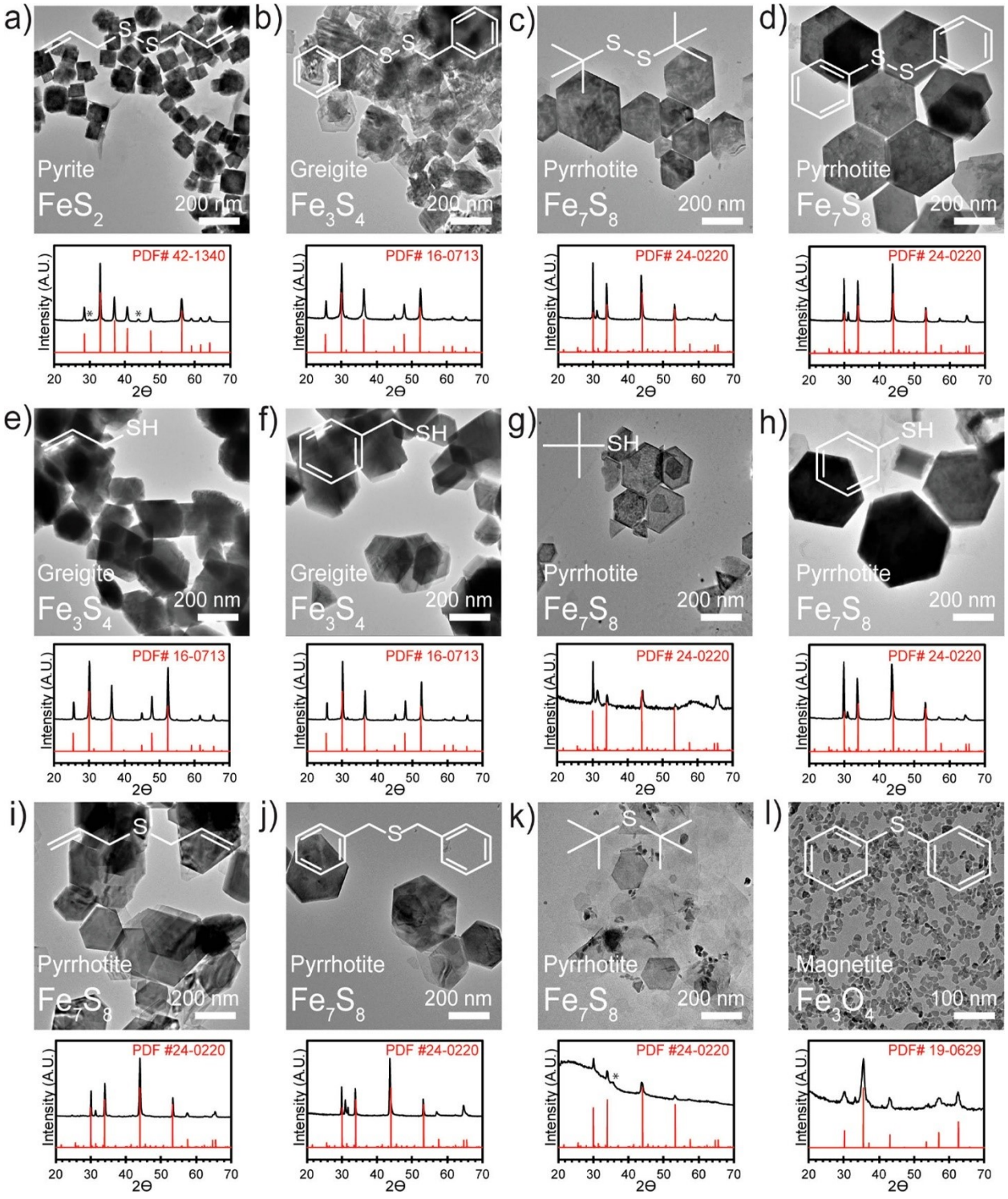

Figure 3.1: Representative TEM images and XRD patterns for products prepared with sulfur precursors of a) Allyl-SS-Allyl (*noted peaks from pyrrhotite impurity), b) Bz-SS-Bz, c) t-Bu-SS-t-Bu, d) Ph-SS-Ph, e) Allyl-SH, f) Bz-SH, g) t-Bu-SH, h) Ph-SH, (i) Allyl-S-Allyl, j) Bz-S-Bz, k) t-Bu-St-Bu (* peak is from magnetite impurity phase), and l) Ph-S-Ph.

.

3.3.1 Computational Evidence Correlating Bond Dissociation Energy to Precursor Reactivity

The determining factor of reactivity for the organosulfur precursors used is likely the C−S bond strength, since that bond must break in order to form an iron sulfide species (the S−S bond strength is additionally considered later for R-S-S-R precursors). The bond dissociation energy (BDE) was calculated using density functional theory (DFT) for each of the organosulfur precursors. Some of these bond strengths have been previously computed and reported by Guo et al., in which the low computational-cost Boese-Martin Kinetics (BMK) functional was used.[93] The calculations are repeated here and further expanded to include our full range of reagents. The calculations for C−S BDE are included in Table A1 for all R-S-S-R, R-SH, and R-S-R precursors, arranged based on the pendant alkyl group. The C−S bond strengths varied from 47.03 kcal/mol for Allyl-SS-Allyl to 77.17 kcal/mol for Ph-SH.

Several trends in C−S bond strength were observed. For each alkyl substituent class, the R-S-S-R molecule had the lowest C−S BDE, followed by R-SH and then R-S-R. This change in the S substitution class, keeping the pendant alkyl group constant, allowed for a change in C−S bond strength of 10−26 kcal/mol. Additionally, the change in pendant alkyl group provided about half the influence of the change in sulfur substitution class, providing a change in C−S bond strength of 5−12 kcal/mol. There was a consistent increase in C−S bond strength from Allyl < Bz < t-Bu < Ph substituents among the thioethers, thiols, and disulfides.

Ranges of C−S bond strength of the organosulfur precursor correlated to the iron sulfide phase produced (Figure 3.2). In general, the organosulfur precursors with the lowest C−S bond strengths favor more sulfur-rich phases. Only Allyl-SS-Allyl produced pyrite FeS_2, the most

sulfur-rich iron sulfide, and has the smallest C−S BDE, less than 50 kcal/mol. Greigite Fe_3S_4 was produced using Bz-SS-Bz, Allyl-SH, and Bz-SH which all have calculated C−S BDEs in the range between 50 and 55 kcal/mol. The rest of the precursors with calculated C−S BDEs > 55 kcal/mol produced pyrrhotite-type iron sulfides with the exception of Ph-S-Ph, which produced iron oxide particles, indicating no reaction of the sulfur precursor (Figure 3.2).

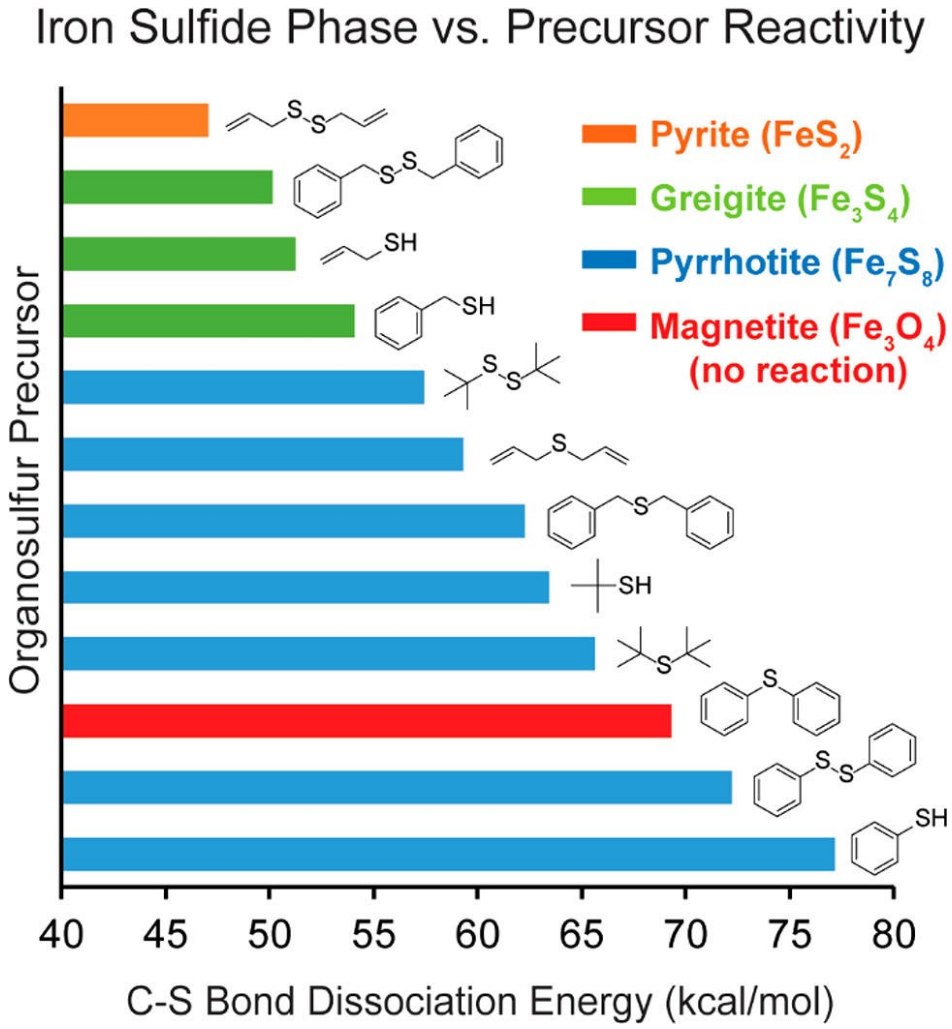

Figure 3.2: Summary of the correlation between the iron sulfide crystalline phase obtained and the precursor reactivity in terms of C−S bond dissociation energy, where more reactive organosulfur precursors have weaker C−S bonds. Organosulfur precursors that resulted in pyrite, greigite, and pyrrhotite formation are indicated by orange, green, and blue bars, respectively. The use of Ph-S-Ph resulted in the formation of magnetite (Fe_3O_4) which is indicative of no reaction with the sulfur precursor (red bar).

An additional factor must be considered in determining the reactivity of R-S-S-R precursors, which is the S−S bond strength. In Table S1 the S−S BDE was calculated for Allyl-SS-Allyl, Bz-SS-Bz, t-Bu-SS-t-Bu, and Ph-SS-Ph. The S−S BDE remains relatively constant among the R-S-S-R molecules (~61−63 kcal/mol) with the exception of Ph-SS-Ph (45 kcal/mol), whose Ph-S• radical is resonance stabilized leading to easier homolytic cleavage of the S−S bond. Since the C−S bond strength correlates well with synthetic products, it is reasonable to conclude that the C−S bond is the dominant factor in reactivity.

The possibility was also considered that the precursors universally decomposed to yield H_2S as the active sulfur source and that reaction rate and S availability were the determining factors in the phase selective synthesis. Phase control could theoretically be achieved by only modifying the reaction temperature if the mechanism was based solely on S availability. Higher reaction temperatures would result in greater S availability in solution leading to more sulfur-rich phases, while lower reaction temperatures would produce sulfur-poor phases due to a lower S availability in solution for a given organosulfur reagent. The reaction

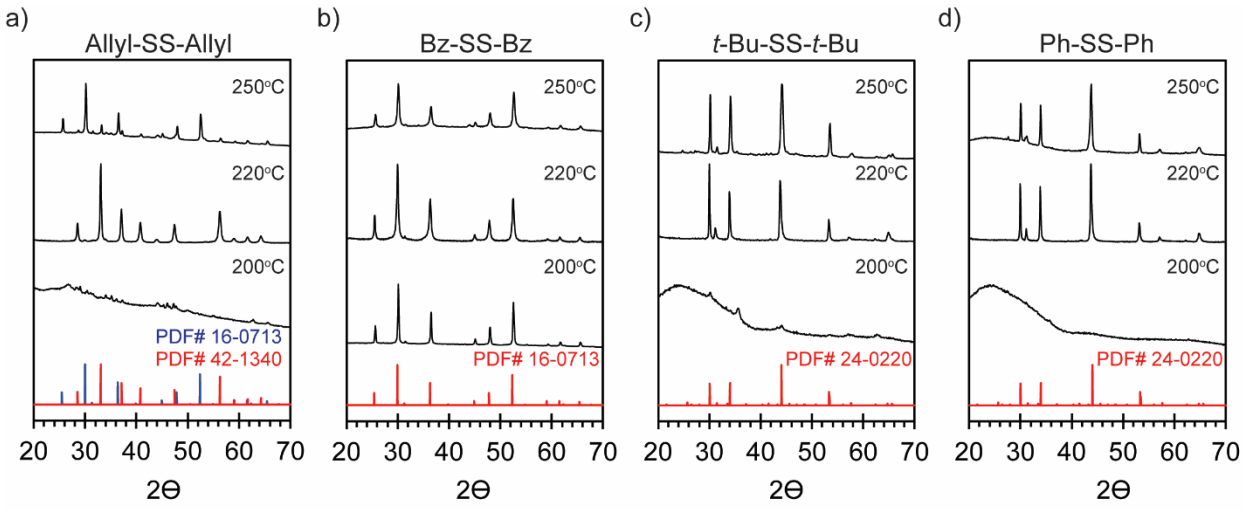

Figure 3.3: XRD study of products obtained at reaction temperatures of 200°C, 220°C and 250°C using a) Allyl-SS-Allyl, b) Bz-SS-Bz, c) *t*-Bu-SS-*t*-Bu, and d) Ph-SS-Ph.

temperatures of 250°C, and 200°C were used in this study and the products were compared to the respective products of the original 220°C reaction (Figure 3.3). For Allyl-SS-Allyl (Figure 3.3a), Fe_3S_4 (greigite, PDF# 16-0713) was the dominant phase with pyrite and pyrrhotite minor phases at 250°C. Pyrite (FeS_2, PDF# 42-1340) is the primary product with trace pyrrhotite impurities at 220°C, and at 200°C very little crystalline product is evident, where trace peaks correspond mostly to various iron oxides, indicative of no reaction of the organosulfur precursor. The hypothesis was that at the elevated temperature of 250°C sufficient thermal energy is present to cleave the S-S bonds, which were identified as the key to direct pyrite nucleation at 220°C with Allyl-SS-Allyl. For reactions using Bz-SS-Bz (Figure 3.3b), both raising or lowering the reaction temperature had little effect on the phase obtained as greigite (Fe_3S_4; PDF# 16-0713) was the major phase obtained in each case (phase pure for 200°C and 220°C, trace pyrrhotite impurity at 250°C). For both *t*-Bu-SS-*t*-Bu and Ph-SS-Ph (Figure 3.3c, d respectively) reactions performed at 250°C also had little effect with the same pyrrhotite phase (Fe_7S_8, PDF# 24-0220) resulting in both cases. However, at 200°C both *t*-Bu-SS-*t*-Bu and Ph-SS-Ph failed to react as only trace peaks belonging to magnetite Fe_3O_4 are evident. In summary, increasing the reaction temperature had a minimal effect on the crystalline product obtained, with the exception of Allyl-SS-Allyl, while decreasing the reaction temperature resulted in no reaction of the sulfur precursors, with the exception of Bz-SS-Bz. Phase control therefore appears to be based on factors other than the rate of formation of an active sulfur species.

Calculated BDE assumes a homolytic cleavage of the C−S bonds to give free radicals, which is likely not the case as S_2^{2-} and S^{2-} are in the product crystals. However, the reactivity trends for strength should be similar for homolytic and heterolytic cleavage. Both carbocations

and free radicals are stabilized by resonance in allyl and benzyl groups. Similarly, the tertiary carbon of the tert-butyl group will support carbocations and free radicals. In contrast, phenylic carbocations and free radicals are not resonance stabilized as the empty or half-filled p orbital is perpendicular to the aromatic electrons. The weak stabilization of carbocations by phenyl groups is noted in the poor reactivity of the phenyl sulfur precursors for the formation of iron sulfides; the sulfur-poor pyrrhotite phases resulted or there was no reaction.

3.3.2 Mechanism of Pyrite Formation

One of the factors that complicates phase control in the iron sulfides is the variability in both the iron and sulfur oxidation states between phases. In particular, pyrrhotite and greigite contain S^-, whereas iron pyrite FeS_2 features persulfide S_2^{2-} units. In previous syntheses of iron pyrite by colloidal hot injection methods, pyrite formation occurs through the sulfidation of an FeS intermediate via the in situ generation of H_2S when sulfur dissolved in alkyl amines is heated.[28,82,100] If pyrite can be formed without going through an FeS intermediate, it may be a way to limit bulk defects in the form of sulfur vacancies. Such vacancies and impurity phases such as sulfur-poor greigite and pyrrhotite act as recombination centers for charge carriers and are commonly implicated in the disappointing photovoltages of FeS_2 based photovoltaic devices.[34,101,102]

Direct pyrite nucleation without proceeding through an FeS intermediate is challenging, mainly because no commonly used sulfur precursors directly release the requisite S_2^{2-} units characteristic of the pyrite structure. This is likely due to the tendency of disulfide bonds to be weaker than common organosulfur bonds, as noted by Macpherson and Stoldt.[85] However, our calculated S−S BDE compared to the C−S BDE (Table S1) for Allyl-SS-Allyl is indeed an

exception, where the S−S bond (BDE = 61.14 kcal/mol) is 14.11 kcal/mol stronger than that the C−S bond, suggesting that S_2^{2-} may be directly released from the Allyl-SS-Allyl precursor to form the persulfide units in pyrite. This calculation inspired us to explore the species formed throughout the reaction in order to gain a deeper understanding of the pyrite formation mechanism.

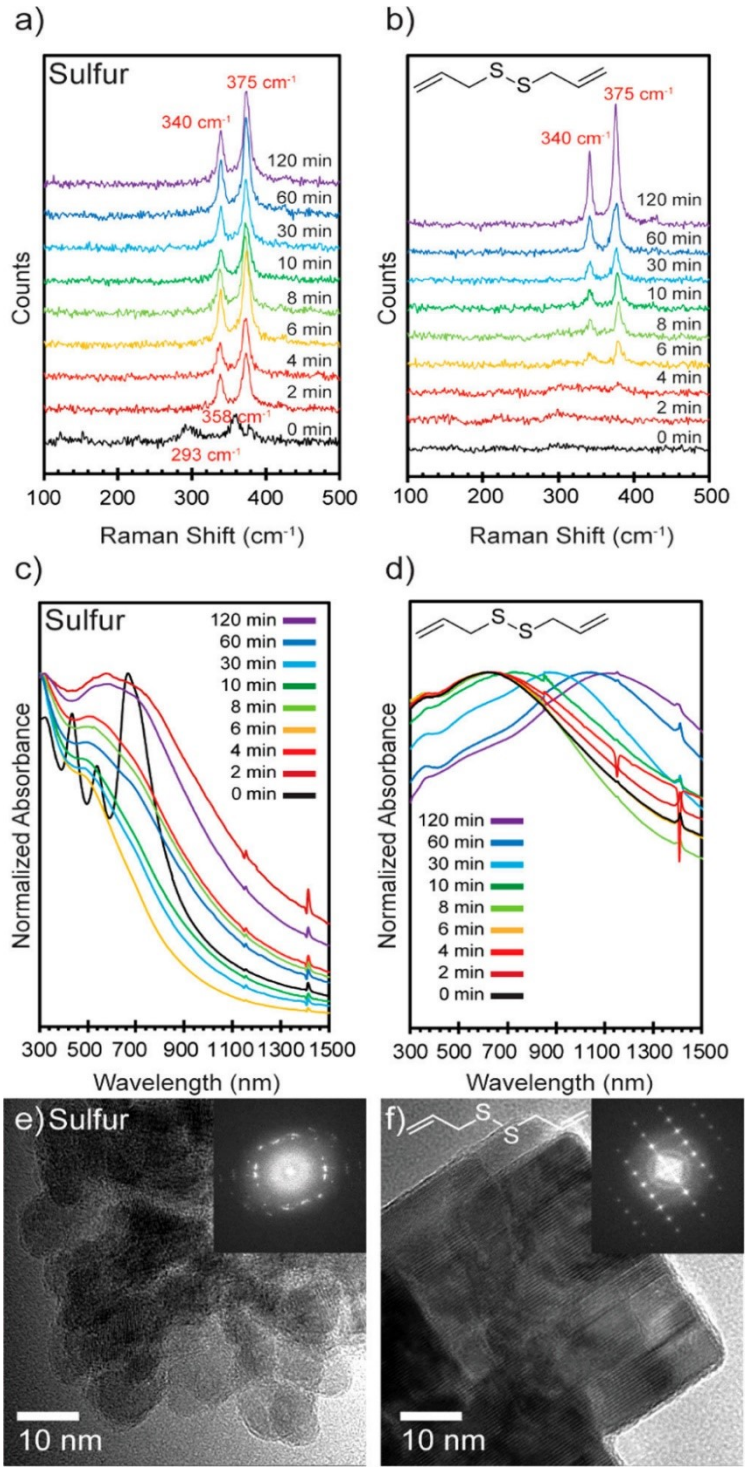

Figure 3.4 Study of pyrite FeS_2 nanoparticle syntheses using two different sulfur precursors. Aliquots were taken at 0, 2, 4, 6, 8, 10, 30, 60, and 120 min after the injection of the sulfur precursor and heating to reaction temperature. Raman spectra, UV−vis-NIR absorbance spectra (in $CHCl_3$), and TEM image of final product with corresponding Fast Fourier Transform are included for the pyrite formation reactions using elemental sulfur (a,c,e) and Allyl-SS-Allyl (b,d,f) as the sulfur source.

While phase identification via XRD is difficult during early reaction times due to low crystallinity, Raman spectroscopy can provide useful insight, as shown previously for the identification of various iron sulfide crystal phases.[28,82,103,104]

A reaction time study was performed in which aliquots were taken at 0, 2, 4, 6, 8, 10, 30, 60, and 120 min after injection of the sulfur precursor. The control experiment, in which elemental sulfur flakes were used as the precursor (Figure 3.4a) instead of an organosulfur, showed Raman signals at 293 and 358 cm^{-1} almost immediately after injection and heating to the reaction temperature (0 min). These vibrations have been previously assigned to an amorphous FeS phase.[28,82]As early as 2 min into the reaction, the amorphous FeS vibrations converted to characteristic pyrite vibrations at 340 and 375 cm^{-1} (corresponding to in-phase stretching of S−S bonds (A_g) and an S−S libration mode (E_g), respectively)[105] which grew in strength until completion of the reaction at 120 min. When Allyl-SS-Allyl was used as the sulfur precursor (Figure 3.4b), no peaks distinguishable from noise were observed for the first 6 min of the reaction. After 6 min pyrite vibrations began to appear, which proceeded to grow in intensity over time with no other visible peaks. The hypothesis is that pyrite is synthesized from the reaction mixture without the formation of an FeS intermediate, which is only possible if the S_2^{2-} units are produced directly from the sulfur precursor.

The two reaction mechanisms that resulted in pyrite formation were further analyzed by UV−vis-NIR absorption spectroscopy. A distinct absorption profile is evident immediately after the injection of elemental sulfur (Figure 3.4c, 0 min), where strong excitonic features are observed. This profile closely resembles intermediates of other colloidal pyrite syntheses that use elemental sulfur as the sulfur precursor at early stages.[83,106,107] The excitonic features were not observed at any other time point during the reaction using elemental sulfur and were completely absent when

Allyl-SS-Allyl was used as the sulfur source. The absorption spectra of the aliquots of the reaction using Allyl-SS-Allyl featured broad band absorption profiles in which the maximum appeared to redshift as the reaction progressed (Figure 3.4d). Differences in the absorption profile between particles synthesized using elemental sulfur and Allyl-SS-Allyl can be ascribed to the differing morphologies of their corresponding FeS_2 particles. For the reaction using elemental sulfur as the sulfur source, the resultant FeS_2 had a dendritic morphology, where aggregates of smaller particles were observed (Figure 3.4e). For the reaction using Allyl-SS-Allyl as the sulfur source, larger cubic particles evolved from aggregates of smaller particles (Figure 3.4f), similar to a previously described mechanism of pyrite nanocube formation via coalescence and recrystallization,[83] and the absorption features are partially occluded by scattering.

While our evidence suggests that diallyl disulfide may release S_2^{2-}, the comparison of S−S bond strength vs C−S bond strength is an unsatisfactory metric to predict the formation of pyrite over the other phases. In addition to Allyl-SS-Allyl, both Bz-SS-Bz and *t*-Bu-SS-*t*-Bu disulfide had stronger calculated S− S BDEs than C−S bonds by 11.75 and 5.67 kcal/mol, respectively (Table A1). Pyrite would also be expected from these two precursors using this metric alone, but greigite and pyrrhotite resulted instead. The hypothesis that relative C−S and S−S bond strength is the root of the phase selection needs further refinement.

3.3.3 Role of Alkylamine in Pyrite Formation with Allyl-SS-Allyl

The presence of an alkylamine is integral to the phase selective synthesis of pyrite from Allyl-SS-Allyl. When the concentration of oleylamine (OAm) was decreased by dilution with

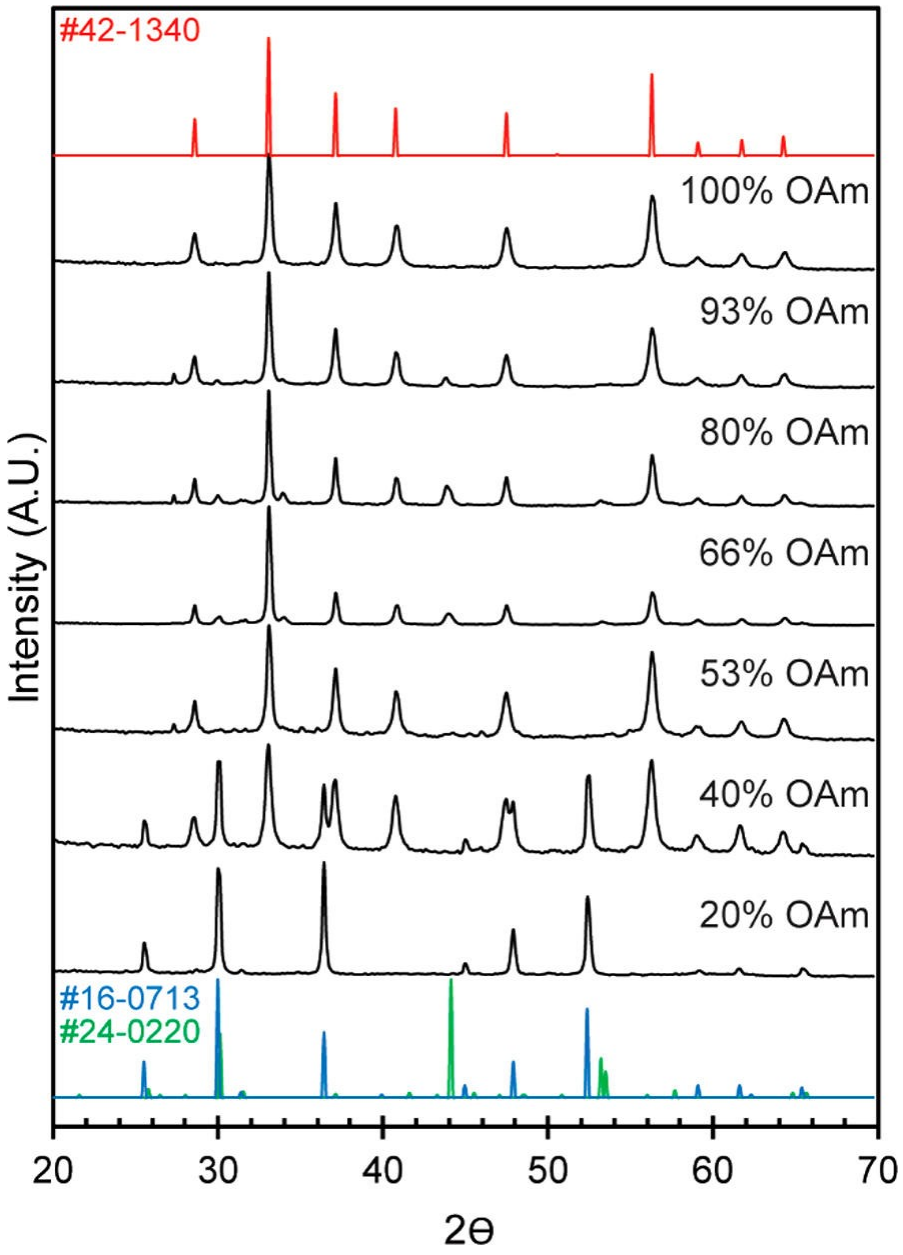

Figure 3.5 XRD study of the iron sulfide product phase obtained using Allyl-SS-Allyl sulfur precursor with decreasing oleylamine (OAm) volume % using octadecene as a cosolvent and constant overall solvent volume between samples. Pyrite #42-1340, greigite #16-0713, and pyrrhotite #24-0220 reference patterns are included.

octadecene (ODE), XRD of the products showed a change in crystal phase (Figure 3.5). When only 20% OAm was used, phase-pure greigite was the crystalline product. As the OAm volume percentage was increased to 40%, a nearly even mixture of pyrite and greigite resulted. At higher

ratios of oleylamine (53%−93% OAm) pyrite was the dominant product with greigite and pyrrhotite minority phases. Nearly phase-pure pyrite resulted when the solvent was 100% OAm. (Figure 3.5). These results indicate that the active sulfur species required to generate pyrite is only produced in the reaction of the alkylamine solvent and Allyl-SS-Allyl and not in the presence of a noncoordinating solvent such as ODE. The presence of the alkylamine is also necessary for the formation of other iron sulfide phases using other organosulfur precursors (otherwise iron oxides are formed), and it is likely necessary for the iron-catalyzed decomposition of the organosulfur reagents (Figure 3.6).

The presence of an alkylamine (oleylamine) in solution was established as a key component in the formation of FeS_2 particles using Allyl-SS-Allyl as the organosulfur precursor. A series of control experiments were conducted where oleylamine (used in the original experiment) was completely replaced by octadecene (ODE) as the solvent for several of the organosulfur reagents. While the $FeCl_2$ did dissolve in ODE to give a light tan solution, the strongly colored Fe^{2+} amine complex was not observed prior to injection. Qualitatively, the reaction mixtures at the end of each reaction were notably more transparent in color when ODE was used as the solvent compared to the corresponding reactions in OAm, and considerably lower product yields were obtained in ODE reactions. Almost none of the reagents formed the same product in neat ODE compared to neat OAm (reported in Figure 3.1). Allyl-SS-Allyl and Ally-SH were the only reagents that formed an iron sulfide product (Figure 3.6 a & b respectively), where broad peaks corresponding to greigite (Fe_3S_4, PDF#16-0713) and magnetite (Fe_3O_4, PDF# 19-0629) were observed. For Allyl-S-Allyl, Bz-SS-Bz, t-Bu-SS-tBu, and Ph-SS-Ph (Figure 3.6 c-f respectively) only the iron oxides of magnetite (Fe_3O_4, PDF# 19-0629) and hematite (Fe_2O_3, PDF# 33-0664) were obtained. It was concluded that the presence of an alkylamine is necessary for the formation of the other iron sulfide

phases with the organosulfur precursors used here. In addition to forming the colored Fe^{2+} -amine complex, it is likely that the amine is necessary for the iron-catalyzed decomposition of the organosulfur reagents.

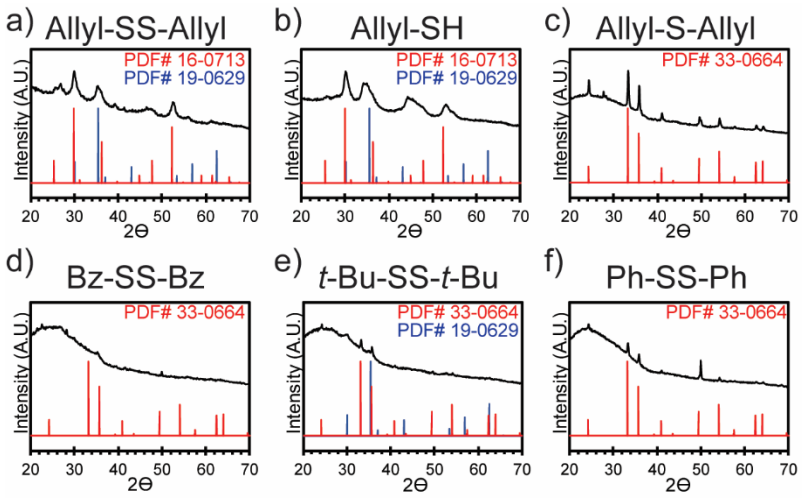

Figure 3.6: XRD patterns of resulting particles of a reaction using neat octadecene (ODE) as the solvent at 220°C for a) Allyl-SS-Allyl, b) Allyl-SH, c) Allyl-S-Allyl, d) Bz-SS-Bz, e) *t*-Bu-SS-*t*Bu, and f) Ph-SS-Ph.

Oleylamine (as well as other long-chain primary alkylamines) has a versatile role in colloidal nanocrystal syntheses as a suitable solvent, surface coordinating ligand, and reducing agent, as well as the ability to form metal−oleylamine complexes that can readily decompose to produce nanocrystals.[80,108] Additionally, alkylamine-sulfur interactions have been previously studied to determine the active species present during the syntheses of metal sulfide nanocrystals that utilize alkylamines and elemental sulfur. The alkylamine reacts with the elemental S to form H_2S and thioamides, which are the species responsible for metal sulfide formation.[100] However, since evidence for a new reaction pathway to pyrite (*vide supra*) was observed, the suspicion was

that the active sulfur species in alkylamine/Allyl-SS-Allyl mixtures differ from those previously reported for elemental alkylamine/sulfur.

3.3.4 Mechanism of Disulfide Decomposition

The assumption that C−S and S−S bond strength are the sole predictors of the phase of iron sulfide produced neglects unique chemistry that is available in the conjugated systems, on the iron metal centers, or the involvement of other constituents in the reaction, especially the alkylamine. In order to gain insight into the decomposition mechanisms and the role of the alkylamine in the reaction, the three disulfides in question (Allyl-SS-Allyl, Bz-SS-Bz, and t-Bu-SS-t-Bu) were heated in the presence of octylamine at 130 °C for 2 h, and the products were characterized by GC-MS and 1H NMR (Supporting Information). Octylamine (99% purity, bp = 175 °C) was used as a substitute for oleylamine (70% purity, bp = 350 °C) as it has a more appropriate boiling point for GC-MS analysis. A control experiment was performed which verified that an alkylamine with a shorter and fully saturated alkyl chain can be used in place of oleylamine to yield the same crystalline product (Figure A5). A reaction temperature of 130 °C was used, which is lower than the boiling points of all compounds of interest, particularly Allyl-SS-Allyl which has a boiling

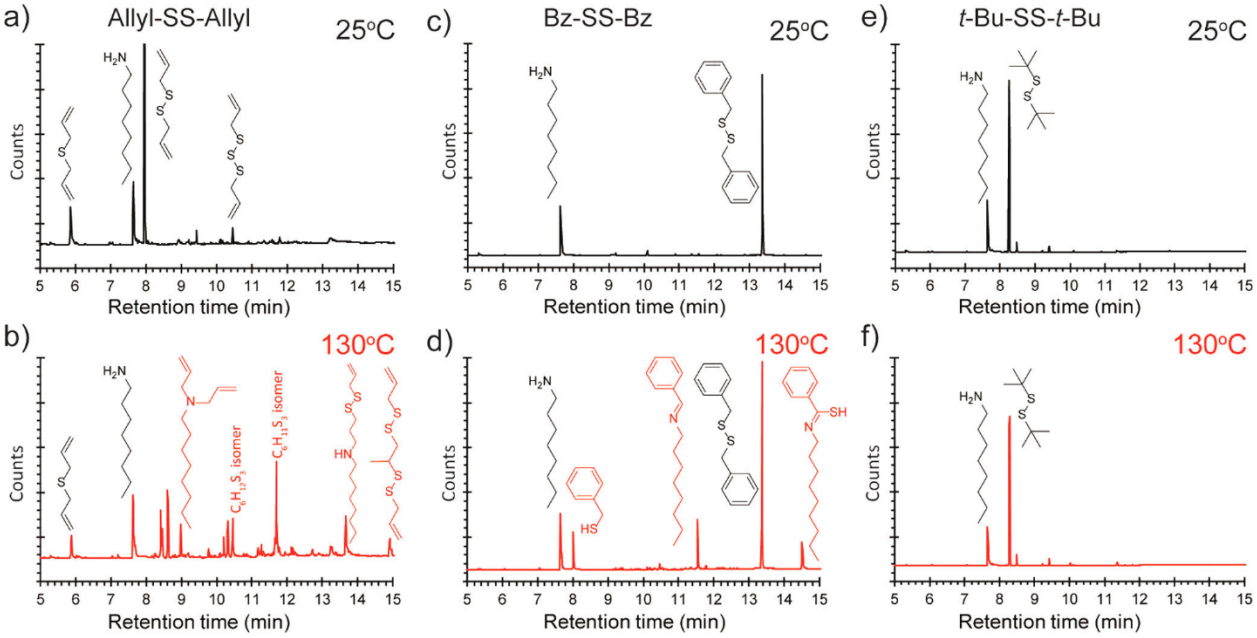

Figure 3.7: GC traces of a 1:1 amine:disulfide molar solution of Allyl-SS-Allyl in octylamine (a and b), Bz-SS-Bz in octylamine (c and d), and t-Bu-SSt-Bu in octylamine (e and f) before heating (black) and after heating (red) at 130 °C for 2 h. MS was used to assign the structures.

point of 180−195 °C. Under these conditions, it is reasonable to assume that observable decreases in GC signal for a specific compound can be attributed to reactions and chemical changes rather than compound loss via evaporation.

Figure 3.7a includes GC traces for a 1:1 molar solution of Allyl-SS-Allyl and octylamine at room temperature. The primary peaks are Allyl-SS-Allyl and octylamine as well as the expected impurities of Allyl-S-Allyl and diallyl trisulfide (Allyl-SSS-Allyl) associated with the 80% technical grade Allyl-SS-Allyl used. After the solution was heated (Figure 3.7b), octylamine remained, while Allyl-SS-Allyl had completely reacted and a number of new compounds emerged. Allyl-SS-Allyl is known to thermally decompose into a complex mixture acyclic and heterocyclic organosulfur compounds at elevated temperatures.[109,110] A control experiment was performed

wherein neat Allyl-SS-Allyl was heated for 2 h at 130 °C, resulting in a number of new observable peaks via GC. The neat Allyl-SS-Allyl solution was compared to the Allyl-SS-Allyl/octylamine solution after heating in order to determine compounds that were exclusively in the disulfide/amine solution after heating (Appendix A). Five unique compounds from the Allyl-SS-Allyl/octylamine reaction were identified and are noted in Figure 3.7b.

Allyl-SS-Allyl is known to rearrange to a thiosulfoxide isomer that is likely stabilized in the presence of the polar amine.[111] This isomer is particularly prone to nucleophilic attack at the α-CH_2 position (Scheme 3.2a).[112] The expected product of a single *N*-based substitution, *N*-allyl-octylamine was not observed (by comparison with the product from a known reaction[113]). However, *N*-allyl-octylamine is more nucleophilic than octylamine. Consequently, the product of

Scheme 2-2 Mechanistic Framework for Understanding the Facile Release of Persulfide by Diallyl Disulfide in Amines

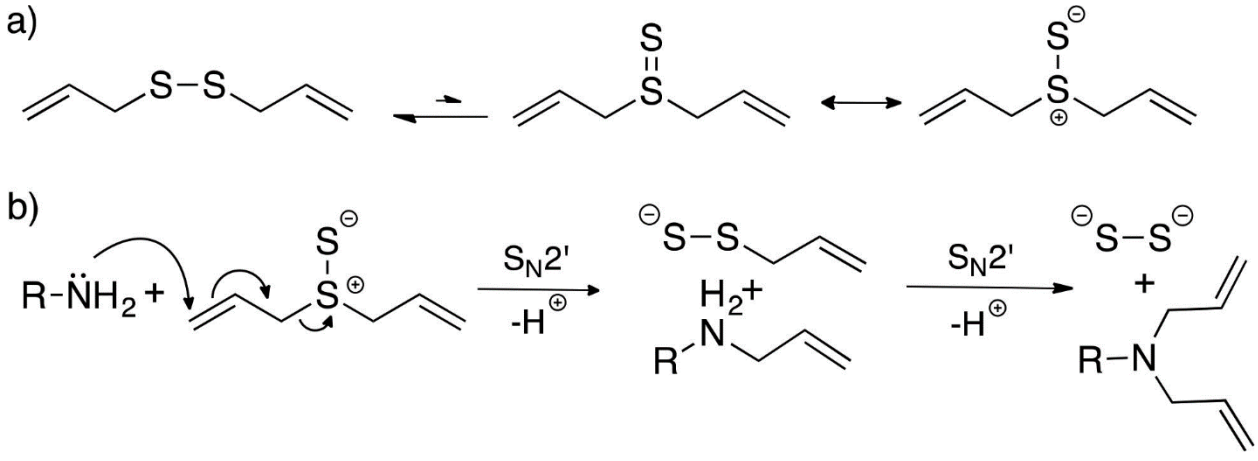

two successive *N* substitutions, di-*N*-allyl-octylamine, was consistent with the MS pattern observed for one of the products (Figure 3.5b). It is postulated that two sequential S_N2' reactions

by amine nucleophiles yield the persulfide necessary for pyrite FeS_2 formation without going through an FeS intermediate (Scheme 3.2b).

Two other products were tentatively assigned by analysis of the MS fragmentation pattern to *N*-(3-(allyldisulfanyl)propyl)-octan-1-amine and 1,3-bis(allyldisulfanyl)propane. These two products result from thiol−ene reactions by Allyl-SS-Allyl on N-allyl-octylamine and Allyl-SS-Allyl, respectively.[114] Two isomers of $C_6H_{11}S_3$ appear that are likely other thermal decomposition products of Allyl-SS-Allyl that are enhanced by the presence of the amine.

Notably, the Allyl-SSS-Allyl is completely absent in the product trace indicating it is highly reactive in these conditions. In contrast, Allyl-S-Allyl is not much changed, indicating it is far less prone to reactions with the amine.

Similar to Allyl-SS-Allyl, Bz-SS-Bz has α-CH_2 positions that are prone to nucleophilic attack due to resonance stabilization. At room temperature, octylamine and Bz-SS-Bz were observed. After heating, however, three new compounds were resolved by GC-MS (Figure 3.7c, d), which includes an expected product of a nucleophilic substitution as *N*-octyl-1-phenylmethanimine. Additionally, Bz-SH and *N*-nonylbenzimidothioic acid were evident. The presence of these compounds that only include one sulfur atom is indicative of a breaking of the disulfide bond in Bz-SS-Bz during the reaction with octylamine. This observation may explain the failure of Bz-SS-Bz to form pyrite when used as the sulfur source in the synthesis of iron sulfide nanoparticles. In contrast to the complex Allyl-SS-Allyl decomposition, these were the only new products observed after heating. Furthermore, the Bz-SS-Bz largely remained unreacted, whereas Allyl-SS-Allyl completely reacted during heating in the presence of octylamine.

Lastly, no reaction occurred for t-Bu-SS-t-Bu in octylamine as no change is evident before and after heating (Figure 3.7e, f). The α carbon in the pendant tert-butyl group is not subject to nucleophilic attack by the amine due to its bulky nature. Additionally, a *t*-Bu radical would only be stabilized via hyperconjugation rather than resonance stabilization available to Allyl-SS-Allyl and Bz-SS-Bz, so C−S homolysis is unlikely at this temperature. As a result, *t*-Bu-SS-*t*-Bu likely requires the higher reaction temperatures and/or the presence of Fe^{2+} in order to decompose to release its active sulfur species.

3.4 Conclusions

This study marks the first time that alkyl sulfides were systematically studied to achieve selective phase control of iron sulfide nanocrystals. Computational methods were used to correlate BDE with sulfur precursor reactivity; the sulfur content of the iron sulfide product obtained was a function of the strength of the C−S bond, where weaker C−S bonds yielded more sulfur-rich phases. While there is correlation with the C−S BDE, the chemistry is nuanced, in particular for Allyl-SS-Allyl, which was the only organosulfur precursor tested that yielded pyrite FeS_2. The hypothesis is that there are multiple factors at play. First, Allyl-SS-Allyl has weaker C−S bonds relative to the S−S bond, which favors the release of disulfide units needed for the pyrite structure. Second, the Allyl-SS-Allyl is subject to nucleophilic attack in S_N2' reactions, especially due to its equilibrium with a thiosulfoxide isomer. The other precursors employed do not have these reactive pathways required to generate the sulfur species needed for pyrite. Additionally, the presence of an alkylamine is essential for the phase selective synthesis of pyrite using Allyl-SS-Allyl as the sulfur precursor. When the concentration of alkylamine is decreased, the phase purity of the obtained pyrite sample suffers. Indeed, at the lowest concentrations of alkylamine, only greigite is

evident. The hypothesis is that the alkylamine is needed as a nucleophile to react with the Allyl-SS-Allyl, releasing the needed S_2^{2-} for pyrite.

This study provides insight into the phase tunability of the complicated iron sulfide system and introduces a new level of control by manipulating the sulfur precursor employed. These phase selective syntheses can be a starting point for further size and shape control of iron sulfide nanoparticles. This systematic understanding of organosulfur reactivity in the presence of alkylamines will contribute to the phase-selective synthesis of other transition metal sulfides. Additionally, the synthesis of other crystalline phases that feature S_2^{2-} structural units (such as covellite CuS as well as other pyrite type minerals CoS_2, NiS_2, etc.) may potentially benefit from using a precursor capable of directly forming persulfide units.

Chapter 4

Synthesis of FeS_2−CoS_2 Core−Frame and Core−Shell Hybrid Nanocubes[b]

4.1 Introduction

Nanoscale structuring and engineering provides a route to control and exploit the properties of materials. By achieving a level of control at the nanoscale of morphology, composition and structure, the properties of a material can be tailored for specific applications.[115] Furthermore, combining two materials can result in enhanced properties that further the utility of the hybrid material.[116] Transition metal disulfides with the pyrite crystal structure are earth abundant materials that have attracted research interest in energy applications such as photovoltaics, energy storage, and catalysis.[117,118] Despite the wide applications of pyrite family materials, the prospect of hybridizing pyrite type materials has not been thoroughly explored.

There have been only a few attempts to hybridize FeS_2 nanoparticles with another material. Recently, core−shell FeS_2−FeSe were synthesized, where the addition of the iron selenide shell improved the surface stability by eliminating intrinsic surface defects in pyrite as well as altered the net magnetic character of the nanocrystals from diamagnetic to ferrimagnetic.[119] Additionally, Tan et al. reported the synthesis of core−shell nano-FeS_2@N-doped graphene as a cathode material for use in rechargeable Li-ion batteries.[120] There have been multiple reports of doping other first-row transition metals such as Mn, Co, Ni, Cu, and Zn in the pyrite structure in order to alter the functionality.[121–126]

[b] Portions of this chapter have been previously published in Rhodes, J. M. et al., *Chem. Mater.*, **2018**, 30, 8121-8125.

Cobalt is a commonly used dopant for iron pyrite, as it is readily substituted in the crystal structure. Adjacent to iron on the periodic table and with one additional d electron, cobalt doping in pyrite nanocrystals can alter the majority carrier type from p-type to n-type.[127] Iron pyrite and cattierite (CoS_2) are isostructural and have only a 2% difference in lattice parameters (5.418 vs 5.528 Å, respectively), so in addition to doping, epitaxial growth to create a hybrid structure is likely under conditions that promote heterogeneous nucleation of the CoS_2. In this study, the synthesis of FeS_2 nanocubes hybridized with an epitaxially grown CoS_2 layer is reported, where core−frame and core−shell nanostructures were achieved.

Extensive research of bimetallic systems has led to remarkable synthetic control, where numerous morphologies are possible for the resultant hybrid nanocrystals, including the core−frame architecture.[128,129] Such structures can be formed though the phase segregation of alloy nanocrystals and the frame shape driven by minimizing strain between the two metals.[130] Galvanic displacement or reduction by an external reductant has also been used to deposit a second metal selectively at edge sites of seed crystals, often platinum group metals on Ag,[128,129,131,132] Cu,[133,134] or Ni seeds.[135] The edges are considered the most reactive, highest energy surfaces, and therefore become sites for selective deposition of metals.[136]

In addition to bimetallic systems, the core−frame structure has also been observed for metal on semiconductor combinations, in the examples Ru−Cu_2S and Rh −Cu_2S systems where these metals are reduced onto Cu_2S seeds at high temperatures by amines.[137,138] These results highlight the complexity of the growth. The reactions were notably temperature sensitive to within 5 °C at 200°C; high temperatures were needed to selectively remove ligands from the edge sites of the semiconductor seeds, but cool enough to avoid complete loss of ligands and seed sintering, and inhibit rampant metal reduction and homogeneous nucleation.[139] In compound−compound

systems, complete core−shell, rather than framed systems are often sought for protection of luminescent semiconductor quantum dots, to preserve high quantum yields. Incomplete shelling, even on one facet, is associated with poor optical properties.[140] In contrast, a framed structure will be advantageous for photocatalysis applications. The junction of materials can provide necessary charge separation after photoexcitation, and both components are exposed for respective oxidative and reductive chemistries with the solution.[141]

In our study, the hybrid structure is unique in that both the core and frame are compound materials, which is a new material combination. As well, shell overgrowth can alternatively be achieved through altering the synthetic conditions, showing synthetic control of frames vs shells only previously demonstrated in some bimetallic systems.[128,129] This core−frame hybrid nanostructure was achieved for the first time for the pyrite family of materials and provides a unique opportunity to explore the resulting structure−function relationship, notably the increase in surface area to volume ratio of the framing material.

4.2 Experimental Methods

4.2.1 General

All glassware was oven dried prior to use. Standard Schlenk line techniques were used in an inert Ar atmosphere for all reactions. A J-KEM Scientific Model 210 temperature controller was used with a heating mantle for reaction temperature control. All reagents and solvents were used as received unless otherwise noted

4.2.2 Materials

Anhydrous iron(II) chloride beads ($FeCl_2$, 99.99%), anhydrous cobalt(II) chloride ($CoCl_2$, 98%), hexadecylamine (HDA, 90%), oleylamine (OAm, 70%), and elemental sulfur were purchased from SigmaAldrich.

4.2.3 Characterization

TEM images and quantitative EDS measurements were acquired using a FEI Tecnai Osiris S/TEM operating at 200 kV with ChemiSTEM for EDS detection. Particle sizing measurements were taken in ImageJ. STEM-EDS tomography was performed on a Tecnai Osiris operating at 200kV with probe current on the order 0.5 nA. The sample was baked under high vacuum at 145 °C and then loaded onto a Fischione model 2020 tomography holder. STEM-EDS maps were collected from -65° to 65° at 2° intervals using Bruker Esprit 1.9 with acquisition times of 70 seconds, pixel dwell time of 70 ms and a pixel size of 0.6 nm. The individual maps for each element were rendered in grayscale and assembled into a tilt series. The tilt series for each element was then aligned and reconstructed using the SIRT method in Inspect 3D. The individual reconstructed volumes were then rendered and colorized using Amira 6.2. X-ray diffraction analysis was performed on a Rigaku SmartLab® X-ray diffractometer equipped with a CuKa radiation source and a D/teX Ultra 250 detector, operating at 40 kV and 44 mA. XRD samples were prepared by drop casting a concentrated solution of NPs onto a glass holder. SEM images were acquired with a Zeiss Merlin SEM working at 3.31 kV with the Inlens detector. The working distance was 5.7 mm.

4.2.4 Synthesis of FeS_2 nanocube stock solution

The FeS_2 particles used in the present study were prepared using a modified method from Macpherson and Stoldt.[85] Anhydrous $FeCl_2$ beads (2.0 mmol, 253.5 mg), elemental sulfur (12.0 mmol, 384.8 mg), and hexadecylamine (40g) were added to a 250mL three-neck round bottom flask, and reacted at 250°C for 3h under an inert argon atmosphere with magnetic stirring at 350 rpm (1 x 5/16" stir bar). The reaction solution was allowed to cool to room temperature resulting in the freezing of the solution due to the hexadecylamine. Additional $FeCl_2$ (4.0 mmol, 507.0 mg), sulfur (8.4 mmol, 269.4 mg), and oleylamine (60 mL) were added through one of the necks of the flask with argon flowing over the frozen solution. The flask was resealed and heated to 200°C for 9h, stirring at 1000 rpm. Once again, the reaction flask was allowed to cool to room temperature and additional $FeCl_2$ (4.0 mmol, 507.0 mg) and sulfur (8.4 mmol, 269.4 mg) were added to the frozen reaction solution, resealed, and reacted at 200°C for 9h under Ar. The resulting solution was allowed to cool below 80°C after which ~40mL of $CHCl_3$ was injected to prevent freezing. The solution was then centrifuged (2000 rpm, 2min) followed by decanting of the supernatant. The precipitated nanocrystals were then cleaned using two cycles of resuspension in $CHCl_3$ followed by centrifugation (2000 rpm, 5 min), and the resulting nanocrystal product stored in $CHCl_3$.

4.2.5 Synthesis of FeS_2/CoS_2 core-frame hybrid nanocubes

In order to synthesized FeS_2/CoS_2 core-frame hybrid nanocubes, a portion of the FeS_2 nanocube stock solution was vacuumed dried to remove the $CHCl_3$ solvent. Afterwards, the dried FeS_2 powder (0.5 mmol, 60 mg), anhydrous $CoCl_2$ powder (0.5 mmol, 65 mg), elemental sulfur (1.25 mmol, 40 mg), hexadecylamine (5g), and oleylamine (7.5mL) were added to a 50 mL three-neck round bottom flask with a magnetic stir bar and heated for 4h at 200°C. The reaction mixture

was then allowed to cool to below 80°C after which ~20 mL of $CHCl_3$ was added to prevent freezing. The solution was then centrifuged (2000 rpm, 2min) followed by decanting of the supernatant. The precipitated nanocrystals were then cleaned using two cycles of resuspension in $CHCl_3$ followed by centrifugation (2000 rpm, 5 min), and the resulting nanocrystal product stored in $CHCl_3$.

4.2.6 Synthesis of CoS_2

In a 25 mL 3-neck round-bottom flask, $CoCl_2$ (0.5 mmol) and 10 mL of OAm were placed under vacuum for 1 h at 60°C. The temperature was increased to 170°C under an inert N_2 atmosphere. In a separate vial, elemental sulfur was dissolved in 5 mL of OAm and placed under vacuum at room temperature for 45 min followed by backfilling with N_2 for 15 min. The S precursor/OAm solution was then injected into the reaction flask and heated to 220°C for 2 h under N_2. The reaction solution was then cooled in air to room temperature, and ~ 40 mL of chloroform was added, followed by centrifugation for 5-10 min at 8000 rpm. Particles were further purified by two cycles of suspension with chloroform followed by ethanol (total ~20 mL) then centrifugation for 5 min at 4400 rpm. The particles were stored in chloroform.

4.2.7 Electrode Fabrication

Electrode substrates were prepared by binding copper wire to FTO with conductive silver epoxy and allowed to dry. The copper wire was encased in a glass tube in order to isolate it from the electrolyte solution during measurements. The FTO with attached glass encased copper wire was then covered with epoxy (Loctite ® 1C), completely isolating the copper wire, and exposing

only a square area measuring 1cm^2 of FTO. The epoxy was allowed to dry in an oven at 120°C for at least 4hr. A suspension was made based on a method adapted from Jasion et al.,[142] where 25mg of nanocrystals, 2.5 mg of activated carbon (Vulcan XC-72R, Fuel Cell Store), 100uL of Nafion suspension (D521, 5 wt% alcohol based, Fuel Cell Store), and 500uL of $CHCl_3$ were combined. The suspension was then sonicated for 15 minutes and then 50uL were dropcast on the prepared FTO electrode described previously and allowed to dry at least 30 min before testing. A platinum electrode was also fabricated in order to compare to the nanocrystal electrodes. In short, a Pt film was electrodeposited onto a 1cm^2 area of a Au/Si wafer from a 0.01M K_2PtCl_6 solution in 0.1M HCl at for 30 min at -0.25V.

4.2.8 Electrochemical measurements

All electrochemical characterizations were performed in a three-electrode configuration and recorded using a Gamry Series G300 with PHE200 software package. Electrodes were evaluated individually submerged in a 0.5 M H_2SO_4 (aq) electrolyte with a Ag/AgCl reference electrode in saturated KCl and platinum mesh counter electrode. Linear sweep voltammetry was performed from -0.1 to -0.5 V at a scan rate of 25 mV s^{-1} and 1 mV voltage step.

4.3 Results and discussion

4.3.1 Characterization of CoS_2/FeS_2 hybrid nanoparticles

The CoS_2/FeS_2 hybrid nanoparticles were synthesized using a seeded growth method starting with FeS_2 nanocubes (Scheme 4.1). The FeS_2 seed particles were prepared using a three-

step heat up synthesis reported by Macpherson and Stold[85] in which sulfur chemical potential, alkylamine chain length, and temperature are manipulated in order to produce well faceted euhedral pyrite nanocubes. In the first step, referred to as nucleation (not nucleation in the traditional sense but rather the initial particles formed, as denoted in the original paper) the iron/sulfur precursor ratio was 1:6 and a reaction temperature of 250 °C in hexadecylamine (HDA) was used which produced spheroidal and irregularly shaped nanoparticles. In a subsequent growth step, the sulfur/iron precursor ratio was lowered to 1:2.05, temperature decreased to 200 °C, and oleylamine (OAm) added to promote the growth of the {100} facets leading to euhedral nanocubes of iron pyrite. However, these particles were mostly truncated cuboids, or had rounded edges. A second growth step was performed after the addition of $FeCl_2$ and sulfur with the 1:2.05 ratio to yield euhedral FeS_2 nanocrystals. After the FeS_2 cubes were formed and isolated, a portion was

Scheme 4-1

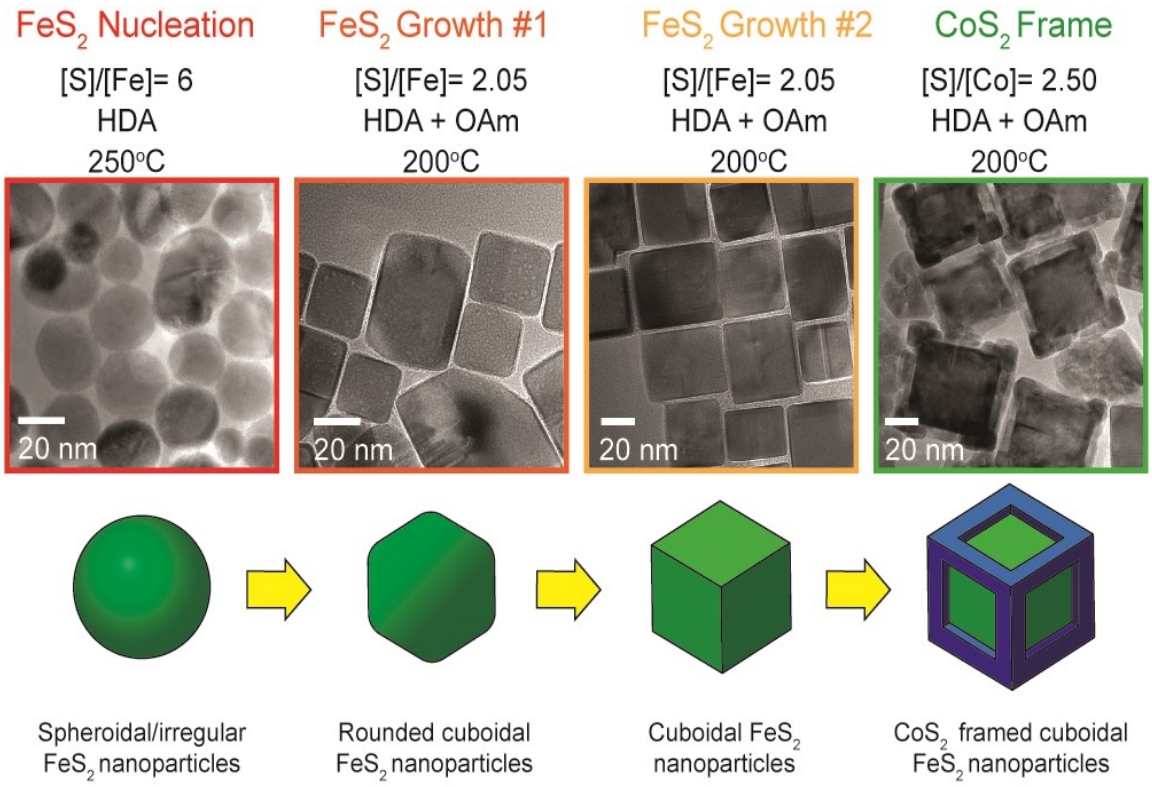

added to a new reaction flask with $CoCl_2$ and sulfur with a [S]/[Co] ratio of 1:2.5 in order to produce CoS_2/FeS_2 hybrid nanocrystals. The resultant hybrid nanocrystals maintain the cubic shape of the origin al seeds with CoS_2 grown on the outer layer of the FeS_2 cuboid crystals.

The FeS_2 nanocubes and framed hybrid nanocrystals are characterized in Figure 4.1. TEM images of the pyrite seed particles are included in Figure 4.1a, with an HR-TEM inset depicting the well isolated and euhedral morphology, as well as the lattice fringing pattern indicating the quality of the crystals. The FeS_2 nanocrystals have cuboidal shapes in some instances, so the edge length of the longest side is measured. The lattice fringing observed in the HR-TEM inset was used to determine the interplanar spacing for a nanocube, yielding a value of 2.71 Å, which is in good agreement with the {200} lattice planes of iron pyrite.[143] In Figure 4.1b, the FeS_2/CoS_2 hybrid

nanocrystals are shown, where the average edge length increased approximately 15 nm larger than the original FeS_2 seed crystals. Additionally, it can be observed from the HR-TEM inset in Figure 1b that the lattice fringing previously seen in the FeS_2 nanocube seeds now extends out into overgrown layer in the same orientation. The outer layer was determined to have an interplanar distance of 2.77 Å, which is in good agreement with the {200} lattice planes of cattierite (CoS_2). As observed in the HR-TEM inset in Figure 4.1b, the {200} planes of the outer CoS_2 layer are parallel to the {200} planes of the FeS_2 core, providing evidence of epitaxial growth. Additional FFT patterns of the lattice fringing for the core and frame material of the hybrids is included in Figure B1.

Powder XRD analysis confirmed the presence of pyrite and cattierite crystal phases. For the original nanocubes, the acquired pattern matched the JCPDS #42-1340 reference pattern for iron pyrite FeS_2 (Figure 4.1e). The acquired pattern for the hybrid nanocrystals includes the same pattern as the original nanocubes, with the addition of shoulder peaks observed at lower 2θ for each corresponding pyrite reflection. The pattern matched JCPDS#42-1340, as well as #41-1471 for cattierite CoS_2, confirming that both species are present in the hybrid nanocrystals. The observed XRD pattern acquired in the present study is distinct from other recent reports of doping cobalt into iron pyrite nanocrystals,[127,144] where the peaks shift depending on the extent of Co doping in accordance to Vegard's law. This further indicates the formation of a core/shell structure rather than an alloy.

Raman spectroscopy further confirmed the presence of independent FeS_2 and CoS_2 nanocrystalline phases. In Figure 4.1e, f, the Raman spectra for FeS_2 nanocubes and FeS_2/CoS_2 hybrid nanocrystals are included, respectively. The characteristic vibrational modes for iron pyrite are observed, where peaks at 342, 376, and 429 cm^{-1} correspond respectively to the in-phase

stretching of the S−S bonds (A_g), the S−S librational mode (E_g), and the $T_g(3)$ mode, which is both the stretching and librational motion of adjacent persulfide units.[105] For the Raman spectrum of the hybrid nanocrystals in Figure 4.1f, peaks are evident at 341 and 373 cm^{-1} indicating the

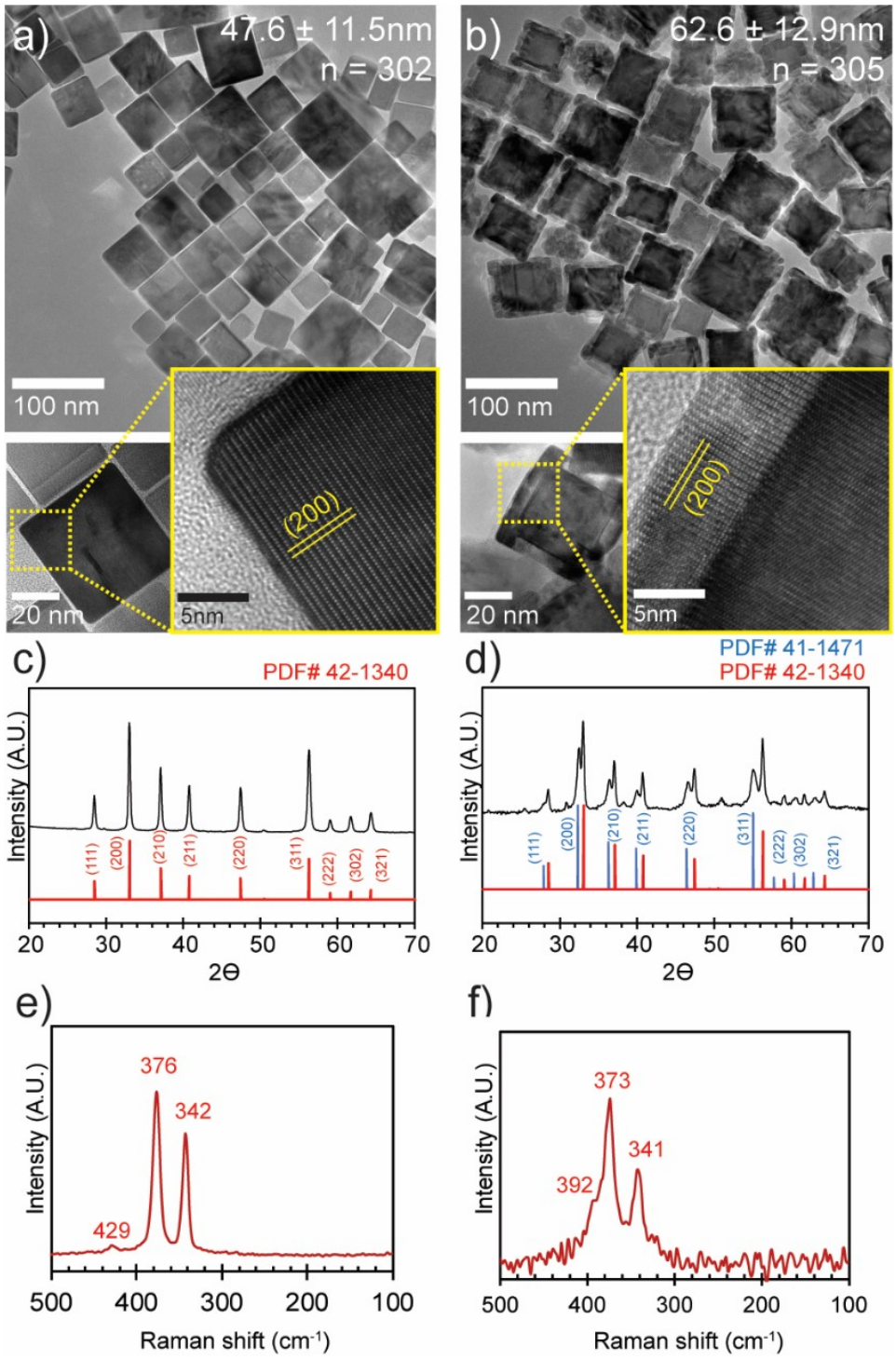

Figure 4.1: Comparison of FeS_2 nanocubes vs FeS_2 /CoS_2 hybrid nanocubes. TEM and HRTEM images for (a) FeS_2 nanocubes (edge length 47.6 ± 11.5 nm, n = 302), and (b) FeS_2 /CoS_2 hybrid nanocrystals (edge length 62.6 ± 12.9 nm, n = 305). Powder XRD pattern for FeS_2 nanocubes and FeS_2/CoS_2 hybrid nanocrystals (c and d, respectively). Raman spectroscopy for (e) FeS_2 nanocubes and (f) FeS_2/CoS_2 hybrid nanocrystals.

presence of FeS_2, but there is also a small shoulder peak at 392 cm^{-1} that closely resembles

previous reports of the A_g Raman-active mode for CoS_2.[144,145]

4.3.2 Determination of specific shelling morphology and control between core-frame and core-shell

STEM-EDS elemental mapping was performed in order to determine the atomic arrangement and morphology of the synthesized hybrid nanocrystals. For the FeS_2 cubes in Figure 4.2a, iron and sulfur are distributed throughout the nanocubes. For the hybrid nanocrystals, cobalt (blue) is localized to the outermost layer, iron (green) only in the original cube, and sulfur (red) evident throughout the entire hybrid structure, providing additional evidence that CoS_2 was grown on the outer layer of the hybrid nanocrystals (Figure 4.2b). It was determined that the hybrid particles have a caged structure as opposed to a complete shell. The first indicator of a framed structure is the contrast variation of the CoS_2 layer observed in TEM (Figure 4.2c). The four corners of the CoS_2 layer are much darker in value than the edges, which is indicative of a greater amount material in the path of the electron beam at the core and corners but less at the edges of the hybrid nanoparticle.

In addition to the TEM observations, STEM-EDS tomography was used in order to confirm and visualize in 3D our hypothesis of a core−frame structure (Figure 4.2d and full movie included in SI). The nanoparticles mounted on a TEM grid underwent a tilt sequence from −65° to +65°

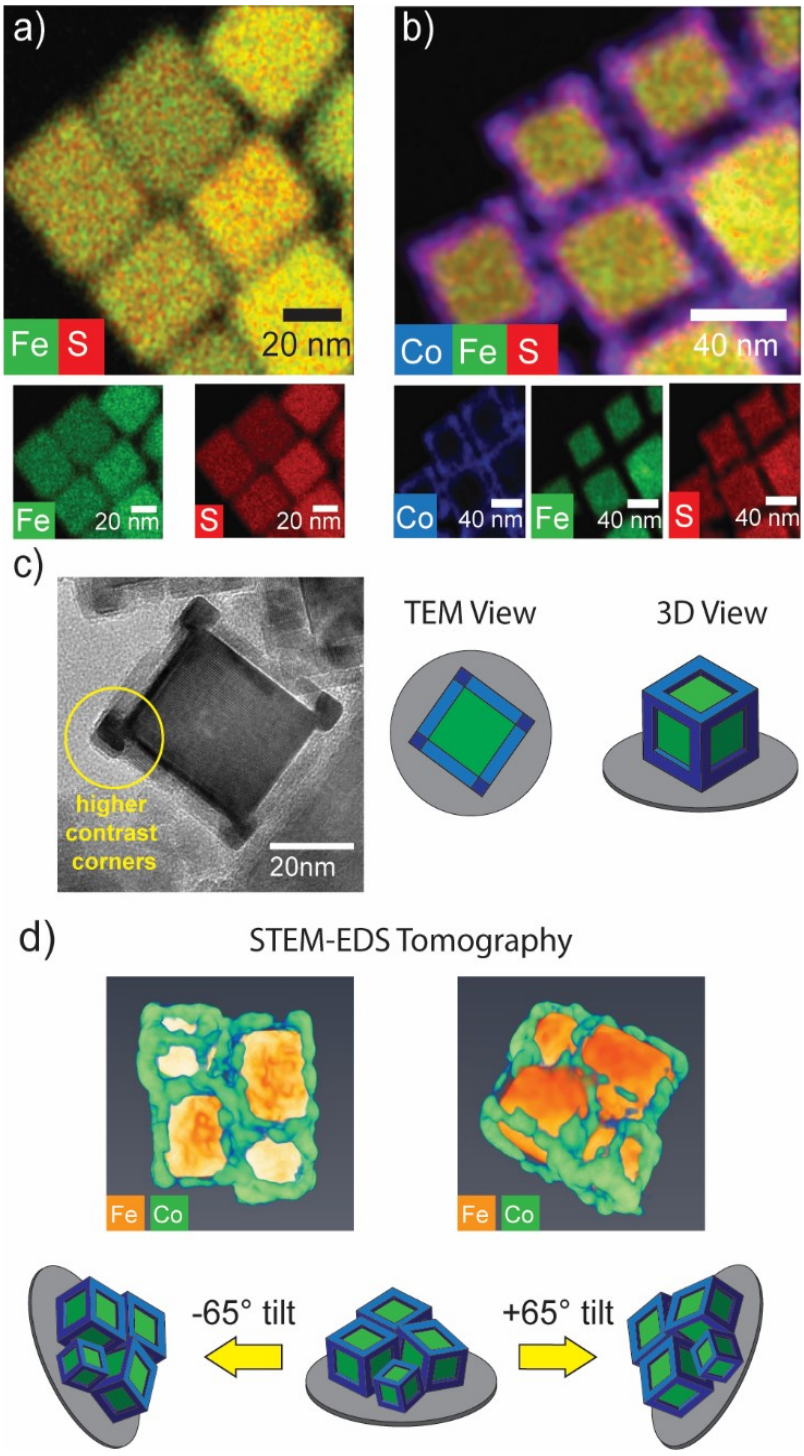

Figure 4.2 STEM-EDS mapping of nanocrystals (a and b). (c) TEM image depicting the contrast difference between FeS_2 core and CoS_2 frame, with special emphasis on the high contrast corners that provide strong evidence of a framed structure. (d) STEM-EDS tomography reconstruction single frame tomograms (full movie included in SI) depicting iron localization to core (orange) and cobalt localized to edges (green), and schematic demonstrating the tilt sequence used to acquire STEM-EDS tomography data.

(with respect to Z direction) with STEM-EDS scan acquired every 2°. The acquired data was

compiled and reconstructed in order to produce a 3-dimensional image, with the elemental mapping of the FeS_2/CoS_2 core−frame hybrid nanoparticles. Figure 4.3d includes two single frame tomograms of the 3-dimensional rendering where four adjacent nanocrystals are shown, with the spatial localization of Co and Fe specified as green and orange respectively, with iron clearly localized in the cores and cobalt framed on edges and corners. The particles demonstrated remarkable stability under the electron beam as they were resilient enough to withstand the long duration of the STEM-EDS tomography experiment.

As noted from the visual reconstruction, in some cases the nanoframes appear to be incomplete, and in other cases growth appears to extend past the edges of the prismatic nanocrystals. The epitaxial growth process appears to be initiated at the edges and corner sites, as areas of high curvature often offer a lower energy barrier for heterogeneous nucleation, and preferentially grow at these areas first. This observation prompted the exploration of the reaction conditions that influence the morphology of overgrown CoS_2 layer.

One of the parameters that affects the morphology of the outer layer of the hybrid nanostructure is the Co/S precursor ratio during the CoS_2 framing step of the reaction. When the [S]/[Co] = 2.5, the core−frame structure is obtained (Figure 4.3a), where the CoS_2 grows primarily on the edges of the nanocube. When the ratio is increased to [S]/[Co] = 4, the CoS_2 layer covers more of the surface of the underlying FeS_2 core, beyond localization to the edges (Figure 4.3b). Also, qualitatively this layer becomes rougher and appears to consist of multiple crystallites of CoS_2. When further increased to [S]/ [Co] = 6, the CoS_2 layer completely covers the surfaces of the FeS_2 nanocrystals forming a core/shell structure (Figure 4.3c). The observations of the growth of the CoS_2 layer on the FeS_2 nanocubes somewhat parallel the relationship between precursor reaction conditions and resulting morphology for the colloidal synthesis of FeS_2 colloidal

nanocrystals. As observed by Li et al.[81] previously higher iron and sulfur precursor concentrations resulted in the formation of clustered, dendritic FeS_2 nanoparticles, while lower precursor concentrations promoted growth of cubic faceted FeS_2 nanocrystals. Also, in a study by Alfonso[146]

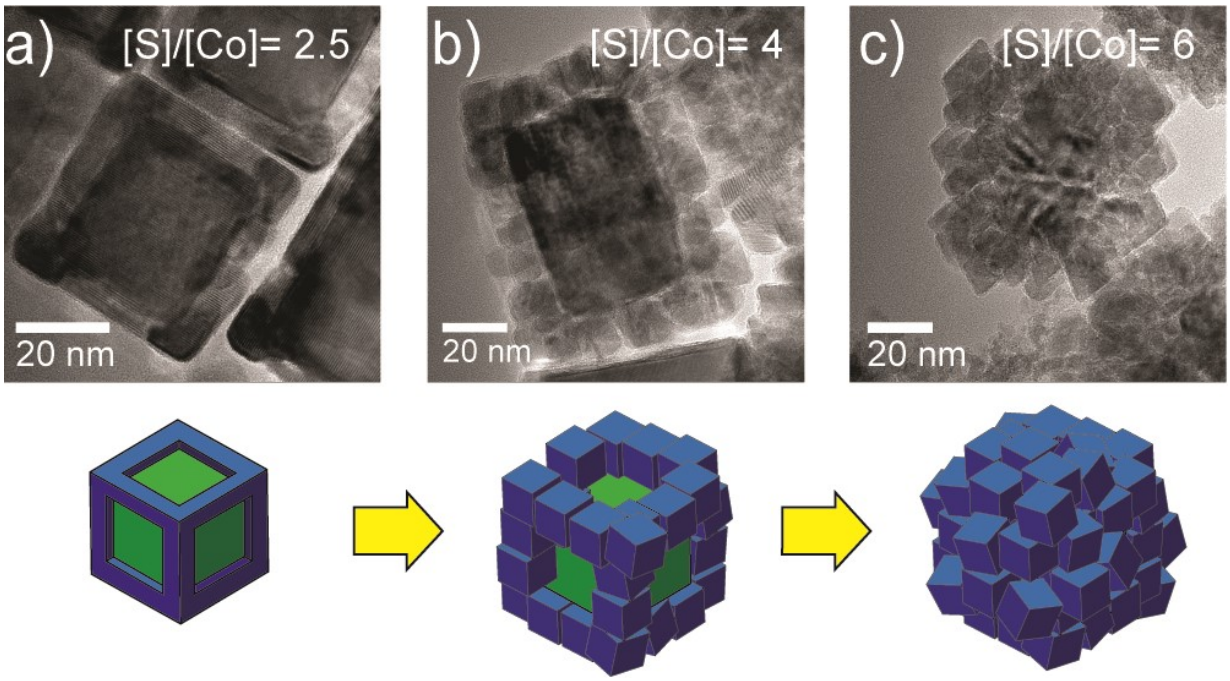

Figure 4.3 TEM images of the effect of sulfur/cobalt precursor ratio in epitaxial growth stage of reaction. (A) When [S]/[Co] = 2.5, the resultant nanostructure is core−frame. (B) When [S]/[Co] = 4, the CoS_2 outer layer becomes thicker and covers a greater area of the surface (further characterization included in Figure B2). (C) When [S]/[Co] = 6, a core/shell structure results where the entire surface of the FeS_2 core is covered with a multicrystallite CoS_2 layer (further characterization included in Figure B1).

sulfur rich/iron poor reaction conditions result in growth of other facets while sulfur poor/iron rich conditions promote growth of {100} planes. This rationale was originally used by Macpherson to produce the iron pyrite nanocubes that were used in this present study.

4.3.3 Electrochemical application

Pyrite-phase transition metal dichalcogenides have been used in electrocatalysis, demonstrating high activity toward HER[142,144,147–150] as well as oxygen reduction.[151–153] The electrocatalytic activity of transition metal pyrite-type materials has generated interest in recent years as low-cost, earth abundant alternatives to noble metal catalysts.[118] The FeS_2 nanocubes and FeS_2/CoS_2 hybrid nanocrystals synthesized here were evaluated with standard electrochemical techniques. These characterizations were performed by interfacing the thin films with an FTO electrode and measuring their voltammetric behavior in 0.5 M H_2SO_4 (aq) electrolyte. Linear sweep voltammetric polarization curves depicting the electrocatalytic current density (J) produced by the synthesized nanocrystal films plotted against potential are included in Figure 4.4. Preliminary results indicate that the hybrid core−frame nanocrystals are HER active, and in a

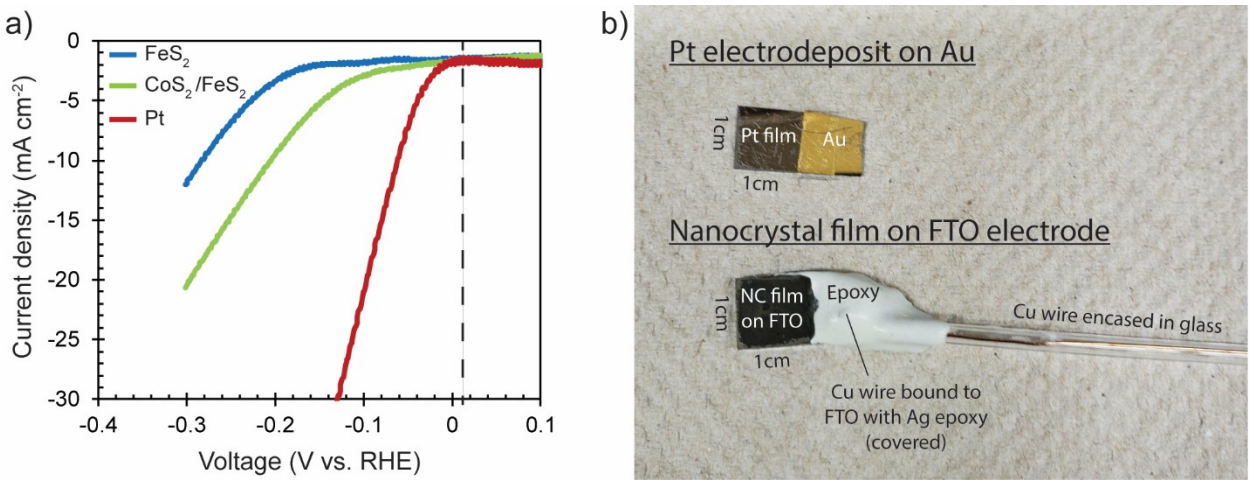

Figure 4.4: A) Electrochemical characterization of the catalytic activity of FeS_2 nanocubes (blue trace) and FeS_2/CoS_2 core-frame nanocubes (green trace), compared to Pt electrodeposited on Au coated silicon (red trace) toward HER. There is background current due to double layer capacitance. B) Fabricated electrodes for electrochemical analysis. Pt film was electrodeposited on Au. Nanocrystal films were deposited on FTO electrode with attached glass encased copper wire, sealed with epoxy.

comparison between the FeS_2 nanocubes and the FeS_2/CoS_2 core−frame nanocrystals, the hybrids outperform as indicated by the lower onset overpotential required to generate current (Figure 4.4).

The high demand of cobalt in energy storage and battery applications has caused the prices of cobalt to drastically spike.[154] Hence, designing systems that efficiently use cobalt is preferable. In catalytic applications, the interfacial surface atoms are responsible for the activity of the catalyst, and a system that maximizes surface atoms while minimizing unnecessary bulk atoms will improve the overall efficiency of the system while consuming less material to do so. In this hybrid system, CoS_2 is present primarily as edge sites while grown on a FeS_2 substrate (one of the most abundant and inexpensive metal chalcogenide materials).

4.4 Conclusion

In conclusion, the colloidal synthesis of FeS_2/CoS_2 core−frame hybrid nanocubes is reported for the first time. The core−frame interface exhibits epitaxial growth between two compounds with the pyrite crystal structure. The morphology of the outer CoS_2 layer can be tuned between core−frame and core−shell based on sulfur/cobalt precursor ratio. The core− frame hybrids also demonstrate electrocatalytic activity toward HER. The core−frame nanostructure is interesting as it may reduce the amount of CoS_2 used while increasing the active catalyst surface area. Ongoing effort is directed toward achieving the hybrid nanostructures with other pyrite type phases such as NiS_2 and RuS_2.

4.5 Attempts to shell with other pyrite-type materials

As a continuation of the work in chapter 4, other materials were considered for the shelling of iron pyrite nanocubes. The pyrite mineralogical family includes a number of other compounds in addition to FeS_2 and CoS_2. With a cubic space group of $Pa\bar{3}$ and general formula of MX_2, (where M= Au, Co, Cu, Fe, Mn, Ni, Os, Pd, Pt, Ru; and X= As, Bi, S, Sb, Se, and Te. The pyrite family of minerals consists of 18 members. The unit cell parameters of all the pyrite family materials are

Table 4-1: Pyrite crystal group. Unit cell parameter data retrieved from the Mineralogical Society of America's Handbook of Mineralogy

Mineral	Formula	Space Group	Cell parameter (Å)	% lattice mismatch to FeS_2
Pyrite	FeS_2	*Pa3*	5.417	0.00%
Cattierite	CoS_2	*Pa3*	5.52	1.87%
Fukuchilite	Cu_3FeS_8	*Pa3*	5.58	2.92%
Laurite	RuS_2	*Pa3*	5.614	3.51%
Erlichmanite	OsS_2	*Pa3*	5.62	3.61%
Vaesite	NiS_2	*Pa3*	5.668	4.43%
Dzharkenite	$FeSe_2$	*Pa3*	5.783	6.33%
Trogtalite	$CoSe_2$	*Pa3*	5.872	7.75%
Sperrylite	$PtAs_2$	*Pa3*	5.967	9.22%
Penroseite	$(Ni,Co,Cu)Se_2$	*Pa3*	5.991	9.58%
Krut'aite	$CuSe_2$	*Pa3*	6.056	10.55%
Hauerite	MnS_2	*Pa3*	6.107	11.30%
Gaotaiite	Ir_3Te_8	*Pa3*	6.413	15.53%
Geversite	$PtSb_2$	*Pa3*	6.428	15.73%
Aurostibite	$AuSb_2$	*Pa3*	6.646	18.49%
Insizwaite	$Pt(Bi,Sb)_2$	*Pa3*	6.691	19.04%

listed in Table 4.1. Based on the unit cell parameter relative to iron pyrite, and the availability of requisite precursors, three other candidates were identified as potential shelling materials for the FeS_2 cubes: Laurite (RuS_2), Vaesite (NiS_2), and Hauerite (MnS_2).

Epitaxial growth of RuS_2 on FeS_2 substrates has been reported previously by Kratzig *et. al.* as a potential photoelectrochemically active anode material for oxygen evolution in water splitting.[155] In their study, epitaxy was achieved using reactive magnetron sputtering to deposit 60 nm thick RuS_2 films on to bulk natural pyrite single crystals. To the best of our knowledge no attempts have

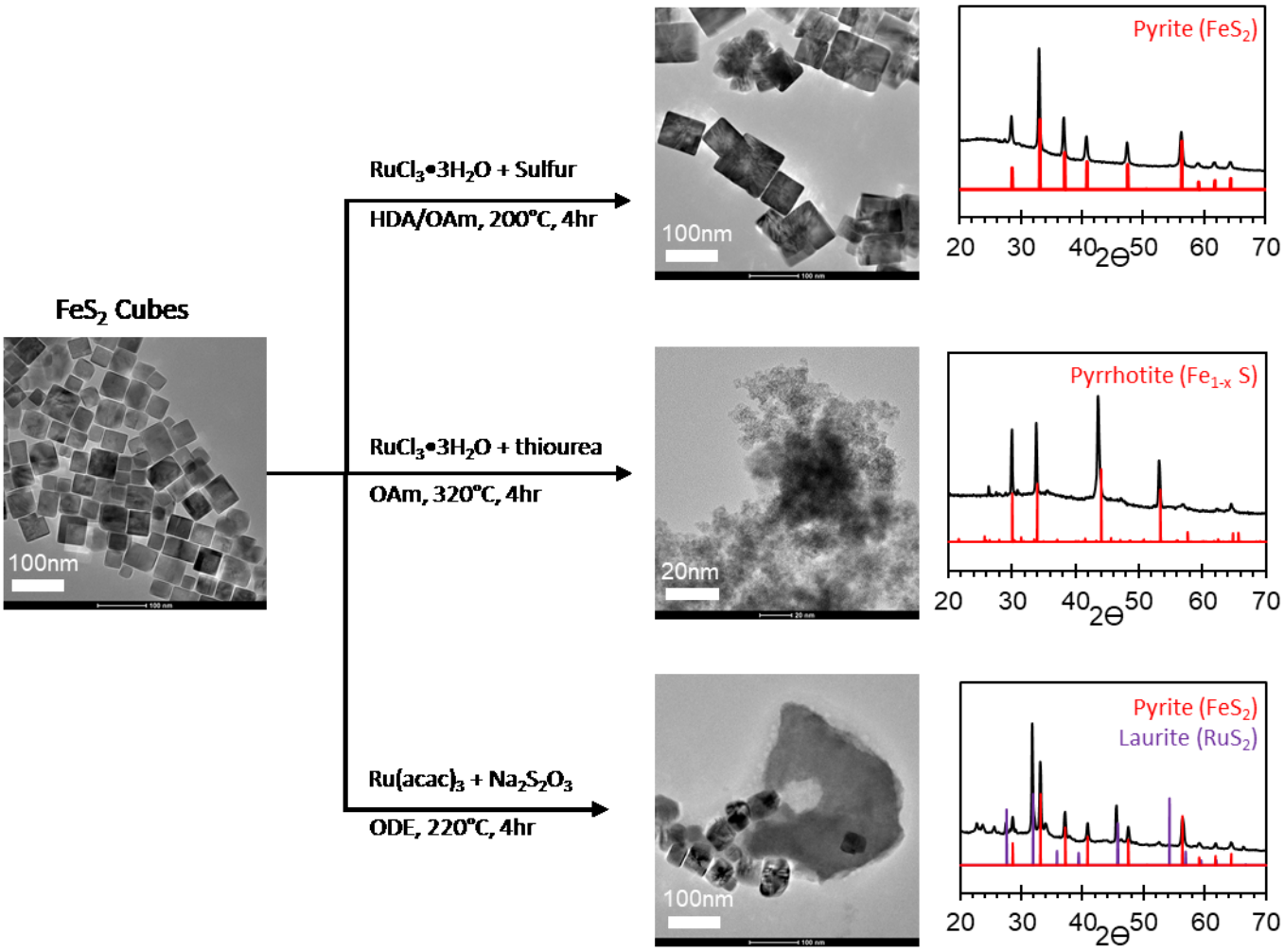

Figure 4.5 Shelling attempts with RuS_2 on FeS_2 nanocubes.

been made to synthesize RuS_2/FeS_2 nanostructures, which would be more favored for catalytic applications due to a much greater surface to volume ratio than bulk counterparts.

In the initial attempt to shell FeS_2 cubes with RuS_2, the same conditions used for the shelling of CoS_2 (Chapter 4) were used, only with the replacement of $CoCl_2$ precursor with $RuCl_3•xH_2O$. The product FeS_2 cubes showed no evidence of a ruthenium containing product (Figure 4.5). Shelling attempts at both 170°C and 220°C also proved unsuccessful using elemental sulfur as a precursor. In an attempt to find literature precedence for the colloidal synthesis of RuS_2, a footnote

was encountered where Kratzig *et al.*[155] mentioned that they "prepared RuS_2 in the form of colloidal particles using $RuCl_3$ as ruthenium and CH_4N_2S, C_2H_5NS, Na_2S, and $Na_2S_2O_3$ as sulfur precursors," however a detailed account of experimental procedures not available as unpublished results were cited. Further correspondence with the authors revealed that the colloidal reaction formed an RuS_xO_y intermediate after the reaction of $RuCl_3$ with thiourea, followed by annealing at temperatures of 400°C in the presence of H_2S. The issue encountered was the high reaction temperatures required for RuS_2 nanocrystal synthesis, where in our experiments the pyrite nanocubes visibly decomposed into pyrrhotite at 320°C. Attempts to lower the reaction temperature resulted in failure to obtain RuS_2 or any Ru nanocrystalline phase, with the exception of $Na_2S_2O_3$. The exception was when $Na_2S_2O_3$ was used. Evidence of RuS_2 appeared in the XRD, but in TEM analysis it was unclear if heterogeneous nucleation had occurred. Instead large irregularly shaped, ruthenium rich (via STEM-EDS) crystals appeared in addition the FeS_2 seed particles (Figure 4.5).

Chapter 5

Preliminary & Conceptual Work: Progress Towards Phase Control Based Precursor Decomposition Kinetics

5.1 Para Disubstituted benzyl disulfides for phase control of iron sulfides

In Chapter 3, we made the observation that phase control of iron sulfides correlated to the reactivity of various alkyl disulfides, sulfides, and thiols in terms of C-S bond strength (Figure 3.2). Of all the reagents used only allyl disulfide formed iron pyrite. Early on our working hypothesis for why allyl disulfide could form pyrite was only a function of the relative strength between the C-S and S-S bonds present. Allyl disulfide has a calculated S-S BDE that is 14.11 kcal/mol higher than its C-S BDE, the largest difference between C-S and S-S BDE for all three disulfides used with stronger S-S bonds than C-S bonds (Figure 5.1). It was speculated that allyl disulfide may possibly be able to thermally decompose and release S_2^{2-} units required for the synthesis of pyrite. Before we were aware of the unique chemistry available to the pendant allyl substituents and the role of oleylamine (see section 3.3.4), the hypothesis was that another disulfide reagent with a similar energy difference should also be able to form iron pyrite.

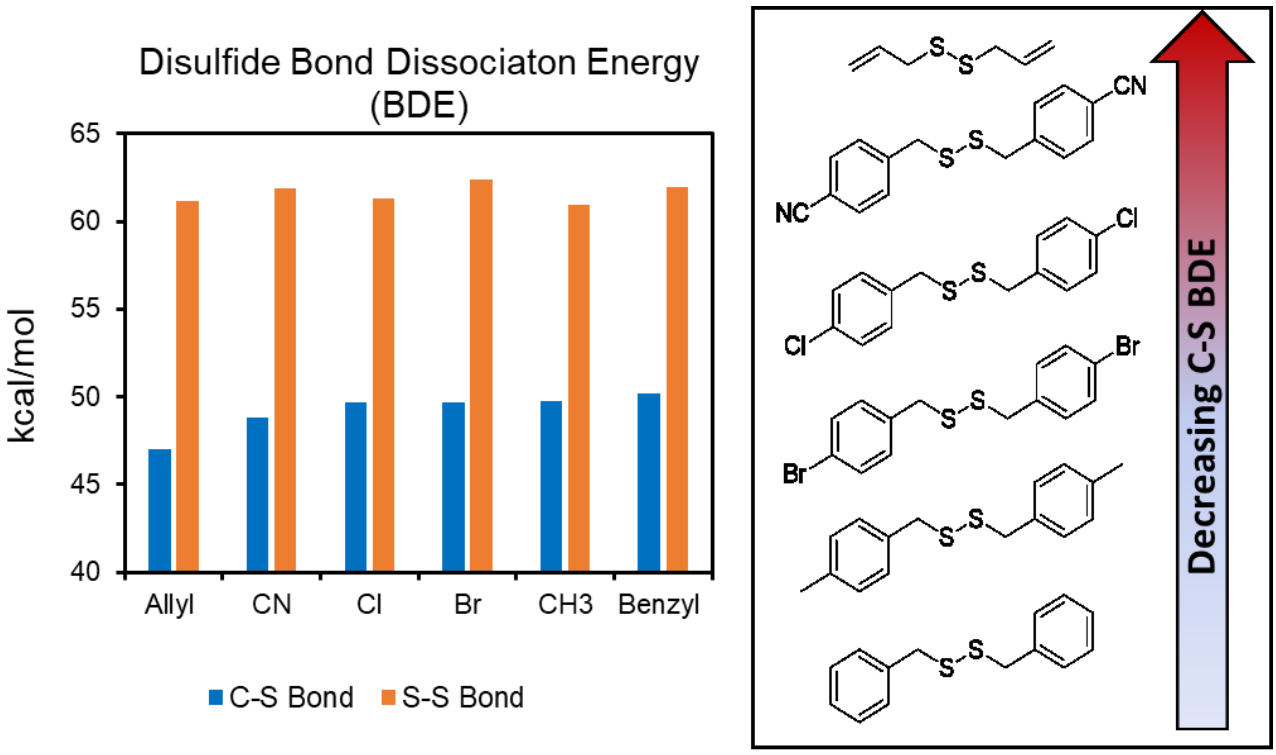

Figure 5.1: Bond dissociation energy (BDE) of allyl disulfide, benzyl disulfide, and para substituted benzyl disulfides.

Benzyl disulfide had the most similar energy difference between C-S and S-S BDE at 11.74 kcal/mol, so substituted benzyl disulfide reagents were considered as possible alternatives. Adding substituent groups on the benzene rings should modify the C-S bond strength based on the electron withdrawing or donating nature of the substituent. Electron withdrawing substituents were chosen in order to draw electron density from the C-S bond. DFT calculations were performed using the same computational methods described in section 3.2.6 in order to confirm the effect of modifying benzyl disulfide with substituent groups (Figure 5.1). The substituent groups initially considered for para-substitution on the benzyl rings of dibenzyl disulfide were methyl (CH_3-Bz-SS-Bz-CH_3) , bromo (Br-Bz-SS-Bz-Br), chloro- (Cl-Bz-SS-Bz-Cl), and cyano- (CN-Bz-SS-Bz-CN) groups, with the observed trend of slight decrease in C-S BDE with values of 49.76, 49.65, 49.72, and

48.81 kcal/mol respectively. Bz-SS-Bz substitution with the most electron withdrawing group CN resulted in the lowest C-S BDE (48.81 kcal/mol) of the series as expected, however it was not quite enough to match the value for allyl disulfide (47.04 kcal/mol). We decided anyway to experimentally test if the lower C-S BDE of CN-Bz-SS-Bz-CN was enough to synthesize pyrite.

Scheme 5-1: Synthetic scheme for CN-Bz-SS-Bz-CN, adapted from a method by Zhou et al. (ref 156)

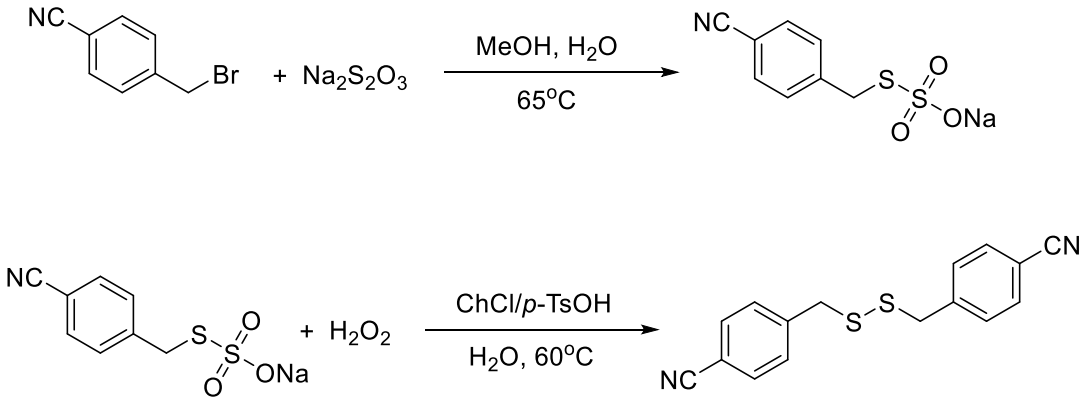

A general method to synthesize a number of disubstituted benzyl disulfides reported by Zhou[156] was adapted in order to synthesize 4,4'-(disulfanediylbis(methylene))dibenzonitrile (CN-Bz-SS-Bz-CN) in Scheme 5.1. First, commercially available 4-(bromomethyl) benzonitrile was converted into sodium S-(4-cyanobenzyl) sulfurothioate in a reaction with sodium thiosulfate in methanol and water. After the isolation of the resulting Bunte salt, the reaction of sodium S-(4-cyanobenzyl) sulfurthioate with hydrogen peroxide was catalyzed by a deep eutectic mixture consisting of choline chloride (ChCl) and *p*-toluenesulfonic acid (*p*-TsOH) to yield CN-Bz-SS-Bz-CN (Figure 5.2a). The resulting product of using CN-Bz-SS-Bz-CN in the general procedure for iron sulfide nanocrystals synthesis is included in Figure 5.2b&c. Large >100 nm hexagonal platelets were the resultant product with an XRD diffraction pattern that corresponded to pyrrhotite Fe_7S_8 (PDF# 29-0723).

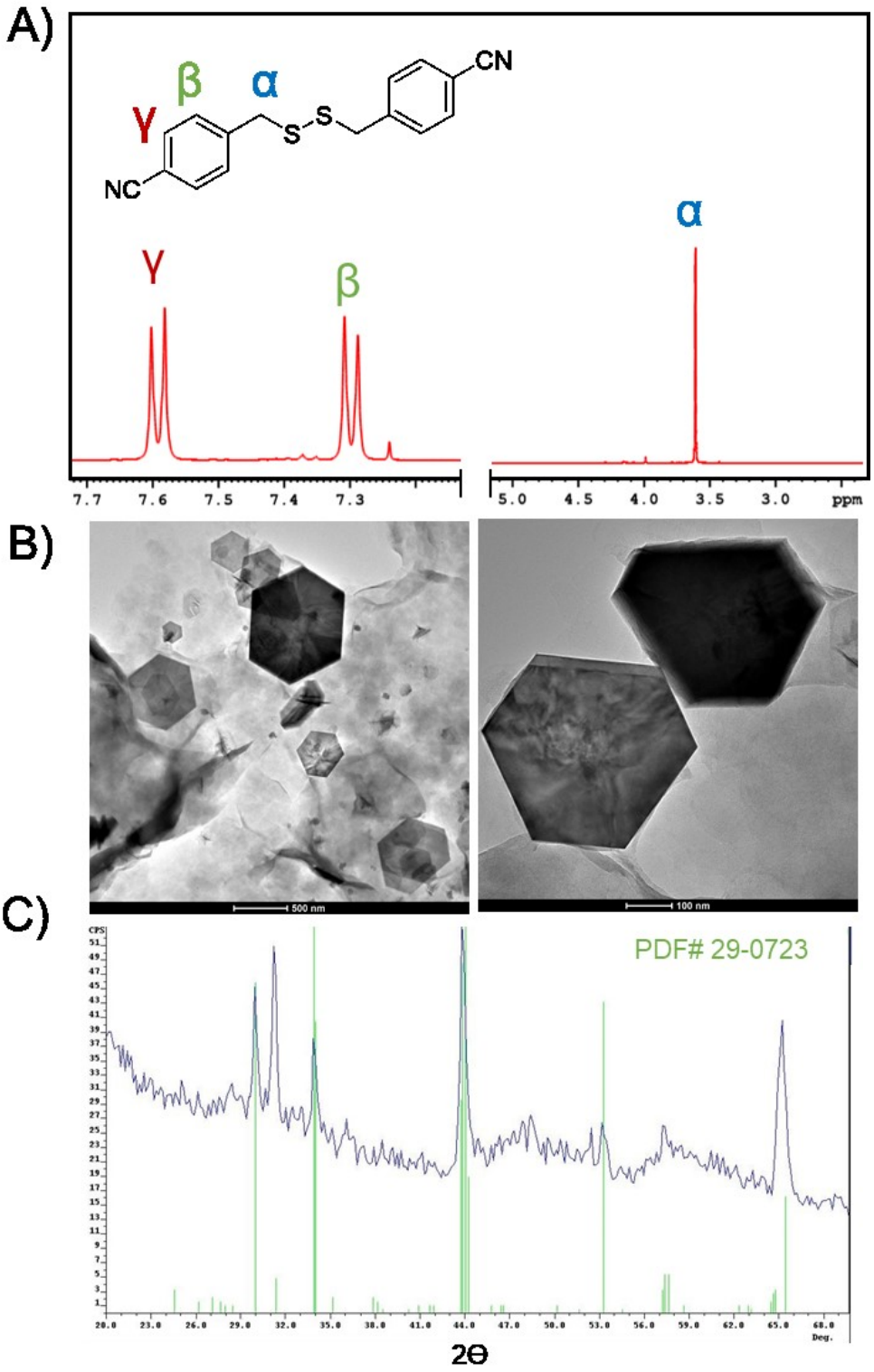

Figure 5.2. A) [1]H-NMR spectrum of CN-Bz-SS-Bz-CN. B) TEM images of resulting iron sulfide nanocrystals using CN-Bz-SS-Bz-CN as the sulfur source, and C) corresponding XRD pattern matching JCPDS # 29-0723 for pyrrhotite.

Obtaining pyrrhotite nanocrystals was an unexpected result of using CN-Bz-SS-Bz-CN as the sulfur precursor in the Fe_xS_y synthesis. As noted in chapter 3, when Bz-SS-Bz was used as the sulfur precursor, greigite Fe_3S_4 was the product. By using a substituted benzyl disulfide with a slightly lower C-S BDE, it was expected that at least greigite would form if not pyrite, if the mechanism of iron sulfide phase control was based solely on the strength of the C-S bond to release the active sulfur species. More data points would be required to make a stronger conclusion, but this project was ultimately abandoned in favor of exploring the decomposition mechanisms of dialkyl disulfides as it turned out that unique chemistry available to allyl disulfide also contributed to pyrite formation, which was described in Section 3.3.4.

Further considerations could potentially be interesting in retrospect. Firstly, using stronger electron withdrawing groups such as $-NO_2$ or $-CF_3$ could potentially lower the C-S BDE even further than the -CN groups used here. Additionally, meta ring substitution for the electron withdrawing groups would also likely have a greater effect on the C-S bond, as well as di-substitution at both meta positions of the aromatic rings, offering even more tunability. However, further investigation into the availability or ease of synthesis of such precursors would be required, as well as considerations about the potential unforeseen effects adding such groups could have on the synthesis of various iron sulfides.

5.2 Kinetic phase control with substituted thioureas

One of the main issues with the phase control of iron sulfides reported in Chapter 3 was phase control as a function of reactivity in the iron sulfide system using various substituted disulfides, thiols, and sulfides. While this study provided insight into the factors that can contribute to phase selection such as the reactivity of the sulfur precursor, other factors complicated analysis

like the unique chemistry available to allyl disulfide. The study of phase control as a function of the kinetics of precursor decomposition and subsequent release of the reactive chalcogenide species would further the understanding of nanocrystal synthesis. In order to isolate the kinetic factors, reagents must be chosen that undergo the same decomposition mechanism. Hence, selecting chalcogenide precursors that have varying reactivities but the same decomposition mechanism can provide the framework for a study in which the kinetics of precursor

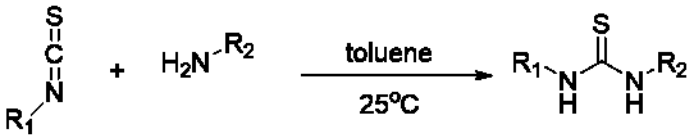

	R_1	R_2
1	3,5-$(CF_3)_2$Ph	Ph
2	Ph	Ph
3	*p*-CN-Ph	$C_{12}H_{25}$
4	Ph	$C_{12}H_{25}$
5	C_6H_{13}	$C_{12}H_{25}$

Figure 5.3: General click reaction scheme between various substituted isothiocyanates and primary amines.

decomposition can be correlated to phase selection.

N-substituted thioureas are promising sulfur releasing precursors with facile tunability. In a study by Hendricks *et. al.*,[157] a tunable library of substituted thioureas enabled a large range of precursor decomposition rates that release the active sulfur species, leading to subsequent control

PbS crystal sizes. The thiourea reagents were prepared as described by simple click reaction between commercially available substituted isothiocyanates and primary or secondary amines in toluene at room temperature (Figure 5.4).

Five N-substituted thiourea precursors were chosen to react with $FeCl_2$ in oleylamine at 220℃ to form iron sulfide nanocrystals in Figure 5.4a. When N-(3,5-bis(trifluoromethyl)phenyl)-N'-phenylthiourea was used as the sulfur precursor, large >100 nm rod-like crystals resulted, identified by XRD as predominately pyrrhotite $Fe_{1-x}S$ with a trace amount of greigite Fe_3S_4 (Figure 5.4b. Using N-(4-cyanophenyl)-N'-dodecylthiourea resulted in primarily pyrrhotite crystals as

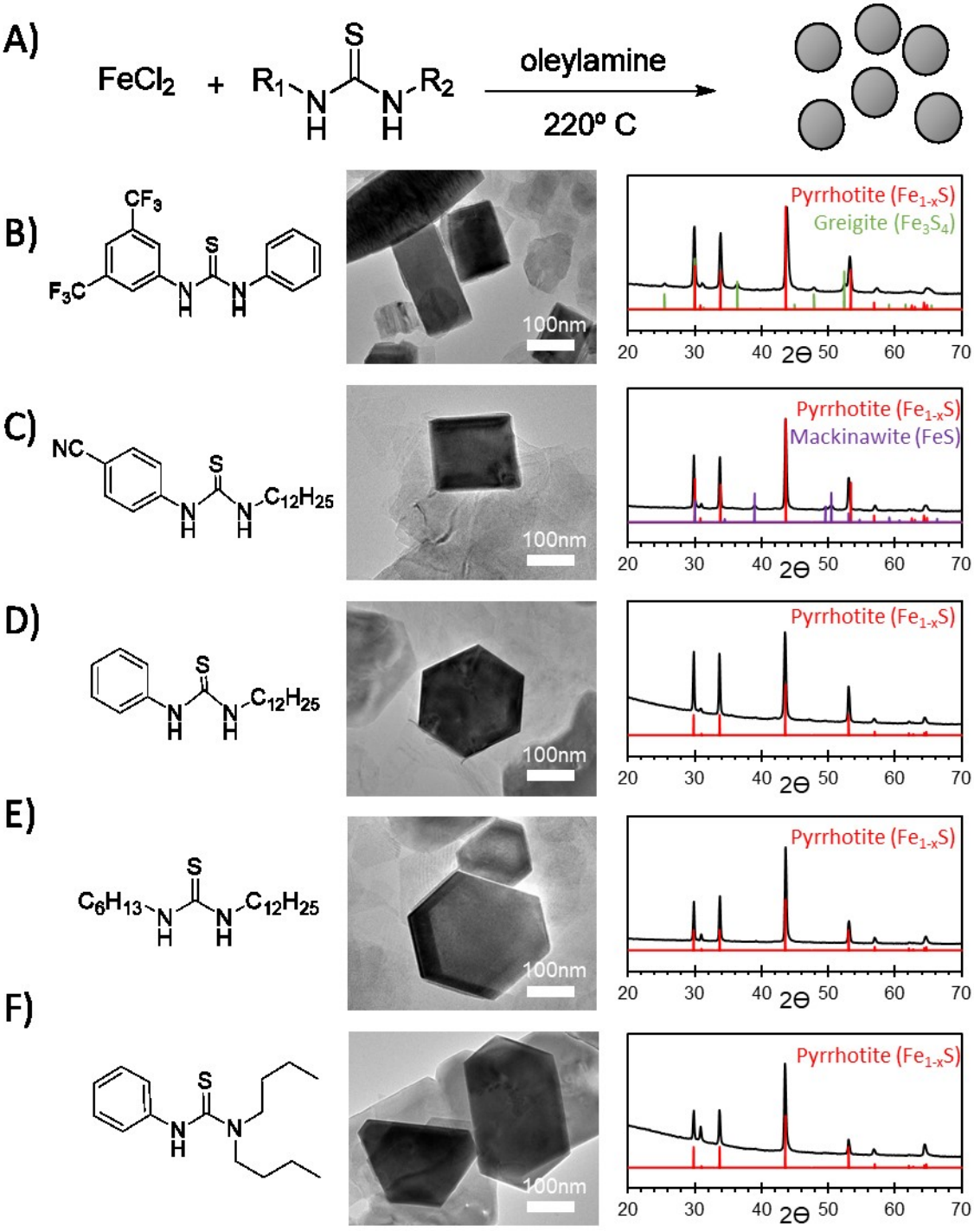

Figure 5.4: Synthesis of Fe-S nanocrystals using various substituted thioureas.

well as a trace mackinawite impurity (Figure 5.4c). Pyrrhotite hexagonal platelets were obtained

as a result of using the final three thioureas N-phenyl-N'-dodecylthiourea, N-hexyl-N'-dodecylthiourea, and N-phenyl-N',N'-dibutylthiourea (Figure 5.4d-f). Since pyrrhotite was the main product of all the thioureas used no conclusions can be made at this time. The presence of the greigite minor phase with the use of N-(3,5-bis(trifluoromethyl)phenyl)-N'-phenylthiourea was somewhat promising since greigite is a more sulfur rich phase compared to pyrrhotite, and that thiourea had the highest relative rate of decomposition in the series according to the study by Hendricks *et. al*.[157] Reaction conditions could be further tuned to further promote the formation of more sulfur rich phases. Furthermore, using monosubstituted thioureas would likely speed up the decomposition rate even more compared to di- and tri-substituted thioureas.

5.3 Kinetic control of nickel sulfides with para-substituted thiophenols

In addition to the iron sulfides, another metal chalcogenide system also investigated was the Ni-S system. In the summer of 2018, REU student Joe Veglak worked under my direction to investigate kinetic phase control of the nickel sulfide system using para-substituted thiophenols. The reactivity of para-substituted thiophenol reagents can be controlled by the electron donating or withdrawing ability of the substituent group. Ranked based on Hammett parameter, chloro- (Cl-), methyl- (CH_3-), methoxy- (CH_3O-), and amino- (NH_3-) substituted thiophenols were used in the reaction with nickel(II) chloride in oleylamine at 220°C in Figure 5.5. Phase control between polydymite (Ni_3S_4) and heazlewoodite (Ni_3S_4) correlated to the relative electron donating ability of the para- substituent on the thiophenol, where more electron donating strength resulted in the formation of the more sulfur poor phase, heazlewoodite. Further expansion of this library is certainly possible from commercially available reagents with even stronger electron donating or withdrawing groups.

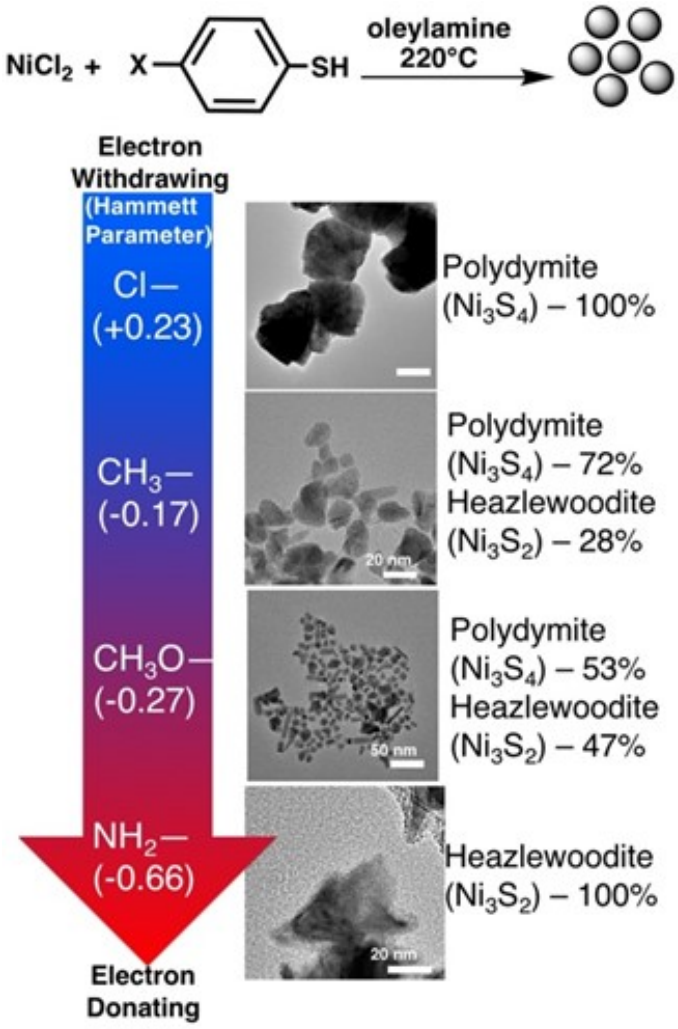

Figure 5.5: Reaction between $NiCl_2$ and various para-substituted thiophenols with increasing electron donating ability. More electron donating substituent groups results in the formation of more sulfur poor nickel sulfide phases.

5.4 Experimental methods

5.4.1 Computational methods

The computational methods used in this study were adapted from the work of Guo et al.[93] in which the bond dissociation energies (BDEs) of various dialkyl disulfides and diselenides were calculated. The BDEs in this study were calculated using Gaussian at the DFT level of theory and the Boese-Martin Kinetics (BMK) functional. Molecular geometries were optimized using the 6-31G(d) basis set followed by single-point energy calculations using the 6-311G(d,p) basis set.

5.4.2 Synthesis of deep eutectic mixture.

A method by Zhou[156] reported to synthesize para-disubstituted benzyl disulfides was adapted for the synthesis of 4,4'-(disulfanediylbis(methylene))dibenzonitrile (CN-Bz-SS-Bz-CN).

In order to synthesize the deep eutectic mixture to serve as the catalytic reaction medium for disulfide synthesis, a mixture of 0.1 mol choline chloride and 0.1 mol *p*-toluenesulfonic acid was heated at 100°C for 40 min until a clear solution was obtained. The solution was used for reactions without further purification.

5.4.3 Synthesis of sodium S-(4-cyanobenzyl) sulfurothioate.

In order to synthesize sodium S-(4-cyanobenzyl) sulfurothioate, first 20 mmol of 4-(bromomethyl) benzonitrile was added to a 100 mL three neck round bottom flask with 24 mmol of $Na_2S_2O_3 \cdot 5H_2O$, 20 mL of methanol, and 10 mL of water. The reaction mixture was stirred 16hr overnight to yield a white solid salt, to which 30 mL of a saturated NaCl solution was added and stirred for 1hr, followed by filtration and twice rinsed with saturated NaCl solution.

5.4.4 Synthesis of 4,4'-(disulfanediylbis(methylene))dibenzonitrile (CN-Bz-SS-Bz-CN).

In a 25 mL three-neck round bottom flask, 4.0 mmol of S-(4-cyanobenzyl) sulfurothioate was added with 20 mL of H_2O and 2 mL of the prepared deep eutectic mixture, followed by the slow addition of 12 mmol of 30% H_2O_2. The reaction mixture was stirred at 60°C for 6 hr. After completion, the solid precipitate was isolated via vacuum filtration, rinsed three times with water followed by rinsing with hexanes twice, and vacuum dried overnight (13hr).

5.4.5 Synthesis of Fe_xS_y nanocrystals with CN-Bz-SS-Bz-CN.

In a 25 mL 3-neck round-bottom flask, $FeCl_2$ (0.5 mmol) and 10 mL of OAm were placed under vacuum for 1 h at 60 °C. The temperature was increased to 170 °C and maintained for 1 h under an inert N_2 atmosphere. In a separate vial, 1.5 mmol of the prepared CN-Bz-SS-Bz-CN precursor was dissolved in 5 mL of OAm and placed under vacuum at room temperature for 45 min followed by backfilling with N_2 for 15 min. The disulfide/OAm solution was then injected into the reaction flask and heated to 220 °C for 2 h under N_2. The reaction solution was then cooled in air to room temperature, and ∼40 mL of chloroform was added, followed by centrifugation for 5−10 min at 8000 rpm. Particles were further purified by two cycles of suspension with chloroform followed by ethanol (total ∼20 mL) and then centrifugation for 5 min at 4400 rpm. The particles were stored in chloroform.

Chapter 6

Conclusion

6.1 Summary

Identifying and developing clean and renewable energy sources that are cost competitive with current nonrenewable energy technologies remains one of the great challenges of the 21st century. The ability to convert the virtually infinite supply of energy provided by the sun into a useful form is one of the most ideal options, but requires a great deal of work in order to one day replace polluting and limited fossil fuels. Iron pyrite-based photovoltaics have the potential to revolutionize the solar energy field from a materials cost and availability standpoint, but many issues need to be resolved in order to develop a pyrite cell with acceptable efficiency. This thesis represents a contribution to our understanding of the factors that contribute to the nanoscale phase selection of the vastly abundant iron sulfide materials.

In Chapter 2 an overview of the state of pyrite photovoltaic research is presented. Despite the attractive, nearly ideal properties for absorption of radiation from the sunlight, pyrite-based photovoltaics have not been able to meet expectations. The low efficiencies of pyrite solar devices have been attributed to anomalously low open circuit voltages. Low open circuit voltages and high dark saturation currents that are commonplace in pyrite cells are clues that suggest high levels of parasitic recombination due to the poor quality of pyrite crystals. The underlying causes have been categorized in three ways, namely, bulk defects, surface defects, and phase impurities. Historically there has been confusion as to the exact extent of bulk nonstoichiometry of pyrite samples, where early studies speculated that sulfur vacancies account for the apparent sulfur deficiency of FeS_{2-x}

with x as high as 0.25. But more recent computational data along with supporting experimental results conclude that the sulfur vacancy formation energy is quite high, and that pyrite is essentially a stoichiometric compound. Surface and interfacial sulfur vacancies are much more likely to occur due to a lower formation energy which results in a number of effects such as surface inversion layers and conductive states which are detrimental to performance. Also, apparent sulfur deficiency in pyrite samples is potentially due to the presence of sulfur deficient iron sulfide phases rather than bulk sulfur vacancies, so the preparation of high-quality phase pure pyrite nanocrystals is a prerequisite for high performing pyrite-based devices.

In Chapter 3, phase-controlled synthesis of iron sulfide nanocrystals is presented. Phase control is achieved based on sulfur precursor reactivity for a library of substituted sulfides, thiols, and disulfides. Precursor reactivity was defined in terms of ability to release an active sulfur species which would be the result of the breaking of a C-S bond in the alkyl substituted sulfur species. In general, lower C-S bond dissociation energies correlated to the precipitation of iron sulfide nanocrystals that were more sulfur rich. Of all the reagents used only allyl disulfide was able to produce iron pyrite, the most sulfur rich of the iron sulfide minerals. Allyl disulfide not only had the lowest C-S bond dissociation energy, but it also had unique chemistry available due to a special S_N2' reaction between the allylic substituent group and the nucleophilic oleylamine solvent. Evidence is provided that supports our hypothesis that allyl disulfide can potentially release persulfide S_2^{2-} units for the direct formation of pyrite, rather than through common pathways of sulfidation of sulfur poor and metastable iron sulfide phases.

In Chapter 4, a novel hybrid pyrite nanostructure is reported where cattierite CoS_2 is epitaxially grown on the surface of iron pyrite nanocubes. The morphology of the epitaxial CoS_2 layer could be varied between frames in which growth was mainly localized to edges and corners

of the pyrite nanocubes, or complete overgrowth based on the molar ratio of cobalt to sulfur precursor in the epitaxial growth stage of the reaction. Advanced imaging techniques such as STEM-EDS tomography were utilized confirming the core-frame morphology, which was achieved for the first time with two compound materials in the pyrite family. The system demonstrated activity toward the hydrogen evolution reaction (HER) in preliminary electrochemical tests. In an age where the demand for cobalt has increasingly driven up costs, a framed structure is a possibly efficient way to reduce material usage as well as improve activity for catalysis due to increasing surface to volume ratio of the catalytic material.

Chapter 5 includes preliminary and ongoing studies reevaluating phase control of the iron sulfide and other metal sulfide systems. In this chapter the kinetics of precursor decomposition are investigated by using a series of substituted thioureas and thiophenols as sulfur precursors. By using the same class of organosulfur reagents in a systematic study, the rate of decomposition can be isolated as the main factor contributing to phase control.

6.2 Future directions and outlook

Despite the significant improvements in cost and performance of silicon based solar cells, an efficient pyrite cell would be practically unbeatable in terms of materials availability and cost. In the second wave of effort to develop pyrite-based photovoltaics in the past decade, some of the fundamental issues are slowly starting to come into focus and become resolved. We are beginning to understand the nature of unintentional doping and the fundamental properties of pyrite better. One of the long-time puzzling observations was the nature of single crystalline samples that were ubiquitously identified as n-type samples, while all polycrystalline and nanocrystalline films were identified as having p-type conductivity. Studies by Zhang provide evidence that suggests that

perhaps the apparent p-type conductivity of polycrystalline and nano crystalline thin films were misinterpretations, as low mobility films or intergranular charge hopping based conductivity can often reverse the sign of the Hall coefficient.[158,159] Additionally, clearer evidence is emerging to identify the origin of *n*-type behavior of unintentionally doped pyrite crystals, with S vacancies as a main suspect.[53–55] More work in terms of identifying the true nature of conductivity and understanding the puzzling electronic properties of pyrite will be required in order to finally overcome the issue of low open circuit voltage that has restrained pyrite progress in photovoltaics.

In addition to further elucidating the fundamental electronic properties, advances in the synthetic methods for nanoscale pyrite film preparation will be required as well. Labile pyrite surfaces have been a longtime concern for photovoltaic applications, but one of the main benefits of colloidal nanoscale processing is the potential of complex ligand engineering for a variety of purposes such as surface passivation or improving charge transport properties.

Alternate tertiary olivine-type iron chalcogenide materials have also been proposed Fe_2MS_4 (M= Si,Ge) could possibly bypass issues associated with pyrite such as its tendency to phase separate into S-deficient conductive Fe-S phases, as well as replace the problematic S_2^{2-} persulfide units with simple S^{2-} atoms.[38] Studies on synthesizing the olivine type materials and testing in photovoltaic devices are accumulating.[160–165]

The verdict is not yet clear on whether pyrite can still be a key contributor to a cleaner and more sustainable future, or if we are just pursuing fool's gold. But the abundant, nontoxic, and incredibly cheap nature of pyrite has the potential to substantially lower the cost of solar energy even without achieving record breaking efficiencies. As of now, it is certainly still worth the pursuit.

References

1. Grätzel, M. Recent advances in sensitized mesoscopic solar cells. *Acc. Chem. Res*. **42**, 1788–1798 (2009).

2. Kamat, P. V. Meeting the clean energy demand: Nanostructure Architectures for Solar Energy Conversion. *Phys. Chem*. **392**, 2834–2860 (2007).

3. Talapin, D. V., Lee, J. S., Kovalenko, M. V. & Shevchenko, E. V. Prospects of colloidal nanocrystals for electronic and optoelectronic applications. *Chem. Rev*. **110**, 389–458 (2010).

4. Kwon, S. G. & Hyeon, T. Formation mechanisms of uniform nanocrystals via hot-injection and heat-up methods. *Small.* **7**, 2685–2702 (2011).

5. Lamer, V. K. & Dinegar, R. H. Theory, Production and Mechanism of Formation of Monodispersed Hydrosols. *J. Am. Chem. Soc*. **72**, 4847–4854 (1950).

6. Whitehead, C. B., Özkar, S. & Finke, R. G. LaMer's 1950 Model for Particle Formation of Instantaneous Nucleation and Diffusion-Controlled Growth: A Historical Look at the Model's Origins, Assumptions, Equations, and Underlying Sulfur Sol Formation Kinetics Data. *Chem. Mater*. **31**, 7116–7132 (2019).

7. Dabasch, R., Willeke, G. & Blenk, O. Iron Sulfide for Photovoltaics. *MRS Bull*. **18**, 56–60 (1993).

8. Kaur, G., Kaur, M., Thakur, A. & Kumar, A. Recent Progress on Pyrite FeS_2 Nanomaterials for Energy and Environment Applications: Synthesis, Properties and Future Prospects. *J. Cluster Sci.* **3**, (2019).

9. Shockley, W. & Queisser, H. J. Detailed balance limit of efficiency of p-n junction solar cells. *Appl. Phys*. **32**, 510–519 (1961).

10. Ennaoui, A., Fiechter, S., Pettenkofer, Ch., Alonso-Vante, N., Buker, K., Bronold, M. Hopfner, C., & Tributsch, H. Iron disulfide for solar energy conversion. *Sol. Energy Mater. Sol. Cells.* **29**, 289–370 (1993).

11. Puthussery, J., Seefeld, S., Berry, N., Gibbs, M. & Law, M. Colloidal Iron Pyrite (FeS_2) Nanocrystal Inks for Thin Film Photovoltaics. *J. Am. Chem. Soc*. **133**, 716–719 (2011).

12. Wadia, C., Alivisatos, A. P. & Kammen, D. M. Materials availability expands the opportunity for large-scale photovoltaics deployment. *Environ. Sci. Technol*. **43**, 2072–2077 (2009).

13. Woodhouse, M., Smith, B., Ramdas, A. & Robert Margolis. *Crystalline Silicon Photovoltaic Module Manufacturing Costs and Sustainable Pricing: 1H 2018 Benchmark and Cost Reduction Roadmap. National Renewable Energy Laboratory* (2019).

14. Jaegermann, W. & Tributsch, H. Photoelectrochemicai reactions of FeS_2 (pyrite) with t120 and reducing agents. *J. Appl. Electrochem*. **13**, 743–750 (1983).

15. Chatzitheodorou, G., Fiechter, S., Konenkamp, R., Kunst, M., Jargermann, W., & Tributsch, H. Thin photoactive FeS_2 (pyrite) films. *Mater. Res. Bull*. **21**, 1481–1487 (1986).

16. Smestad, G., Da Silva, A., Tributsch, H., Fiechter, S., Kunst, M., Meziani, N., Birkholz, M. Formation of semiconducting iron pyrite by spray pyrolysis. *Sol. Energy Mater.* **18**, 299–313 (1989).

17. Smestad, G., Ennaoui, A., Fiechter, S., Tributsch, H., Hofmann, & W. K., Birkholz, M. Photoactive thin film semiconducting iron pyrite prepared by sulfurization of iron oxides. *Sol. Energy Mater*. **20**, 149–165 (1990).

18. Ennaoui, A., Fiechter, S., Smestad, G. & Tributsch, H. Preparation of Iron Disulfide and Its Use for Solar Energy Conversion. *Energy and the Environment: Into the 1990s*.458–464 (Pergamon Press, 1990)

19. Ennaoui, A. & Tributsch, H. Iron sulphide solar cells. *Sol. Cells* **13**, 197–200 (1984).

20. Ennaoui, A., Fiechter, S., Goslowsky, H. & Tributsch, H. Photoactive Synthetic Polycrystalline Pyrite (FeS_2). *J. Electrochem. Soc*. **132**, 1579–1582 (1985).

21. Ennaoui, A., Fiechter, S., Jaegermann, W. & Tributsch, H. Photoelectrochemistry of Highly Quantum Efficient Single- Crystalline n-FeS (Pyrite). *J. Electrochem. Sci. Technol*. **133**, 97–106 (1986).

22. Ennaoui, A. & Tributsch, H. Energetic characterization of the photoactive FeS_2 (pyrite) interface. *Sol. Energy Mater*. **14**, 461–474 (1986).

23. Ennaoui, A. et al. Photoelectrochemical Energy Conversion Obtained with Ultrathin Organo-Metallic-Chemical-Vapor-Deposition Layer of FeS_2 (Pyrite) on TiO_2. *J. Electrochem. Soc*. **139**, 2514–2518 (1992).

24. Büker, K., Alonso-Vante, N. & Tributsch, H. Photovoltaic output limitation of n-FeS_2 (pyrite) Schottky barriers: A temperature-dependent characterization. *J. Appl. Phys*. **72**, 5721–5728 (1992).

25. Eyert, V., Höck, K.-H., Fiechter, S. & Tributsch, H. Electronic structure of FeS_2: The crucial role of electron-lattice interaction. *Phys. Rev. B.* **57**, 6350–6359 (1998).

26. Altermatt, P. P., Kiesewetter, T., Ellmer, K. & Tributsch, H. Specifying targets of future research in photovoltaic devices containing pyrite (FeS_2) by numerical modelling. *Sol. Energy Mater. Sol. Cells*. **71**, 181–195 (2002).

27. Steinhagen, C., Harvey, T. B., Stolle, C. J., Harris, J. & Korgel, B. A. Pyrite nanocrystal solar cells: Promising, or fool's gold? *J. Phys. Chem. Lett*. **3**, 2352–2356 (2012).

28. Bi, Y., Yuan, Y., Exstrom, C. L., Darveau, S. A. & Huang, J. Air Stable, Photosensitive, Phase Pure Iron Pyrite Nanocrystal Thin Films for Photovoltaic Application. *Nano Lett*. **11**, 4953–4957 (2011).

29. Morrish, R., Silverstein, R. & Colin, W. A. Synthesis of Stoichiometric FeS_2 through Plasma-Assisted Sulfurization of Fe_2O_3. *J. Am. Chem. Soc*. **134**, 17854–17857 (2012).

30. Wadia, C., Wu, Y., Gul, S., Volkman, S. K., Guo, J., Alivisatos, A. P. Surfactant-assisted hydrothermal synthesis of single-phase pyrite FeS_2 nanocrystals. *Chem. Mater*. **21**, 2568–2570 (2009).

31. Green, M. A., Hishikawa, Y., Dunlop, E. D., Levi, D. H., Hohl-Ebinger, J., Yoshita, M., Ho-Baillie, A. W. Y. Solar cell efficiency tables (Version 53). *Prog. Photovoltaics Res. Appl*. **27**, 3–12 (2019).

32. Yoshikawa, K., Kawasaki, H., Yoshida, W., Irie, T., Konishi, K., Nakano, K., Uto, T., Adachi, D., Kanematsu, M., Uzu, H., Yamamoto, K. Silicon heterojunction solar cell with interdigitated back contacts for a photoconversion efficiency over 26%. *Nat. Energy*. **2**, 17032 (2017).

33. Voigt, B., Moore, W., Manno, M., Walter, J., Jeremiason, J. D., Aydil, E. S., Leighton, C. Transport Evidence for Sulfur Vacancies as the Origin of Unintentional n-Type Doping in Pyrite FeS_2. *ACS Appl. Mater. Interfaces*. **11**, 15552–15563 (2019).

34. Zhang, X., Scott, T., Socha, T., Nielsen, D., Manno, M., Joshnson, M., Yan, Y., Losovyj, Y., Dowben P., Aydil E. S., Leighton C. Phase Stability and Stoichiometry in Thin Film Iron Pyrite: Impact on Electronic Transport Properties. *ACS Appl. Mater. Interfaces.* **7**, 14130–14139 (2015).

35. Rahman, M. Z. & Edvinsson, T. What Is Limiting Pyrite Solar Cell Performance? *Joule*. **3**, 2282–2293 (2019).

36. Luck, J., Hartmann, A. & Fiechter, S. Stoichiometry and impurity concentration in synthetically grown iron pyrite crystals and their constituents. *Fresenius' Zeitschrift für Anal. Chemie*. **334**, 441–446 (1989).

37. Birkholz, M., Fiechter, S., Hartmann, A. & Tributsch, H. Sulfur deficiency in iron pyrite (FeS_{2-x}) and its consequences for band-structure models. *Phys. Rev. B*. **43**, 11926–11936 (1991).

38. Yu, L., Lany, S., Kykynyshi, R., Jieratum, V., Ravichandran, R., Pelatt, B., Altschul, E., Platt, H. A. S., Wager, J. F., Keszler, D. A., Zunger, A. Iron chalcogenide photovoltaic absorbers. *Adv. Energy Mater*. **1**, 748–753 (2011).

39. Hu, J., Zhang, Y., Law, M. & Wu, R. First-principles studies of the electronic properties of native and substitutional anionic defects in bulk iron pyrite. *Phys. Rev. B - Condens. Matter Mater. Phys*. **85**, 1–10 (2012).

40. Herbert, F. W., Krishnamoorthy, A., Van Vliet, K. J. & Yildiz, B. Quantification of electronic band gap and surface states on FeS_2(100). *Surf. Sci*. **618**, 53–61 (2013).

41. Sun, R., Chan, M. K. Y. & Ceder, G. First-principles electronic structure and relative stability of pyrite and marcasite: Implications for photovoltaic performance. *Phys. Rev. B - Condens. Matter Mater. Phys*. **83**, 1–12 (2011).

42. Ganduglia-Pirovano, M. V., Hofmann, A. & Sauer, J. Oxygen vacancies in transition metal and rare earth oxides: Current state of understanding and remaining challenges. *Surf. Sci. Rep*. **62**, 219–270 (2007).

43. McAuliffe, R. D. & Shoemaker, D. P. Inflexible stoichiometry in bulk pyrite FeS_2 as viewed by in situ and high-resolution X-ray diffraction. *Acta Crystallogr. Sect. B Struct. Sci. Cryst. Eng. Mater*. **74**, 436–444 (2018).

44. Alonso-Vante, N., Chatzitheodorou, G., Fiechter, S., Mgoduka, N., Poulios, I., Tributsch, H. Interfacial behavior of hydrogen-treated sulphur deficient pyrite (FeS_{2-x}). *Sol. Energy Mater*. **18**, 9–21 (1988).

45. Ellmer, K. & Höpfner, C. On the stoichiometry of the semiconductor pyrite (FeS_2). *Philos. Mag. A*. **75**, 1129–1151 (1997).

46. Berry, N., Cheng, M., Perkins, C. L., Limpinsel, M., Hemminger, J. C., Law, M. Atmospheric-pressure chemical vapor deposition of iron pyrite thin films. *Adv. Energy Mater*. **2**, 1124–1135 (2012).

47. Fiechter, S., Birkholz, M., Hartmann, A., Dulski, P., Giersig, M., Tributsch, H. The microstructure and stoichiometry of pyrite FeS_{2x}. *J. Mater. Res*. **7**, 1829–1838 (1992).

48. Fukui, T. & Miyadai, T. Photoconductivity of Natural Pyrite (FeS_2). *J. Phys. Soc. Japan*. **31**, 1277 (1971).

49. Chongyang, L., Pettenkofer, C. & Tributsch, H. Enhancement of photoactivity in pyrite (FeS_2) interfaces by photoelectrochemical processes. *Surf. Sci*. **204**, 537–554 (1988).

50. Murphy, R. & Strongin, D. R. Surface reactivity of pyrite and related sulfides. *Surf. Sci. Rep*. **64**, 1–45 (2009).

51. Zhang, Y. N., Hu, J., Law, M. & Wu, R. Q. Effect of surface stoichiometry on the band gap of the pyrite FeS_2(100) surface. *Phys. Rev. B - Condens. Matter Mater. Phys*. **85**, 1–5 (2012).

52. Walter, J., Zhang, X., Voigt, B., Hool, R., Manno, M., Mork, F., Aydil, E. R., Leighton, C. Surface conduction in n -type pyrite FeS_2 single crystals. *Phys. Rev. Mater*. **1**, 1–17 (2017).

53. Liang, D., Cabán-Acevedo, M., Kaiser, N. S. & Jin, S. Gated Hall Effect of Nanoplate Devices Reveals Surface-State-Induced Surface Inversion in Iron Pyrite Semiconductor. *Nano Lett*. **14**, 6754–6760 (2014).

54. Herbert, F. W., Krishnamoorthy, A., Ma, W., Van Vliet, K. J. & Yildiz, B. Dynamics of point defect formation, clustering and pit initiation on the pyrite surface. *Electrochim. Acta.* **127**, 416–426 (2014).

55. Andersson, K. J., Ogasawara, H., Nordlund, D., Brown, G. E. & Nilsson, A. Preparation, Structure, and Orientation of Pyrite FeS_2 {100} Surfaces: Anisotropy, Sulfur Monomers, Dimer Vacancies and a Possible FeS Surface Phase. *J. Phys. Chem. C.* **118.** 21896-21903 (2014).

56. Seefeld, S., Limpinsel, M., Liu, Y., Farhi, N., Weber, A., Zhang, Y., Berry, N., Kwon, Y. J., Perkins, C. L., Hemminger, J. C., Wu, R., Law, M. Iron Pyrite Thin Films Synthesized from an $Fe(acac)_3$ Ink. *J. Am. Chem. Soc*. **135**, 4412–4424 (2013).

57. Limpinsel, M., Farhi, N., Berry, N., Lindemuth, J., Perkins, C. L., Lin, Q., Law, M. An inversion layer at the surface of n-type iron pyrite. *Energy Environ. Sci*. **7**, 1974 (2014).

58. Cabán-Acevedo, M., Kaiser, N. S., English, C. R., Liang, D., Thompson, B. J., Chen, H., Czech, K. J., Wright, J. C., Hamers, R. J., Jin, J. Ionization of high-density deep donor defect states explains the low photovoltage of iron pyrite single crystals. *J. Am. Chem. Soc*. **136**, 17163–17179 (2014).

59. Jagadeesh, M. S. & Seehra, M. S. Electrical Resistivity and Band Gap of Marcasite (FeS_2). *Phys. Lett*. **80**, 77–79 (1980).

60. Sánchez, C., Flores, E., Barawi, M., Clamagirand, J. M., Ares, J. R., Ferrer, I. J. Marcasite revisited: Optical absorption gap at room temperature. *Solid State Commun*. **230**, 20–24 (2016).

61. Moon, D. G., Rehan, S., Lim, S. Y., Nam, D., Seo, I., Gwak, J., Cheong, H., Cho, Y. S., Lee, Y., Ahn, S. Structural, optical and electrical impacts of marcasite in pyrite thin films. *Sol. Energy.* **159**, 930–939 (2018).

62. Wu, L., Dzade, N. Y., Gao, L., Scanlon, D. O., Ozturk, Z., Hollingsworth, N., Weckhuysen, B. M., Hnesen, E. J. M., de Leeuw, N. H., Hofmann, J. P. Enhanced Photoresponse of FeS_2 Films: The Role of Marcasite Pyrite Phase Junctions. *Adv. Mater.* **28**, 9602–9607 (2016).

63. Rickard, D. & Luther, G. W. Chemistry of iron sulfides. *Chem. Rev*. **107**, 514–562 (2007).

64. Vaughan, D. J. & Lennie, A. R. The iron sulfide minerals - their chemistry and role in nature. *Sci Prog*. **75**, 371–388 (1991).

65. Benning, L. G., Wilkin, R. T. & Barnes, H. L. Reaction pathways in the Fe-S system below 100°C. *Chem. Geol*. **167**, 25–51 (2000).

66. Hunger, S. & Benning, L. G. Greigite: A true intermediate on the polysulfide pathway to pyrite. *Geochem. Trans*. **8**, 1–20 (2007).

67. Matamoros-Veloza, A., Stawski, T. M. & Benning, L. G. Nanoparticle Assembly Leads to Mackinawite Formation. *Cryst. Growth Des*. **18**, 6757–6764 (2018).

68. Clayton, A. J., Irvine, S. J. C., Barrioz, V., Brooks, W. S. M., Zoppi, G., Forbes, I., Rogers, K. D., Lane, D. W., Hutchings, K., Roncallo, S. Metal-organic chemical vapor deposition of ultra-thin photovoltaic devices using a pyrite based p-i-n structure. *Thin Solid Films*. **519**, 7360–7363 (2011).

69. Khalid, S., Ahmed, E., Khan, Y., Riaz, K. N. & Malik, M. A. Nanocrystalline Pyrite for Photovoltaic Applications. *ChemistrySelect*. **3**, 6488–6524 (2018).

70. Van Embden, J., Chesman, A. S. R. & Jasieniak, J. J. The heat-up synthesis of colloidal nanocrystals. *Chem. Mater*. **27**, 2246–2285 (2015).

71. Kershaw, S. V, Susha, A. S. & Rogach, A. L. Narrow bandgap colloidal metal chalcogenide quantum dots: synthetic methods, heterostructures, assemblies, electronic and infrared optical properties. *Chem. Soc. Rev.* **42**, 3033–87 (2013).

72. Choi, S. H., An, K., Kim, E., Yu, J. H., Kim, J. H., Hyeon, T. Simple and generalized synthesis of semiconducting metal sulfide nanocrystals. *Adv. Funct. Mater*. **19**, 1645–1649 (2009).

73. Joo, J., Na, H. B., Yu, T., Yu, J. H., Kim, Y. W., Wu, F., Zhang, J. Z., Hyeon, T. Generalized and facile synthesis of semiconducting metal sulfide nanocrystals. *J. Am. Chem*. *Soc*. **125**, 11100–5 (2003).

74. Douglas, A., Carter, R., Oakes, L., Share, K., Cohn, A. P., Pint, C. L. Ultrafine Iron Pyrite (FeS_2) Nanocrystals Improve Sodium-Sulfur and Lithium-Sulfur Conversion Reactions for Efficient Batteries. *ACS Nano*. **9.** 11156-11165 (2015).

75. Roberts, A. P., Chang, L., Rowan, C. J., Horng, C.-S. & Florindo, F. Magnetic properties of sedimentary greigite (Fe_3S_4): an update. *Rev. Geophys*. **49**, RG1002 (2011).

76. Rui, X., Tan, H. & Yan, Q. Nanostructured metal sulfides for energy storage. *Nanoscale*. **6**, 9889–9924 (2014).

77. Posfai, M., Buseck, P. R., Bazylinski, D. A. & Frankel, R. B. Reaction Sequence of Iron Sulfide Minerals in Bacteria and Their Use as Biomarkers. *Science*. **280**, 880–883 (1998).

78. Feng, M., Lu, Y., Yang, Y., Zhang, M., Xu, Y., Gao, H., Dong, L., Xu, W., Yu, S. Bioinspired greigite magnetic nanocrystals: chemical synthesis and biomedicine applications. *Sci. Rep*. **3**, 2994 (2013).

79. Wu, B., Song, H., Zhou, J. & Chen, X. Iron sulfide-embedded carbon microsphere anode material with high-rate performance for lithium-ion batteries. *Chem. Commun*. **47**, 8653–8655 (2011).

80. Jiang, F., Peckler, L. T. & Muscat, A. J. Phase Pure Pyrite FeS_2 Nanocubes Synthesized Using Oleylamine as Ligand, Solvent, and Reductant. *Cryst. Growth Des*. **15**, 3565–3572 (2015).

81. Li, W., Doblinger, M., Vaneski, A., Rogach, Jackel, F., Feldmann, J. Pyrite nanocrystals: shape-controlled synthesis and tunable optical properties via elf-assembly. *J. Mater. Chem*. **21**, 17946–17952 (2011).

82. Ge, H., Hai, L., Prabhakar, R. R., Ming, L. Y. & Sritharan, T. Evolution of nanoplate morphology, structure and chemistry during synthesis of pyrite by a hot injection method. *RSC Adv*. **4**, 16489 (2014).

83. Gong, M., Kirkeminde, A. & Ren, S. Symmetry-defying iron pyrite (FeS_2) nanocrystals through oriented attachment. *Sci. Rep*. **3**, 2092 (2013).

84. Lucas, J. M., Tuan, C., Lounis, S. D., Britt, D. K., Qiao, R., Yang, W., Lanzara, A., Alivisatos, A. P. Ligand-controlled colloidal synthesis and electronic structure characterization of cubic iron pyrite (FeS_2) nanocrystals. *Chem. Mater*. **25**, 1615–1620 (2013).

85. MacPherson, H. A. & Stoldt, C. R. Iron pyrite nanocubes: Size and shape considerations for photovoltaic application. *ACS Nano*. **6**, 8940–8949 (2012).

86. Xian, H., Zhu, J., Liang, X. & He, H. Morphology controllable syntheses of micro- and nano-iron pyrite mono- and poly-crystals: a review. *RSC Adv*. **6**, 31988–31999 (2016).

87. Akhtar, M., Akhter, J., Malik, M. A., O'Brien, P., Tuna, F., Raftery, J., Helliwell, M. Deposition of iron sulfide nanocrystals from single source precursors. *J. Mater. Chem*. **21**, 9737 (2011).

88. Yuan, B. X., Luan, W. L., Tu, S. T. & Wu, J. One-step synthesis of pure pyrite FeS_2 with different morphologies in water. *New J. Chem*. **39**, 3571–3577 (2015).

89. Vanitha, P. V. & O'Brien, P. Phase control in the synthesis of magnetic iron sulfide nanocrystals from a cubane-type Fe-S cluster. *J. Am. Chem. Soc*. **130**, 17256–17257 (2008).

90. Vela, J. Molecular chemistry to the fore: New insights into the fascinating world of photoactive colloidal semiconductor nanocrystals. *J. Phys. Chem. Lett*. **4**, 653–668 (2013).

91. Alvarado, S. R., Guo, Y., Ruberu, T. P. a, Tavasoli, E. & Vela, J. Inorganic chemistry solutions to semiconductor nanocrystal problems. *Coord. Chem. Rev*. **263–264**, 182–196 (2014).

92. Brutchey, R. L. Diorganyl Dichalcogenides as Useful Synthons for Colloidal Semiconductor Nanocrystals. *Acc. Chem. Res*. **48**, 2918–2926 (2015).

93. Guo, Y., Alvarado, S. R., Barclay, J. D. & Vela, J. Shape-programmed nanofabrication: Understanding the reactivity of dichalcogenide precursors. *ACS Nano.* **7**, 3616–3626 (2013).

94. Ruberu, T. P. A., Albright, H. R., Callis, B., Ward, B., Cisneros, J., Fan, H., Vela, J. Molecular Control of the Nanoscale : Effect of Phosphine-Chalcogenide Reactivity on CdS-CdSe Nanocrystal. *ACS Nano.* **6**, 5348–5359 (2012).

95. Hendricks, M. P., Campos, M. P., Cleveland, G. T., Jen-La Plante, I. & Owen, J. S. A tunable library of substituted thiourea precursors to metal sulfide nanocrystals. *Science*. **348**, 1226–1230 (2015).

96. Andaraarachchi, H. P., Thompson, M. J., White, M. A., Fan, H. J. & Vela, J. Phase-Programmed Nanofabrication: Effect of Organophosphite Precursor Reactivity on the Evolution of Nickel and Nickel Phosphide Nanocrystals. *Chem. Mater*. **27**, 8021–8031 (2015).

97. Qiao, L., Fu, Z., Li, J., Ghosen, J., Zeng, M., Stebbins, J., Prasad, P. N., Swihart, M. T. Standardizing Size- and Shape-Controlled Synthesis of Monodisperse Magnetite (Fe_3O_4) Nanocrystals by Identifying and Exploiting Effects of Organic Impurities. *ACS Nano*. **11**, 6370–6381 (2017).

98. Wilkin, R. T. & Barnes, H. L. Formation processes of framboidal pyrite. *Geochim. Cosmochim. Acta*. **61**, 323–339 (1997).

99. Wilkin, R. T. & Barnes, H. L. Pyrite formation by reactions of iron monosulfides with dissolved inorganic and organic sulfur species. *Geochim. Cosmochim. Acta*. **60**, 4167–4179 (1996).

100. Thomson, J. W., Nagashima, K., Macdonald, P. M. & Ozin, G. A. From Sulfur-Amine Solutions to Metal Sulfide Nanocrystals – Peering into the Oleylamine- Sulfur Black Box. *J. Am. Chem. Soc.* **133**, 5036–5041 (2011).

101. Shukla, S., Xing, G., Ge, H., Prabhakar, R. R., Mathew, S., Su, Z., Nalla, V., Venkatesan, T., Mathews, N., Sritharan, T., Sum, T. C., Xiongm Q. Origin of Photocarrier Losses in Iron Pyrite (FeS_2) Nanocubes. *ACS Nano*. **10**, 4431–4440 (2016).

102. Cabán-Acevedo, M., Kaiser, N. S., English, C. R., Liang, D., Thompson, B. J., Chen, H., Czech, K. J., Wright, J. C., Hamers, R. J., Jin, S. Ionization of high-density deep donor defect states explains the low photovoltage of iron pyrite single crystals. *J. Am. Chem. Soc*. **136**, 17163–17179 (2014).

103. Boughriet, A., Figueiredo, R. S., Laureyns, J. & Recourt, P. Identification of newly generated iron phases in recent anoxic sediments: ^{57}Fe Mossbauer and micro-Raman spectroscopic studies. *J. Chem. Soc*., *Faraday Trans*. **93**, 3209–3215 (1997).

104. Bourdoiseau, J. A., Jeannin, M., Remazeilles, C., Sabot, R. & Refait, P. The transformation of mackinawite into greigite studied by Raman spectroscopy. *J. Raman Spectrosc*. **42**, 496–504 (2011).

105. Kleppe, A. K. & Jephcoat, A. P. High-pressure Raman spectroscopic studies of FeS_2 pyrite. Mineral. Mag. 68, 433–441 (2004).

106. Wilcoxon, J.P.; Newcomer, P.P.; Samara, G. A. Strong Quantum Confinement Effects in Semiconductors: FeS_2 Nanoclusters. *Solid State Commun*. **98**, 581–585 (1996).

107. Li, T., Li, H., Wu, Z., Hao, H., Liu, J., Huang, T., Sun, H., Zhang, J., Zhang, H. Guo, Z. Colloidal synthesis of greigite nanoplates with controlled lateral size for electrochemical. *Nanoscale*. **7**, 4171–4178 (2015).

108. Mourdikoudis, S. & Liz-Marzán, L. M. Oleyamine in Nanoparticle Synthesis. *Chem. Mater.* **25**, 1465 (2013).

109. Block, E. The organosulfur chemistry of the genus Allium - Implications for the organic chemistry of sulfur. *Angew. Chemie - Int. Ed. English*. **31**, 1135–1178 (1992).

110. Block, E., Iyer, R., Grisoni, S., Saha, C., Belman, S., Lossing, F. P. Lipoxygenase Inhibitors from the Essential Oil of Garlic. Markovnikow Addition of the Allyldithio Radical to Olefins. *J. Am. Chem. Soc*. **110**, 7813–7827 (1988).

111. Hofle, G. & Baldwin, J. E. Thiosulfoxides. The Intermediates in Rearrangement and Reduction of Allylic Disulfides. *J. Am. Chem. Soc*. **2**, 6307–6308 (1971).

112. Moore, C. G. & Watson, A. A. The Reaction of Alkenethiolate Ions With Dialkenyl Disulphides To Give Dialkenyl Monosulphides. *Tetrahedron* **18**, 219–225 (1962).

113. Thiedemann, B., Schmitz, C. M. L. & Staubitz, A. Reduction of N -allylamides by $LiAlH_4$: Unexpected attack of the double bond with mechanistic studies of product and byproduct formation. *J. Org. Chem*. **79**, 10284–10295 (2014).

114. Uygun, M., Tasdelen, M. A. & Yagci, Y. Influence of type of initiation on thiol-ene 'click' Chemistry. Macromol. *Chem. Phys*. **211**, 103–110 (2010).

115. Banin, U., Ben-Shahar, Y. & Vinokurov, K. Hybrid semiconductor-metal nanoparticles: From architecture to function. *Chem. Mater*. **26**, 97–110 (2014).

116. Costi, R., Saunders, A. E. & Banin, U. Colloidal hybrid nanostructures: A new type of functional materials. *Angew. Chemie - Int. Ed*. **49**, 4878–4897 (2010).

117. Shukla, S., Ager, J. W., Xiong, Q. & Sritharan, T. Scientific and Techonological Assessment of Iron Pyrite for Use in Solar Devices. *Energy Technol*. **6**, 8–20 (2018).

118. Gao, M. R., Zheng, Y. R., Jiang, J. & Yu, S. H. Pyrite-Type Nanomaterials for Advanced Electrocatalysis. *Acc. Chem. Res*. **50**, 2194–2204 (2017).

119. McGrath, A. J., Dual-Functional Optoelectronic and Magnetic Pyrite/Iron Selenide Core/Shell Nanocrystals. *J. Phys. Chem. C* **121**, 8220–8226 (2017).

120. Tan, R., Yang, J., Hu, J., Wang, K., Zhao, Y., Pan, F. Core–shell nano-FeS_2@N-doped graphene as an advanced cathode material for rechargeable Li-ion batteries. *Chem. Commun*. **52**, 986–989 (2016).

121. Wang, D. Y., Gong, M. Chou, H., Pan, C., Chen, H., Wu, Y., Lin, M., Guan, M., Yang, J., Chen C., Wang, Y., Hwang, B., Chen, C., Dai, H. Highly active and stable hybrid catalyst of cobalt-doped FeS_2 nanosheets-carbon nanotubes for hydrogen evolution reaction. *J. Am. Chem. Soc*. **137**, 1587–1592 (2015).

122. Yu, Q., Cai, S., Jin, Z. & Yan, Z. Evolutions of composition, microstructure and optical properties of Mn-doped pyrite (FeS_2) films prepared by chemical bath deposition. *Mater. Res. Bull*. **48**, 3601–3606 (2013).

123. Thomas, B., Ellmer, K., Bohne, W., Rohrich, J., Kunst, M., Tributsch, H. Photoeffects in cobalt doped pyrite (FeS_2) films. Solid State Commun. **111**, 235–240 (1999).

124. Zhang, K., Park, M., Zhou, L. Lee, G., Shin, J., Hu, Z., Chou, S. Chen, J., Kang, Y. Cobalt-Doped FeS_2 Nanospheres with Complete Solid Solubility as a High-Performance Anode Material for Sodium-Ion Batteries. *Angew. Chemie Int. Ed*. **55**, 12822–12826 (2016).

125. Jiao, J., Chen, L., Kuang, D., Gao, W., Feng, H., Xia, J. Synthesis of FeS_2 and Co-doped FeS_2 films with the aid of supercritical carbon dioxide and their photoelectrochemical properties. *RSC Adv*. **1**, 255 (2011).

126. Gabold, H., Luan, Z., Paul, N., Opel, M., Muller-Buschbaum, P., Law, M., Paul, A. Structural and magnetic properties of cobalt iron disulfide ($Co_xFe_{1-x}S_2$) nanocrystals. *Sci. Rep*. **8**, 4835 (2018).

127. Kinner, T., Bhandari, K. P., Bastola, E., Monahan, B. M., Haugen, N. O., Roland, P. J., Bigioni, T. P., Ellingson, R. J. Majority Carrier Type Control of Cobalt Iron Sulfide ($Co_xFe_{1-x}S_2$) Pyrite Nanocrystals. *J. Phys. Chem. C* **120**, 5706–5713 (2016).

128. Gilroy, K. D., Ruditskiy, A., Peng, H. C., Qin, D. & Xia, Y. Bimetallic nanocrystals: Syntheses, properties, and applications. *Chem. Rev*. **116**, 10414–10472 (2016).

129. Wu, Y., Sun, X., Yang, Y., Li, J., Zhang, Y., Qin, D. Enriching Silver Nanocrystals with a Second Noble Metal. *Acc. Chem. Res*. **50**, 1774–1784 (2017).

130. Oh, A., Baik, h., Choi, D., Cheon, J. Y., Kim, B., Kim, H., Kwon, S. J., Joo, S. H., Jung, Y., Lee, K. Skeletal octahedral nanoframe with cartesian coordinates via geometrically precise nanoscale phase segregation in a Pt@Ni core-shell nanocrystal. *ACS Nano* **9**, 2856–2867 (2015).

131. Zhang, Y., Ahn, J., Liu, J. & Qin, D. Syntheses, Plasmonic Properties, and Catalytic Applications of Ag–Rh Core-Frame Nanocubes and Rh Nanoboxes with Highly Porous Walls. *Chem. Mater*. **30,** 2151-2159(2018)

132. Ahn, J., Wang, D., Ding, Y., Zhang, J. & Qin, D. Site-Selective Carving and Co-Deposition: Transformation of Ag Nanocubes into Concave Nanocrystals Encased by Au-Ag Alloy Frames. *ACS Nano* **12**, 298–307 (2018).

133. Mathurin, L. E., Tao, J., Xin, H., Li, J., Zhu, Y., Chen, J. Dendritic Core-Frame and Frame Multimetallic Rhombic Dodecahedra: A Comparison Study of Composition and Structure Effects on Electrocatalysis of Methanol Oxidation. *CHEMNANOMAT* **4**, 76–87 (2018).

134. Park, J., Sa, Y. J., Baik, H., Kwon, T., Joo, Sang, H., Lee, K. Iridium-Based Multimetallic Nanoframe@Nanoframe Structure: An Efficient and Robust Electrocatalyst toward Oxygen Evolution Reaction. *ACS Nano* **11**, 5500–5509 (2017).

135. Jin, H., Hong, Y., Yoon, J., Oh, A., Chaudhari, N. K., Baik, H., Joo, S. H., Lee, K. Lanthanide metal-assisted synthesis of rhombic dodecahedral MNi (M = Ir and Pt) nanoframes toward efficient oxygen evolution catalysis. *NANO ENERGY* **42**, 17–25 (2017).

136. Ni, B. & Wang, X. Face the Edges: Catalytic Active Sites of Nanomaterials. *Adv. Sci*. **2**, 1500085 (2015).

137. Macdonald, J. E., Bar Sadan, M., Houben, L., Popov, I. & Banin, U. Hybrid nanoscale inorganic cages. *Nat. Mater*. **9**, 810–815 (2010).

138. Vinokurov, K. Bekenstein, Y., Gutkin, V., Popov, I., Millo, O., Banin, U. Rhodium growth on Cu_2S nanocrystals yielding hybrid nanoscale inorganic cages and their synergistic properties. *CrystEngComm* **16**, 9506–9512 (2014).

139. Vinokurov, K., MacDonald, J. E. & Banin, U. Structures and mechanisms in the growth of hybrid Ru-Cu_2S nanoparticles: From cages to nanonets. *Chem. Mater*. **24**, 1822–1827 (2012).

140. Orfield, N. J., McBride, J. R., Wang, F., Buck, M., Keene, J. D., Reid, K. R., Htoon, H., Hollingsworth, J. A., Rosenthal, S. J. Quantum Yield Heterogeneity among Single Nonblinking Quantum Dots Revealed by Atomic Structure-Quantum Optics Correlation. *ACS Nano* **10**, 1960–1968 (2016).

141. Ben-Shahar, Y. & Banin, U. Hybrid Semiconductor–Metal Nanorods as Photocatalysts. *Top. Curr. Chem*. **374**, 1–26 (2016).

142. Jasion, D., Barforoush, J. M., Qiao, Q., Zhu, Y., Ren, S., Leonard, K. C. Low-Dimensional Hyperthin FeS_2 Nanostructures for Efficient and Stable Hydrogen Evolution Electrocatalysis. *ACS Catal*. **5**, 6653–6657 (2015).

143. Paszkowicz, W. & Leiro, J. A. Rietveld refinement study of pyrite crystals. *J. Alloys Compd*. **401**, 289–295 (2005).

144. Faber, M. S., Lukowski, M. A., Ding, Q., Kaiser, N. S. & Jin, S. Earth-Abundant Metal Pyrites (FeS_2, CoS_2, NiS_2, and Their Alloys) for Highly Efficient Hydrogen Evolution and Polysulfide Reduction Electrocatalysis. *J. Phys. Chem. C* **118**, 21347–21356 (2014).

145. Anastassakis, E. & Perry, C. H. Light scattering and IR measurements in XS_2 pyrite-type compounds. *J. Chem. Phys*. **64**, 3604–3609 (1976).

146. Alfonso, D. R. Computational investigation of FeS_2 surfaces and prediction of effects of sulfur environment on stabilities. *J. Phys. Chem. C* **114**, 8971–8980 (2010).

147. Faber, M. S., Dziedzic, R., Lukowski, M. A., Kaiser, N. S. & Ding, Q. High-Performance Electrocatalysis Using Metallic Cobalt Pyrite (CoS_2) Micro- and Nanostructures. *J. Am. Chem. Soc*. **136**, 10053–10061 (2014).

148. Faber, M. S. & Jin, S. Earth-abundant inorganic electrocatalysts and their nanostructures for energy conversion applications. *Energy Environ. Sci*. **7**, 3519–3542 (2014).

149. Cabán-Acevedo, M. et al. Efficient hydrogen evolution catalysis using ternary pyrite-type cobalt phosphosulphide. *Nat. Mater*. **14**, 1245–51 (2015).

150. Xiong, W., Guo, Z., Li, H., Zhao, R. & Wang, X. Rational Bottom-Up Engineering of Electrocatalysts by Atomic Layer Deposition: A Case Study of $Fe_x Co_{1-x} S_y$ -Based Catalysts for Electrochemical Hydrogen Evolution. *ACS Energy Lett*. **2**. 2778–2785 (2017).

151. Jirkovský, J. S., Björling, A. & Ahlberg, E. Reduction of oxygen on dispersed nanocrystalline CoS_2. *J. Phys. Chem. C* **116**, 24436–24444 (2012).

152. Zhu, L., Susac, D., Teo, M., Wong, K. C., Wong, P. C., Parsons, R. R., Bizzotto, D., Mitchell, K. A. R., Campbell, S. A. Investigation of CoS_2-based thin films as model catalysts for the oxygen reduction reaction. *J. Catal*. **258**, 235–242 (2008).

153. Zhao, C., Li, D. & Feng, Y. Size-controlled hydrothermal synthesis and high electrocatalytic performance of CoS_2 nanocatalysts as non-precious metal cathode materials for fuel cells. *J. Mater. Chem. A* **1**, 5741 (2013).

154. Scott, A. Metal prices challenge battery sector. *C&EN* **95**, 21–23 (2017).

155. Kratzig, A., Zachaus, C., Brunken, S., Thomas, D., Bogdanoff, Ellmer, K., Fiechter, S. RuS_2 thin films as oxygen-evolving electrocatalyst: Highly oriented growth on single-crystal FeS_2 substrate and their properties compared to polycrystalline layers. *Phys. Status Solidi Appl. Mater. Sci*. **211**, 2020–2029 (2014).

156. Zhou, Y. Deep eutectic mixture catalysed the synthesis of disulfides using Bunte salts as thiol surrogates. *J. Chem. Res*. **39**, 332–335 (2015).

157. Hendricks, M. P., Campos, M. P., Cleveland, G. T., Plante, I. J. La & Owen, J. S. A Tunable library of substituted thiourea precursors to metal sulfide nanocrystals. *Science*. **348**, 1226–1230 (2015).

158. Zhang, X., Manno, M., Baruth, A., Johnson, M., Aydil, E. S., Leighton, C. Crossover from nanoscopic intergranular hopping to conventional charge transport in pyrite thin films. *ACS Nano* **7**, 2781–2789 (2013).

159. Zhang, X., Li, M., Walter, J., O'Brien, L., Manno, M. A., Voigt, B., Mork, Frazier, F., Baryshev, S. V., Kakalios, J., Aydil, Eray, S., Leighton, C. Potential resolution to the doping puzzle in iron pyrite: Carrier type determination by Hall effect and thermopower. *Phys. Rev. Mater*. **1**, 1–11 (2017).

160. Park, B.-I., Yu, S., Hwang, Y., Cho, S., Lee, J., Park, C., Lee, D., Lee, S. Highly crystalline Fe_2GeS_4 nanocrystals: green synthesis and their structural and optical characterization. *J. Mater. Chem. A* **3**, 2265–2270 (2015).

161. Gudelli, V. K., Kanchana, V. & Vaitheeswaran, G. Predicted thermoelectric properties of olivine-type Fe_2GeCh_4 (Ch = S, Se and Te). *J. Phys. Condens. Matter.* **28**, 25502 (2016).

162. Shi, X., Tian, A., You, J., Yu, Z., Yang, H., Xue, X. Fe_2SiS_4 nanoparticle - A new heterogeneous Fenton reagent. *Mater. Lett*. **169**, 153–156 (2016).

163. Lim, D., Ramasamy, P. & Lee, J. Solution synthesis of single-crystalline Fe_2GeS_4 nanosheets. *Mater. Lett*. **183**, 65–68 (2016).

164. Liu, M., Berg, D. M., Hwang, P., Lai, C., Stone, K. H., Babbe, F., Dobson, K. D., Radu, D. R. The promise of solution-processed Fe_2GeS_4 thin films in iron chalcogenide photovoltaics. *J. Mater. Sci*. **53**, 7725–7734 (2018).

165. Fredrick, S. J. & Prieto, A. L. Solution Synthesis and Reactivity of Colloidal Fe_2GeS_4: A Potential Candidate for Earth Abundant, Nanostructured Photovoltaics. *J. Am. Chem. Soc*. **135**, 18256–18259 (2013).

Appendices

A. Supporting information for Chapter 3

Table A1. Calculated C-S and S-S bond characteristics for alkyl disulfide reagents.

Precursor **R-SS-R**	R-S BDE (kcal/mol)	S-S BDE (kcal/mol)	(C-S)-(S-S) (kcal/mol)	C-S bond length (Å)	S-S bond length (Å)	C-S-S-C dihedral angle (deg)
Allyl-SS-Allyl	47.03	61.14	-14.11	1.8729	2.0920	90.33
Bz-SS-Bz	50.18	61.93	-11.74	1.8736	2.0917	87.70
t-Bu-SS-*t*-Bu	57.42	63.09	-5.67	1.8904	2.0956	111.58
Ph-SS-Ph	72.21	45.07	27.13	1.8071	2.1148	79.24

Tables A2. Calculated C-S and S-S bond characteristics for alkyl thiol reagents

Precursor **R-S-H**	C-S BDE (kcal/mol)	C-S bond length (Å)	S-H bond length (Å)	C-S-H bond angle (deg)
Allyl-SH	51.25	1.8690	1.3564	96.70
Bz-SH	54.06	1.8687	1.3583	96.65
t-Bu-SH	63.47	1.8782	1.3582	96.53
Ph-SH	77.17	1.8180	1.3590	97.19

Table A3. Calculated C-S and S-S bond characteristics for alkyl sulfide reagents

Precursor **R-S-R**	C-S BDE (kcal/mol)	C-S bond length (Å)	C-S-C bond angle (deg)
Allyl-S-Allyl	59.31	1.8609	98.93
Bz-S-Bz	62.31	1.8608	98.46
t-Bu-S-*t*-Bu	65.61	1.8814	113.53
Ph-S-Ph	69.35	1.8165	100.83

Table A4. Summary of calculated C-S bond dissociation energy (BDE) for disulfides, thiols, and thioethers and the experimental product and crystal phase obtained, including sulfur/iron atomic ratios derived from quantitative energy-dispersive X-ray spectroscopy (EDS) and particle sizing

Precursor (R =)	C-S BDE (kcal/mol)	S-S BDE (kcal/mol)	Product	Crystal Phase	S:Fe Ratio	Size (nm)** (n = 100)
Allyl-SS-Allyl	47.03	61.14	FeS_2	Pyrite*	1.98	150 ± 45.7
Bz-SS-Bz	50.18	61.93	Fe_3S_4	Greigite	1.30	-
tBu-SS-tBu	57.42	63.09	Fe_7S_8	Pyrrhotite	1.11	232 ± 68.5
Ph-SS-Ph	72.21	45.07	Fe_7S_8	Pyrrhotite	1.14	511 ± 104.6
Allyl-SH	51.25	-	Fe_3S_4	Greigite	1.30	-
Bz-SH	54.06	-	Fe_3S_4	Greigite	1.29	-
tBu-SH	63.47	-	Fe_7S_8	Pyrrhotite	1.01	219 ± 107.0
Ph-SH	77.17	-	Fe_7S_8	Pyrrhotite	1.05	372 ± 144.5
Allyl-S-Allyl	59.31	-	Fe_7S_8	Pyrrhotite	1.14	319 ± 101.0
Bz-S-Bz	62.31	-	Fe_7S_8	Pyrrhotite	1.06	340 ± 104.0
tBu-S-tBu	65.61	-	Fe_7S_8 + Fe_3O4	Pyrrhotite & Magnetite	0.72	130 ± 67.9
Ph-S-Ph	69.35	-	Fe_3O_4	Magnetite	0.02	18 ± 6.2

* Pure phase pyrite FeS_2 resulted after 30 min reaction time. Longer reaction times led to formation of pyrrhotite impurities. See Figure A1 for details

** For FeS_2 cubic nanoparticles, the longest edge length was measured. For hexagonal and irregular hexagonal shaped pyrrhotite nanoparticles, the longest diagonal was measured. Greigite sheets had no regular shape and it was difficult to distinguish individual particles.

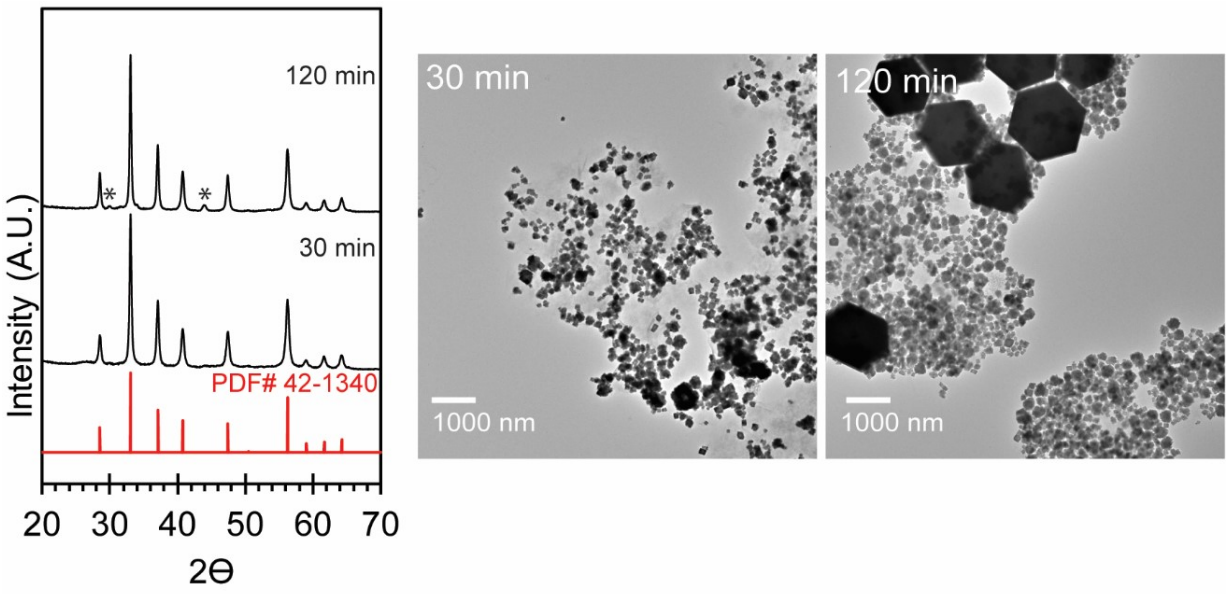

Figure A1. Phase purity of FeS_2 particles resulting from using allyl disulfide as sulfur precursor over time. Pyrite was obtained at 30 min as evidenced by the XRD pattern, but after extended heating for 120 min, pyrrhotite impurities appeared, as evidenced in the TEM as large ~1 μm hexagonally shaped particles and reflections denoted by asterisks in the XRD pattern. Since pyrite is the most thermodynamically stable iron sulfide mineral,[64] and pyrite formation is believed to be an irreversible process based on previous studies,[85] we speculate that the source of the pyrrhotite phase is from the impurities associated with the 80% technical grade allyl disulfide precursor used here. Allyl-S-Allyl is the most likely culprit since it is the most abundant impurity in the technical grade allyl disulfide (~14% as determined by ^{1}HNMR integration); which was shown in this study to produce pyrrhotite in a reaction with an iron(II) precursor under the same conditions (Figure 3.1i). Additionally, the numerous organosulfur compounds that result from thermal decomposition of allyl disulfide could contribute to the formation of the pyrrhotite platelets observed.

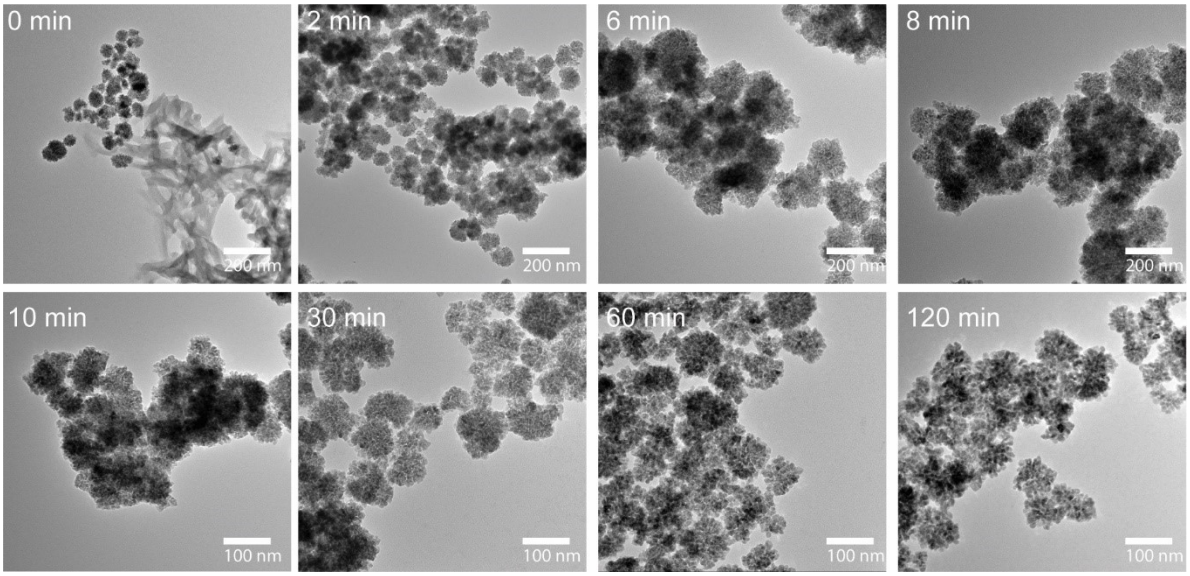

Figure A2. Study of pyrite formation mechanism using **elemental sulfur** as the sulfur source. TEM images of corresponding aliquots taken at 0, 2, 6, 8, 10, 30, 60 and 120 minutes after injection of elemental sulfur. The resultant particles have dendritic morphologies.

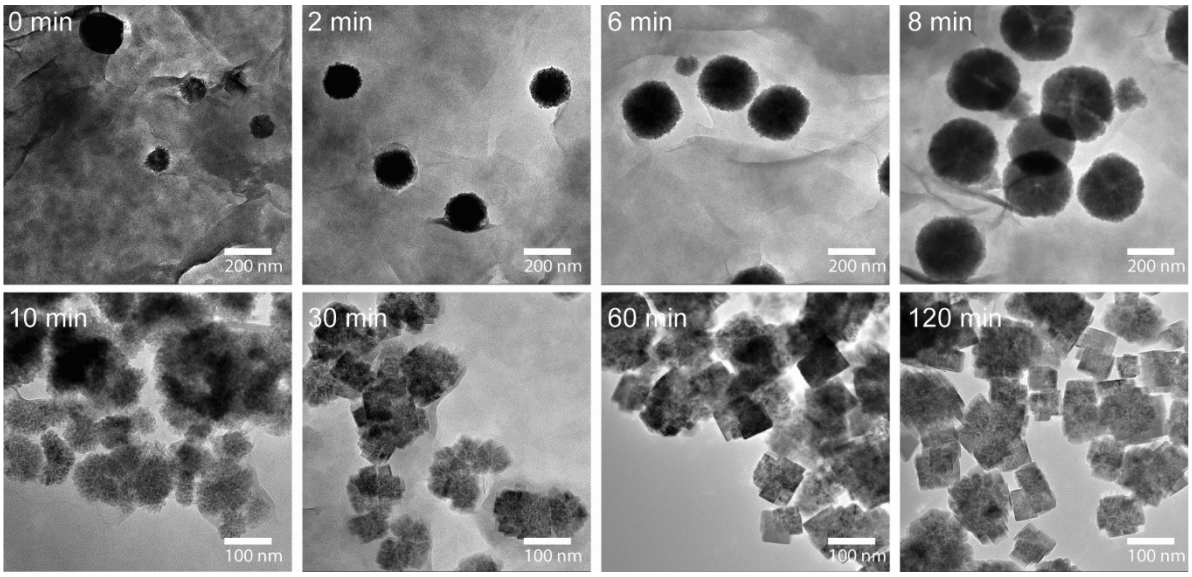

Figure A3. Study of pyrite formation mechanism using **Allyl-SS-Allyl** as the sulfur source. TEM images of corresponding aliquots taken at 0, 2, 6, 8, 10, 30, 60 and 120 minutes after injection of Allyl-SS-Allyl. The resultant particles have cube-like morphologies.

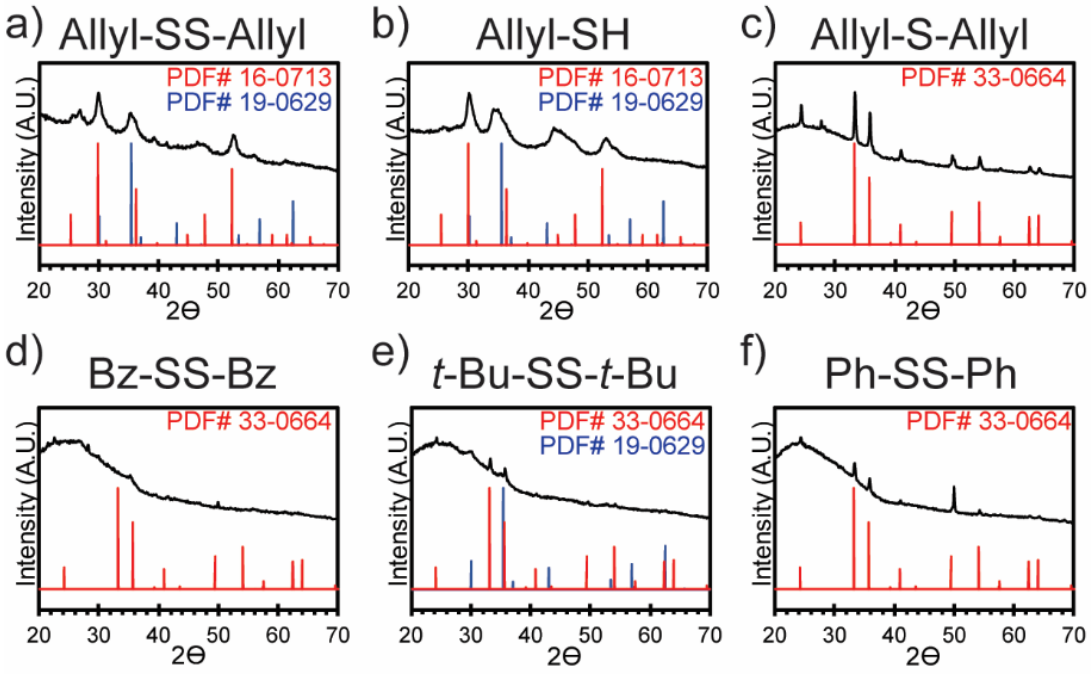

Figure A4. XRD patterns of resulting particles of a reaction using neat octadecene (ODE) as the solvent at 220°C for a) Allyl-SS-Allyl, b) Allyl-SH, c) Allyl-S-Allyl, d) Bz-SS-Bz, e) *t*-Bu-SS-*t*Bu, and f) Ph-SS-Ph.

The presence of an alkylamine (oleylamine) in solution was established as a key component in the formation of FeS_2 particles using Allyl-SS-Allyl as the organosulfur precursor. A series of control experiments were conducted where oleylamine (used in the original experiment) was completely replaced by octadecene (ODE) as the solvent for several of the organosulfur reagents. While the $FeCl_2$ did dissolve in ODE to give a light tan solution, the strongly colored Fe^{2+} amine complex was not observed prior to injection. Qualitatively, the reaction mixtures at the end of each reaction were notably more transparent in color when ODE was used as the solvent compared to the corresponding reactions in OAm, and considerably lower product yields were obtained in ODE reactions. Almost none of the reagents formed the same product in neat ODE compared to neat OAm (reported in Figure 3.1). Allyl-SS-Allyl and Ally-SH were the only reagents that formed an iron sulfide product (Figure A4 a & b respectively), where broad peaks corresponding to greigite (Fe_3S_4, PDF#16-0713) and magnetite (Fe_3O_4, PDF# 19-0629) were observed. For Allyl-S-Allyl, Bz-SS-Bz, *t*-Bu-SS-*t*Bu, and Ph-SS-Ph (Figure A4 c-f respectively) only the iron oxides of magnetite (Fe_3O_4, PDF# 19-0629) and hematite (Fe_2O_3, PDF# 33-0664) were obtained. We conclude that the presence of an alkylamine is necessary for the formation of the other iron sulfide phases with the organosulfur precursors used here. In addition to forming the colored Fe^{2+}-amine complex, it is likely that the amine is necessary for the iron-catalyzed decomposition of the organosulfur reagents.

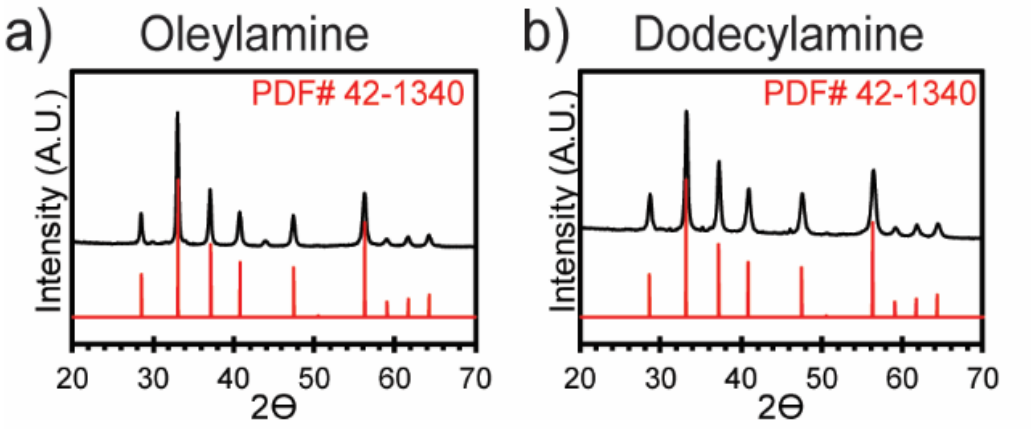

Figure A5. XRD patterns of resulting particles of a reaction using Allyl-SS-Allyl as the organosulfur precursor with the alkylamine solvent as a) oleylamine (OAm, from Figure 1a), and b) dodecylamine (DDA). Dodecylamine was used in a control experiment to determine if alkyl chain length (and mid chain alkene group of OAm) affected the iron sulfide product obtained when Allyl-SS-Allyl is used as the sulfur source. In both cases iron pyrite (FeS_2, PDF#42-1340) is the obtained crystalline product. Dodecylamine was used instead of octylamine because of its higher boiling point (octylamine is incompatible with the synthesis at 220°C as its boiling point is 170°C). We conclude that the alkyl chain length (and mid chain alkene) play a minimal role in the resultant crystalline phase obtained while the amine group is the key component in producing the active sulfur species responsible for nucleating with the iron(II) precursor.

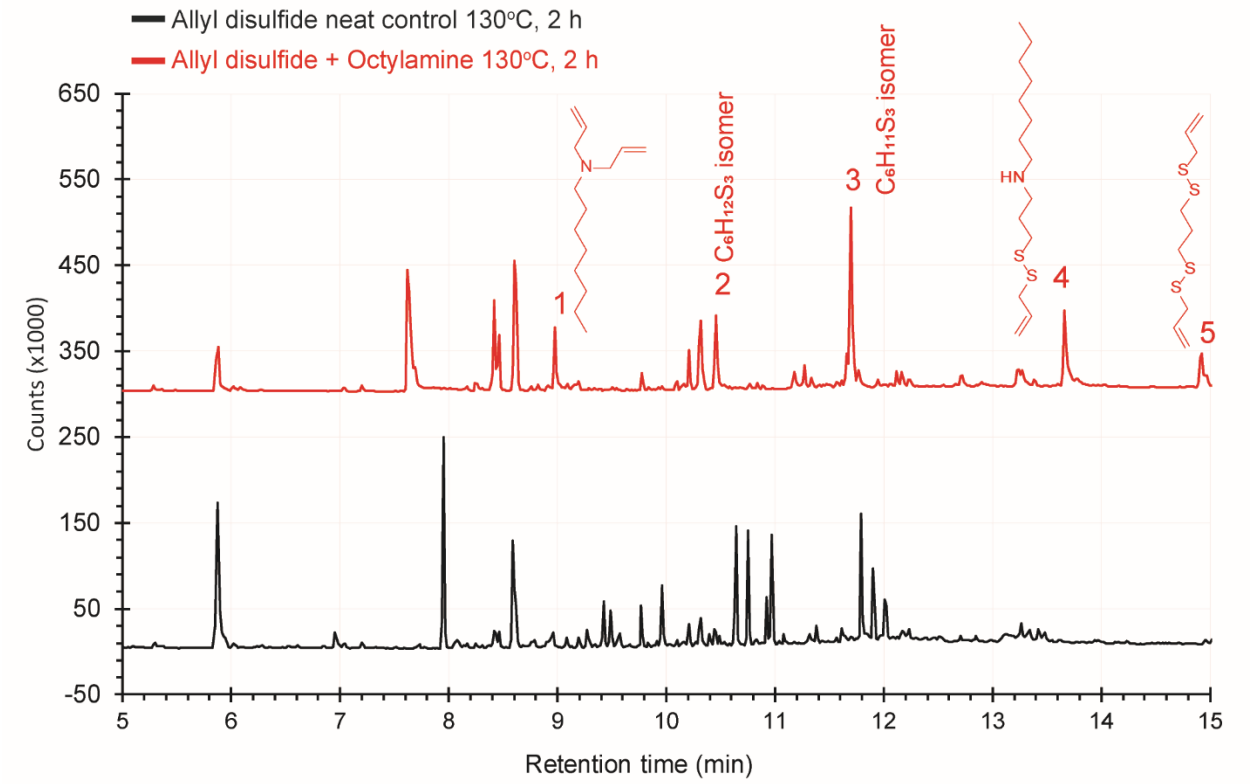

Figure A6. GC traces for allyl disulfide in octylamine after heating 130°C for 2 h (red) and neat allyl disulfide control after heating at 130°C for 2 h (black). The new compounds unique to allyl disulfide/octylamine heated solution are labeled 1-5 with their likely structures.

GC-MS analysis of compounds 1-5 after heating at 130°C for 2 h: Name: retention time; *m/z* (relative intensity).

1. Di-*N*-allyloctanamine: 8.97 min; *m/z* = 170 (20%, M^+), 154 (78%), 126 (57%), 112 (49%), 84 (51%), 70 (100%), 42 (58%)
2. $C_6H_{12}S_3$ isomer: 10.46 min; *m/z* = 180 (48%, M^+), 146 (50%), 119 (100%), 105 (15%), 73 (28%), 45 (46%)
3. $C_6H_{11}S_3$ isomer: 11.69 min; *m/z* = 179 (100%, M^+), 145 (6%), 119 (12%), 105 (38%), 73 (10%), 45 (20%)
4. *N*-(3-(allyldisulfanyl) propyl) octan-1-amine: 13.68 min; *m/z* = 276 (10%, M^+), 233 (94%), 200 (20%), 142 (27%), 133 (22%), 119 (16%), 72 (35%), 58 (59%), 44 (100%)
5. 1,3-bis(allylsulfanyl)propane: 14.92 min; *m/z* = 253 (8%, M^+), 211 (8%), 179 (100%), 146 (55%) 119 (16%), 105 (35%), 73 (26%), 45 (35%).

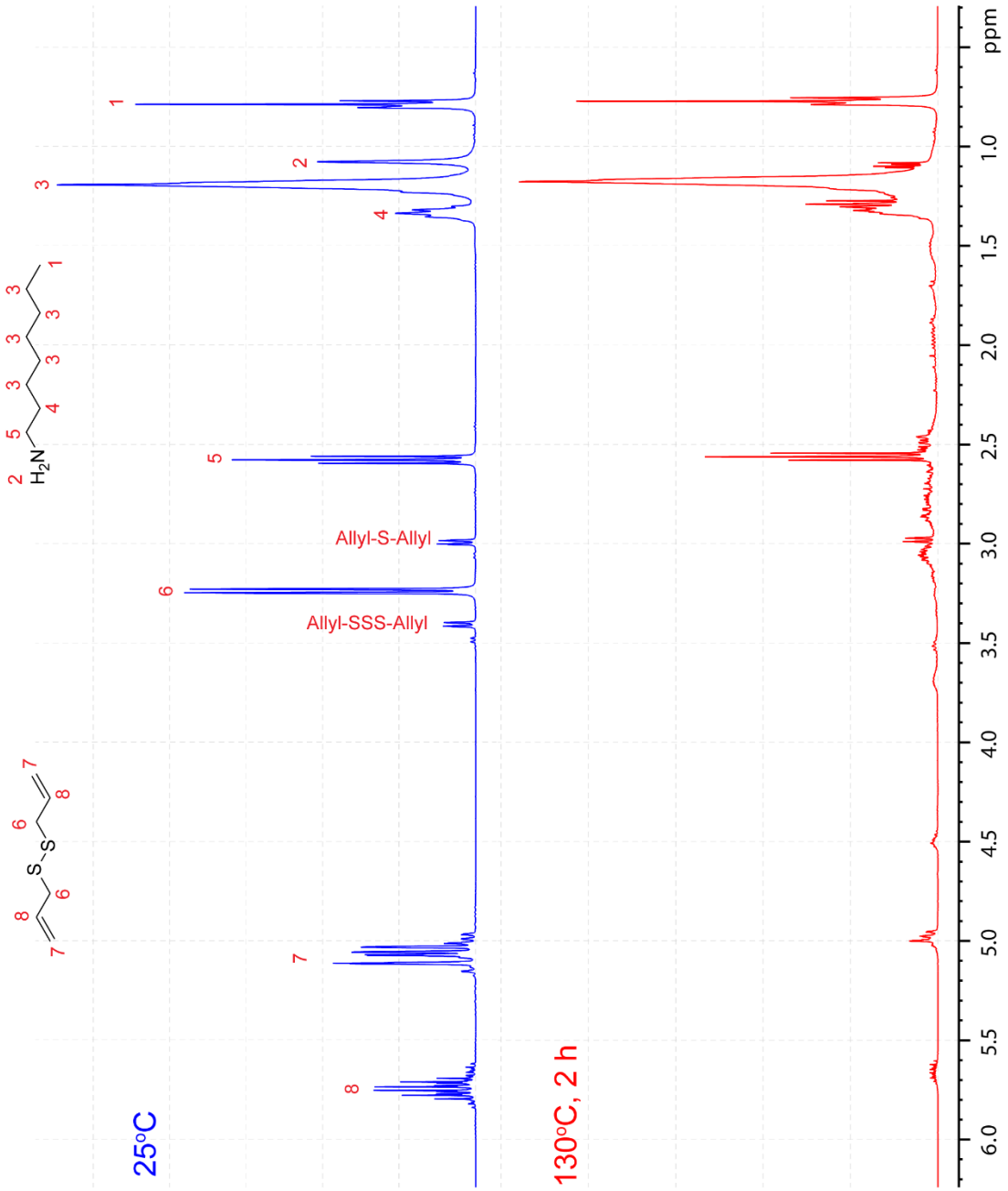

Figure A7: ^{1}H NMR overlay for a 1:1 molar ratio solution of allyl disulfide and octylamine at room temperature (blue) and after heating for 2 h at 130°C (red). Allyl disulfide resonances disappear and numerous low intensity resonances appear.

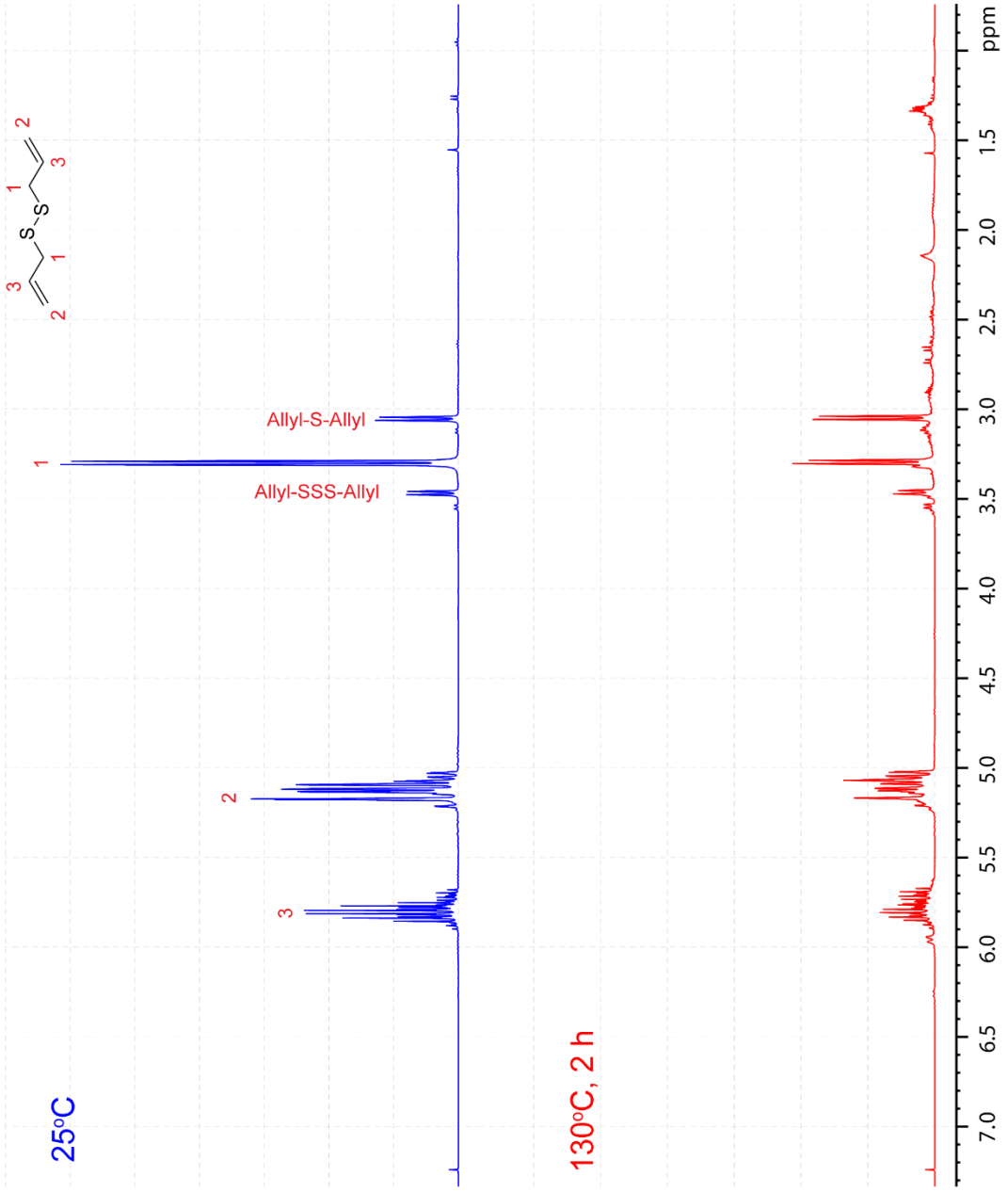

Figure A8: ^{1}H NMR overlay for allyl disulfide at room temperature (blue) and after heating for 2 h at 130°C (red). Used as control experiment to monitor thermal decomposition of allyl disulfide. Allyl disulfide resonances decrease as numerous low intensity peaks appear, likely decomposition products.

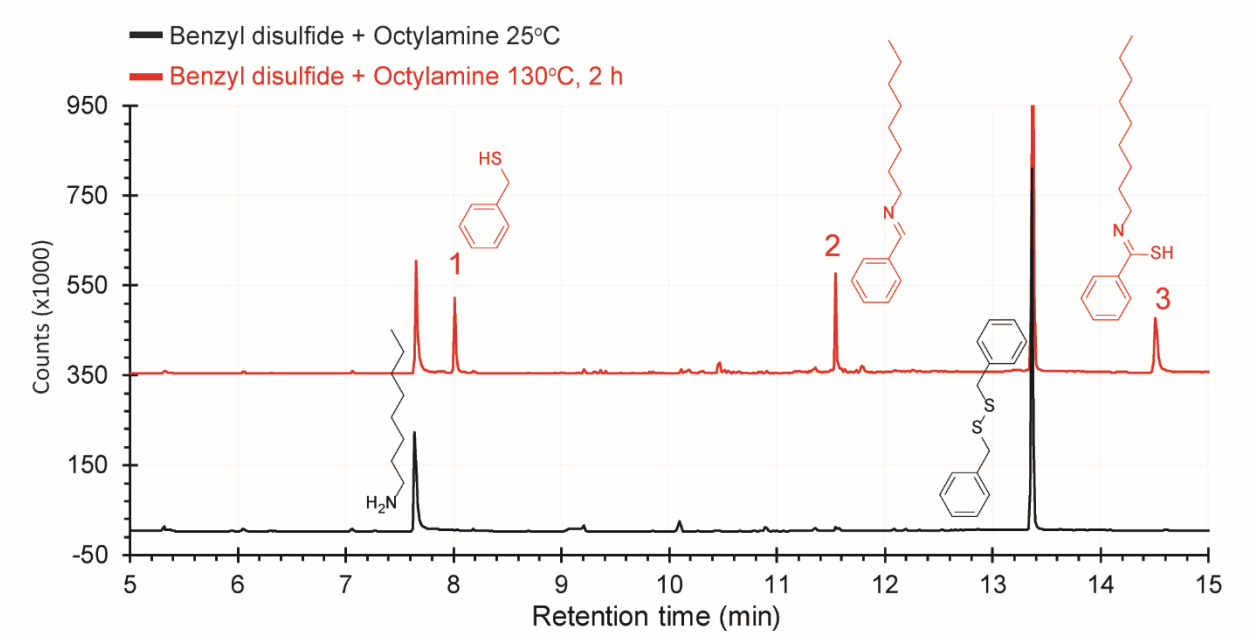

Figure A9. GC trace for benzyl disulfide in octylamine at room temperature (black) and after heating at 130°C for 2 h (red).

GC-MS analysis of compounds 1-3 after heating at 130°C for 2 h. Name: retention time; *m/z* (relative intensity, ion).

1. Benzyl mercaptan: 7.99 min; *m/z* = 124 (34%, M^+), 91 (100%), 65 (24%)
2. *N*-octyl-1-phenylmethanimine: 11.55 min; *m/z* = 218 (27%, M^+), 174 (19%), 160 (100%), 132 (28%), 118 (39%), 104 (15%), 91 (53%)
3. (Z)-*N*-nonylbenzimidothioic acid: 14.53 min; *m/z* = 250 (100%, M^+), 145 (6%), 119 (12%), 105 (38%), 73 (10%), 45 (20%)

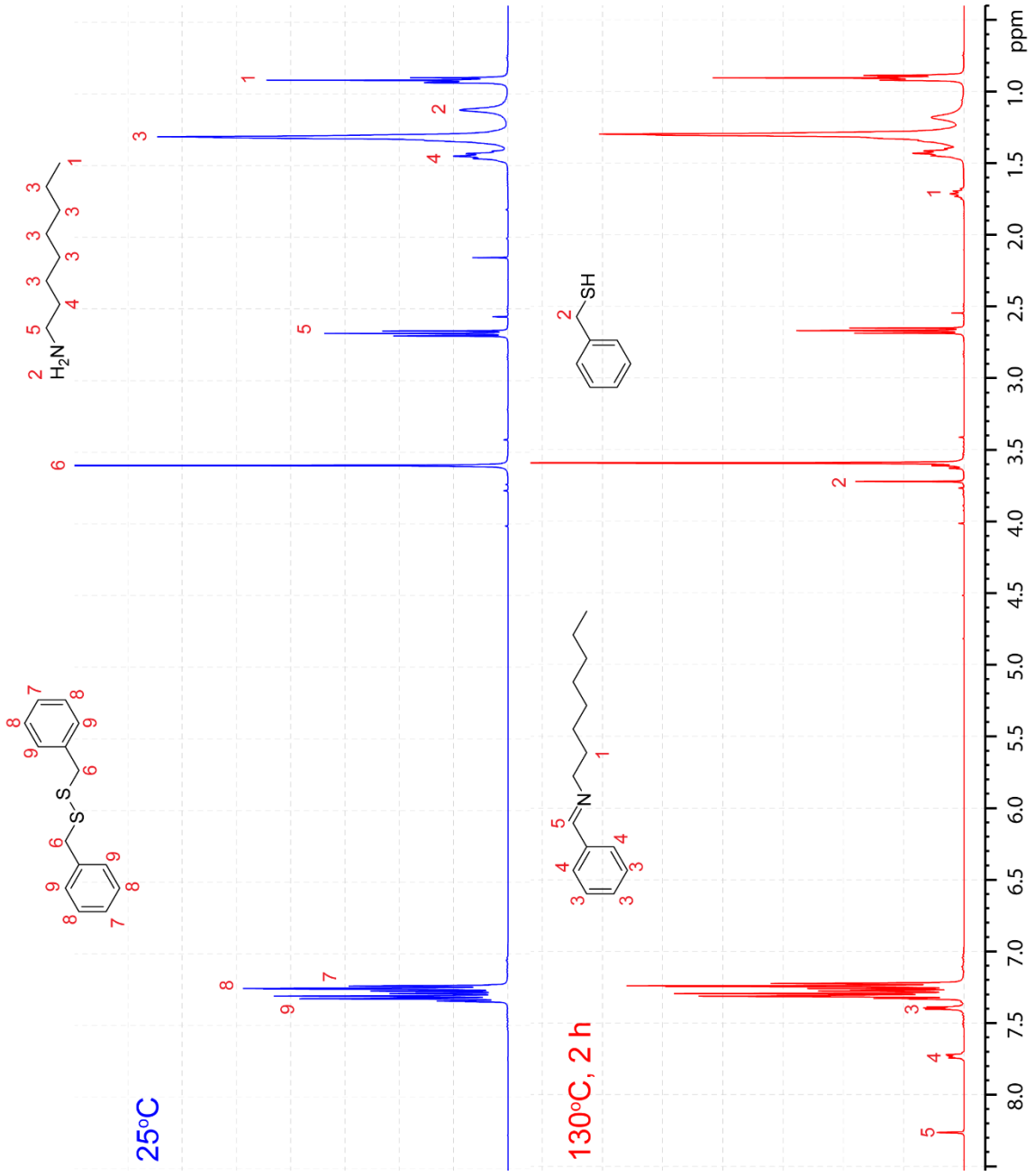

Figure A10. ^{1}H NMR overlay for a 1:1 molar ratio solution of benzyl disulfide and octylamine at room temperature (blue) and after heating for 2 h at 130°C (red). The new resonances unique to the solution after heating are assigned to *N*-octyl-1-phenylmethanimine and benzyl mercaptan.

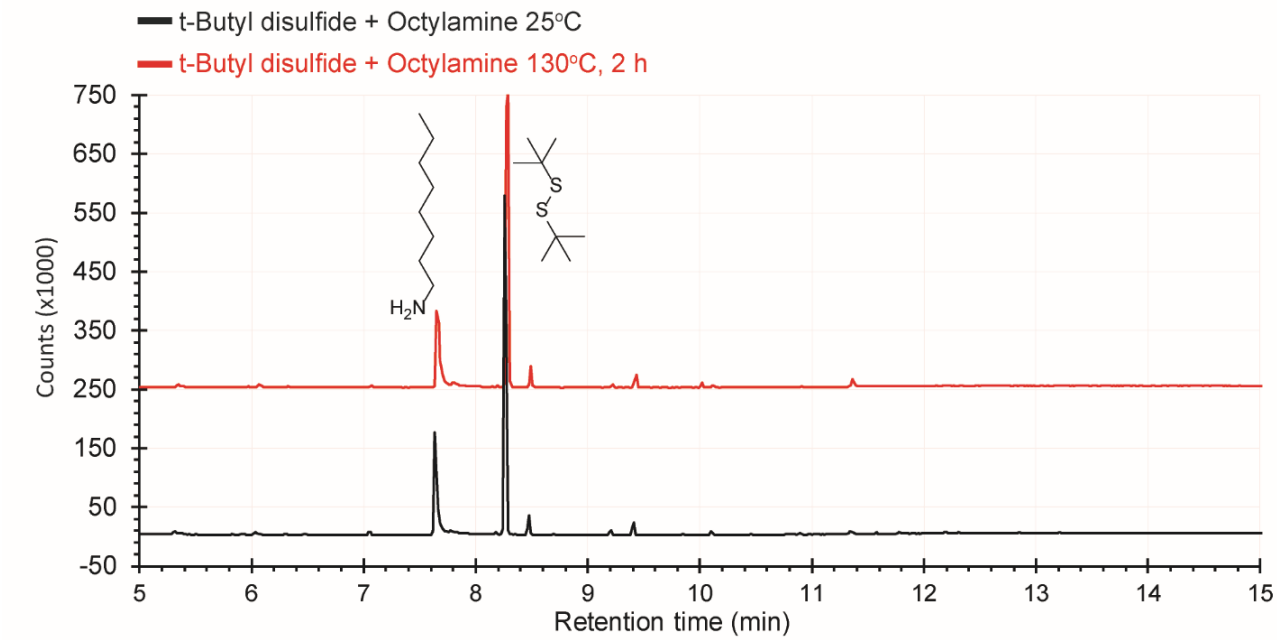

Figure A11. GC trace for di-*tert*-butyl disulfide in octylamine at room temperature (black) and after heating at 130°C for 2 h (red). No new compounds were identified after heating.

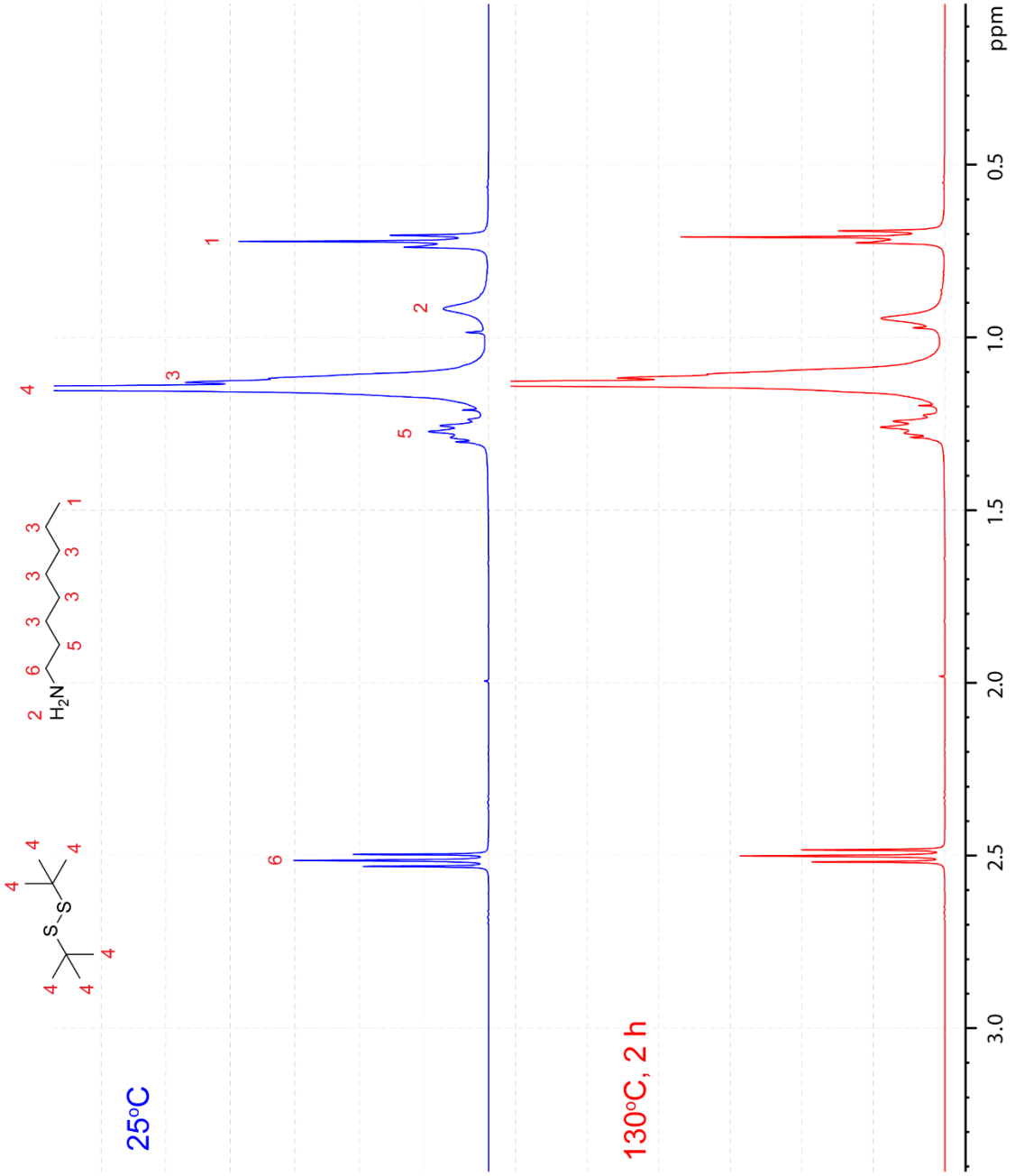

Figure A12. ^{1}H NMR spectra overlay for a 1:1 molar ratio solution of tert-butyl disulfide and octylamine at room temperature (top) and after heating for 2 h at 130°C (bottom). No new resonances are apparent after heating, indicating that no reaction occurred.

B. Supporting information for Chapter 4

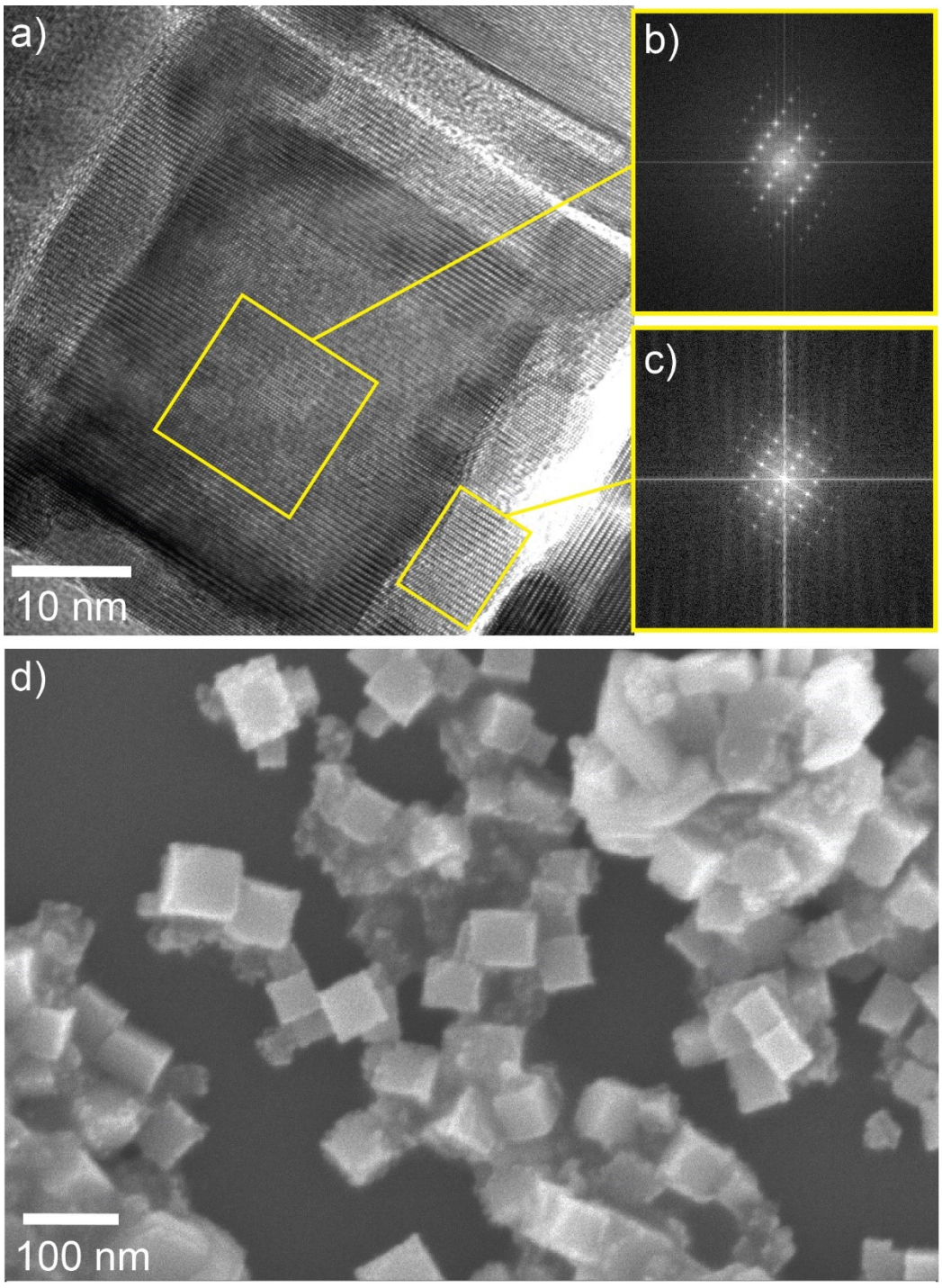

Figure B1. a) A high resolution TEM image of a hybrid nanocrystal with b) including FFT analysis of lattice fringing pattern from FeS_2 core nanocube and c) including FFT analysis of lattice fringing from CoS_2 frame demonstrating epitaxial growth, as well as d) a SEM image depicting the core-frame hybrid nanocubes.

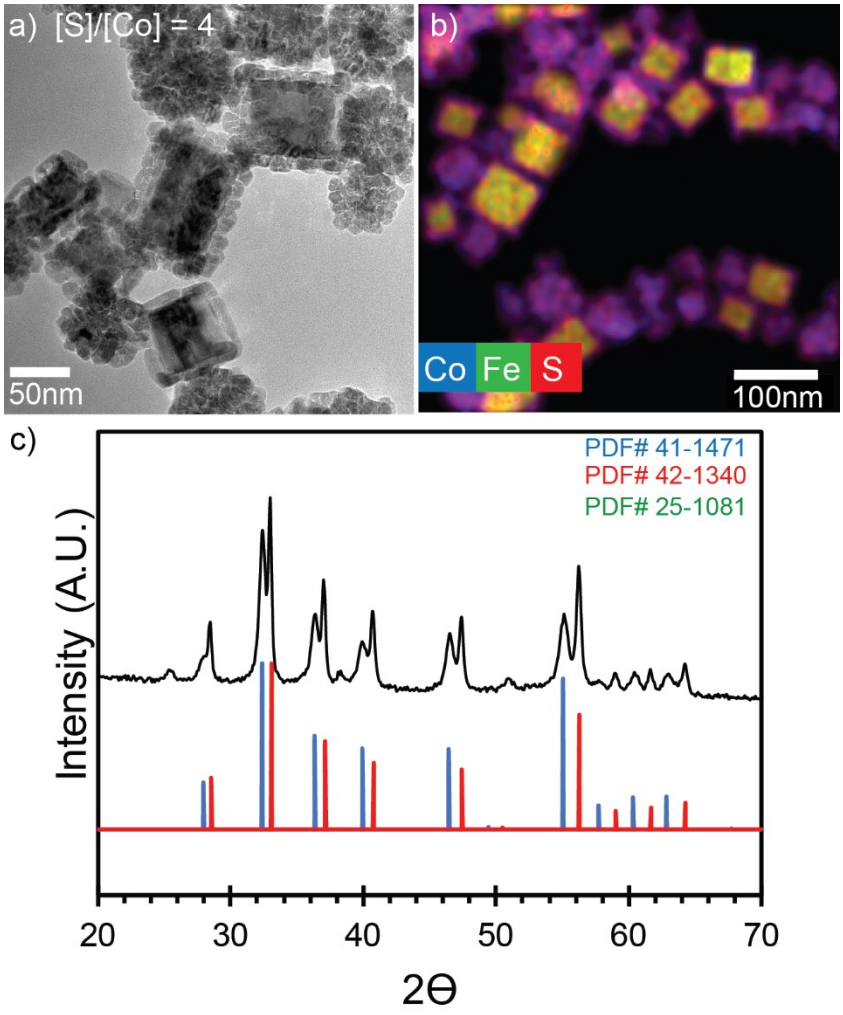

Figure B2. Characterization of resulting hybrid nanocrystal product when [S]/[Co] = 4. Greater surface coverage of FeS_2 nanocubes by CoS_2 is observed as well as heterogenous nucleation of CoS_2 and presence of a minor CoS (Jaipurite) impurity phase.

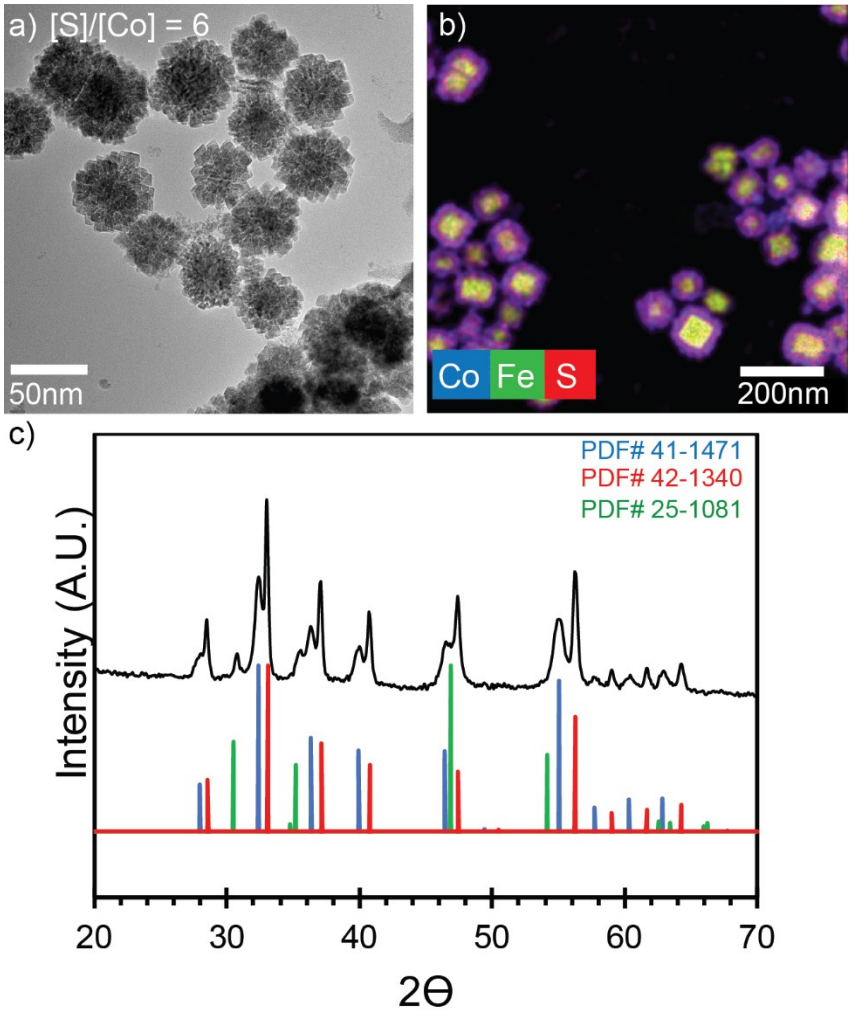

Figure B3. Characterization of resulting hybrid nanocrystal product when [S]/[Co] = 6. Complete coverage of FeS_2 nanocubes by CoS_2 is observed as well as heterogenous nucleation of CoS_2 and presence of a minor CoS (Jaipurite) impurity phase.

Jordan M. Rhodes

Jordanrhodes22@gmail.com

Education

Vanderbilt University, Nashville, TN
Expected graduation May 2020
PhD in Chemistry
Advisor: Janet E. Macdonald

Rider University
2014 B.S. in Chemistry, *cum laude*

Research Experience

Macdonald Laboratory, Vanderbilt University, Aug. 2014-May2020

Chen Laboratory (Rider University, Undergraduate)

Teaching

Lab Teaching Assistant, Vanderbilt University
Organic Chemistry, Multiple Semesters 2018-2020
General Chemistry, Multiple Semesters 2015-2016

Publications

Jordan M. Rhodes, James R. McBride, Janet E. Macdonald. "Synthesis of FeS_2-CoS_2 Core Frame and Core-Shell Hybrid Nanocubes," *Chemistry of Materials,* **2018**, (30), 8121-8125.

Jordan M. Rhodes, Caleb A. Jones, Lucas B. Thal, Janet E. Macdonald. "Phase-Controlled Colloidal Synthesis of Iron Sulfide Nanocrystals via Sulfur Precursor Reactivity and Direct Pyrite Precipitation," *Chemistry of Materials,* **2017**, (29), 8521-8530.

Emil A. Hernandez-Pagan, Andrew O'Hara, Summer L. Arrowood, James R. McBride, **Jordan M. Rhodes**, Sokrates T. Pantelides, Janet E. Macdonald. "Transformations of the Anion Sublattice in the Cation-Exchange Synthesis of Au_2S form $Cu_{2-x}S$ Nanocrystals," *Chemistry of Materials,* **2018,** (30), 8843-8851.

Emil A. Hernandez-Pagan, Alice D. P. Leach, **Jordan M. Rhodes**, Suresh Sarkar, Janet E. Macdonald. "A Synthetic Exploration of Metal-Semiconductor Hybrid Particles of $CuInS_2$," *Chemistry of Materials*, **2015**, (27), 7969-7976.

Presentations

Gordon Research Conference, Smithfield, RI, 2018 (Poster Presentation)
Synthesis of FeS_2-CoS_2 core-frame and core-shell hybrid nanocubes and electrocatalytic activity toward HER
ACS National Meeting Washington DC, 2017 (Oral Presentation)
Phase-controlled synthesis of iron sulfide nanoparticles via sulfur precursor reactivity

VINSE Summer Seminar, Vanderbilt University, 2018 (Oral Presentation)

Phase-controlled synthesis of iron sulfide nanoparticles via sulfur precursor reactivity

VINSE 19th Annual Nanoscience and Nanotechnology Forum, Vanderbilt University, 2018 (Poster Presentation)

Synthesis of FeS_2-CoS_2 core-frame and core-shell hybrid nanocubes and electrocatalytic activity toward HER *2nd place poster competition winner

VINSE 18th Annual Nanoscience and Nanotechnology Forum, Vanderbilt University, 2017 (Poster Presentation)

Phase-controlled synthesis of iron sulfide nanocrystals via sulfur precursor reactivity and direct pyrite precipitation

Volunteering Vanderbilt Student Volunteers for Science (VSVS), 2015-2017